A Thesis

entitled

A Comparison of Two and Three Bladed Floating Wind Turbines

by Brett Andersen

Submitted to the Graduate Faculty as partial fulfillment of the

requirements for the Masters of Science Degree in Mechanical Engineering

_____
Dr. Abdollah Aliakbarkhan Afjeh
Committee Chair

_____
Dr. Duane Hixon
Committee Member

_____
Dr. Efstratios Nikolaidis
Committee Member

_____
Dr. Larry Viterna
Committee Member

_____
Dr. Patricia Komuniecki, Dean
College of Graduate Studies

The University of Toledo
May 2010

An Abstract of

A Comparison of Two and Three Blade Wind Turbines on Floating Platforms

by Brett Andersen

Submitted to the Graduate Faculty as partial fulfillment of the

requirements for the Masters of Science Degree in Mechanical Engineering

The University of Toledo
May 2010

A possible solution to the limitations of current offshore wind technology would be the utilization of a floating platform. Floating platforms are not a new idea, as the oil and gas industries have been constructing and using floating platforms for a number of years. Two bladed wind turbines offer the following advantages over three bladed in a floating environment: cost savings of one blade, lower weight further reduces system costs, easier rotor lift and assembly, and greater rotor speeds reduce drivetrain stress. Additionally, two blade rotors usually feature flexible blades or a teetered hub with a pivot point. This is especially important for floating wind turbines because the teeter pin effectively decouples the motion of the rotor plane from the tower motion, reducing damaging cyclic bending moments in the drive train.

This thesis is dedicated to everyone who has the courage and perseverance to go after what's calling.

Acknowledgments

This paper would not be possible without the opportunity granted me by Dr. Abdollah Aliakbarkhan Afjeh and Dr. Larry Viterna. I would also like to thank Dr. Jason Jonkman of the National Renewable Energy Lab (to think you answered my emails – WOW). I never would have considered I could complete a Masters level thesis without encouragement of Dr. Ray Hixon.

To my parents, you gave everything you had and I didn't give a second thought. My passion for this subject is directly related to your example.

To my friends in Hilton Head, my time with you probably had something to do with this work. To the boys of the squalor thanks for helping me back on my feet. To Bill Grass, Ben Gramling, Lisa Shimko thanks for "Aquatic Fen," Natalie Bate, Kristen Aagenas, Ed Lawrence you are a lunatic thanks for being a friend when I needed one, Selena Grodek my muse, Green Energy Ohio, and Robert Kozar thank you for giving me a peak behind the curtain. To Vijaya Sirangu for making sure I did things correctly. Finally, to Elise Bonnema because it might not seem crazy later.

Dr. Larry Viterna, thank you.

Contents

List of Tables

List of Figures

Chapter 1

Introduction

1.1 Overview

Harnessing the power of the sun through wind has been the fastest growing renewable energy resource for the past two decades. Open spaces, and a suitable average minimum wind speed are needed to generate utility scale power. Unfortunately, on land these criteria are not typically found near large population centers. Most large cities are located near the ocean or a lake. Offshore offers vast open spaces, higher average wind speeds than on land and thus provides an ideal location to generate wind energy. Studies performed by the National Renewable Energy Laboratory (NREL) estimate that offshore wind resource are greater than 1000 GW for the United States [3].

Currently, the harnessing of offshore wind requires the building of foundations in the sea floor, which results in higher costs than land based wind energy due to the complexity of the construction. The necessity of having to build platforms in the ocean floor also limits the depth of water in which offshore wind turbines can be built. A possible solution to

the limitations of current offshore wind technology would be the utilization of a floating platform. Floating platforms are not a new idea, as the oil and gas industries have been constructing and using floating platforms for a number of years.

A floating platform wind turbine holds the promise of generating large amounts of electricity offshore in both shallow and deep waters near the world's large coastal cities. Lowering the cost of energy (COE) is critical for expanding the use of wind turbines, particularly for offshore sites. Achieving favorable economics on a floating platform wind turbine depends less on reducing wind turbine costs and more on an integrated full system design that reduces the life cycle costs [4].

A car is not a boat. They both transport people and things from point A to point B. They both use a motor. They both have someone who drives. But a car is not a boat. As obvious as it may seem, a floating platform wind turbine is not an on-land wind turbine. Currently, and including in this paper, ideas for a floating platform wind turbines have simply been putting an on-land wind turbine on top of a floating platform. Although this may ultimately be what a floating platform wind turbine will look like (at the time of writing, Statio-Hywind floating platform wind turbine is operating off the coast of Norway) , the purpose of this paper is to add to the conversation of designing a floating platform wind turbine that accounts for the unique loads and dynamics a floating wind turbine would experience.

In NREL's paper, "Engineering Challenges for Floating Offshore Wind Turbines " it is stated that the economics of a floating system are assumed to be dominated by the additional costs associated with a floating platform and power distribution. A few of the design challenges, mentioned in the paper are: system weight, installation, maintenance decommission costs, tower-top motions, and controls complexity. Removing one blade from the standard three-bladed rotor may provide positive results for many of the design challenges. These include:

- Cost savings of one blade
- Lower weight further reduces system costs
- Easier rotor lift and assembly
- Greater rotor speeds reduce drivetrain stress

Removing one blade from a standard three-blade rotor would reduce the weight of the rotor by approximately one-third. The reduced weight in the rotor would translate to further reductions in weight especially in the tower and platform. A two-bladed rotor has other distinct advantages. For example, a two-bladed rotor is much easier to handle during installation, repair, and maintenance, and decommissioning. This is significant regardless if the blades are assembled to the nacelle on land or offshore. In either case handling two blades instead of three is much more convenient. Further a two blade rotor can take advantage of a teeter hinge at hub. Adding teetering effectively isolates the important out-of-plane bending loads on the blades to the low-speed shaft, reducing stress put on the gear box or direct-drive generator. A teeter hinge also passively accommodates for the variable motion that a floating platform would experience. Finally

two-blade turbines have a broader efficiency over the tipspeed range that may possibly increase power production under rapidly changing windspeeds.

This thesis presents the results of numerical studies conducted to investigate the performance and loads on two and three-bladed wind turbine designs for floating offshore installation. NREL's 5-MW Reference Wind Turbine for Offshore System Development [1] was used in this study. NREL's reference turbine was designed with three blades. We simply removed one blade and added a teeter hinge for the two blade analysis. We did not optimize the rotor blades for the two-bladed analysis. We used two speed control systems to regulate power production: pitch-to-feather and pitch-to-stall. We tested the three and two-bladed turbines on-top of four platforms: rigidly cantilevered to inertia frame, OC3/Hywind spar buoy, MIT/NREL tension leg platform (TLP), and ITI Energy barge.

For our comparison, we focused first on the annual energy production using two and three blades. For annual wind speed, we used the Rayleigh Wind Speed Distribution recommended by the IEC 61400-1 wind turbine design standard (using an average 10 mps at hub height).[5] To predict energy production, we used NREL's performance code WT_Perf.

Second, we ran time domain simulations of the four platforms at a steady wind speed of 13 mps for 100 seconds. We looked at the loads running through the turbine starting with the flap-wise bending moment of blade 1, the bending moment and torque of the low-

speed shaft, the tower-top bending moment and the tower-base bending moment. We also looked at the power and energy production.

1.2 – Previous Research

Many research programs have investigated the changes in the loads, the motions and power of a floating offshore wind turbine compared to a fixed-bottom one. [33] These simulation tools use assumptions that stem from the idea of a slender vertical surface-piercing cylinder extending from the sea floor. These approximations limit the tools' use for analyzing many floating platform concepts.

Other studies have modeled floating offshore wind turbines using linear frequency-domain analysis tools developed for the offshore oil and gas industries. These studies demonstrated that the natural frequencies of a floating platform wind turbine could be placed out of the range of high intensity waves.[22 - 25]

One problem with linear frequency-domain analysis tools is the inability to capture the nonlinear dynamic and transient effects that are crucial to wind turbine analysis. Other simulations include the use of a "state domain" technique and time-domain dynamic models [26]. Nielsen, Hanson, and Skaare and Larsen and Hanson have used a combination of aero-servo-elastic, hydrodynamic and mooring program to design a deep drafted spar buoy (called "Hywind"). These studies compared results to a scaled down

model. However, these computer simulations used Morison's equation to compute the hydrodynamics which ignores potentially important hydrodynamic effects.[27 - 29]

Jason Jonkman, at NREL, used a floating barge concept to develop a more sophisticated time domain aero-servo-elastic-hydro model. His model assumes linearity in terms of adding the effects of diffraction, hydrostatic, and radiation. [18] Using the program WAMIT, Jason's model calculates the frequency-domain radiation / diffraction hydrodynamics. He brings his results from WAMIT into the time domain through a program called HydroDyn. From the development of the WAMIT/HydroDyn/FAST program additional floating concepts where created. These include the StatoilHywind spar buoy concept [13] and the MIT/NREL tension leg platform [31].

Recently, NREL, Jason Jonkman, and Matha have performed a quantitative comparison of the responses of three floating platforms, following the design load cases outlined in the IEC 61400-3 design standard for offshore wind turbines. [34] In September 2009, Statoil Hywind launched a 2.3 MW floating wind on the spar buoy concept. [35]

Section 1.3 – Tools

WT_Perf

WT_Perf is a blade performance code offered by NREL. It is a descendent of the PROP code. It uses Blade Element Momentum (BEM) theory to determine the power extracted from the wind by the blades. A brief description of Blade Element Momentum theory is presented.

FAST

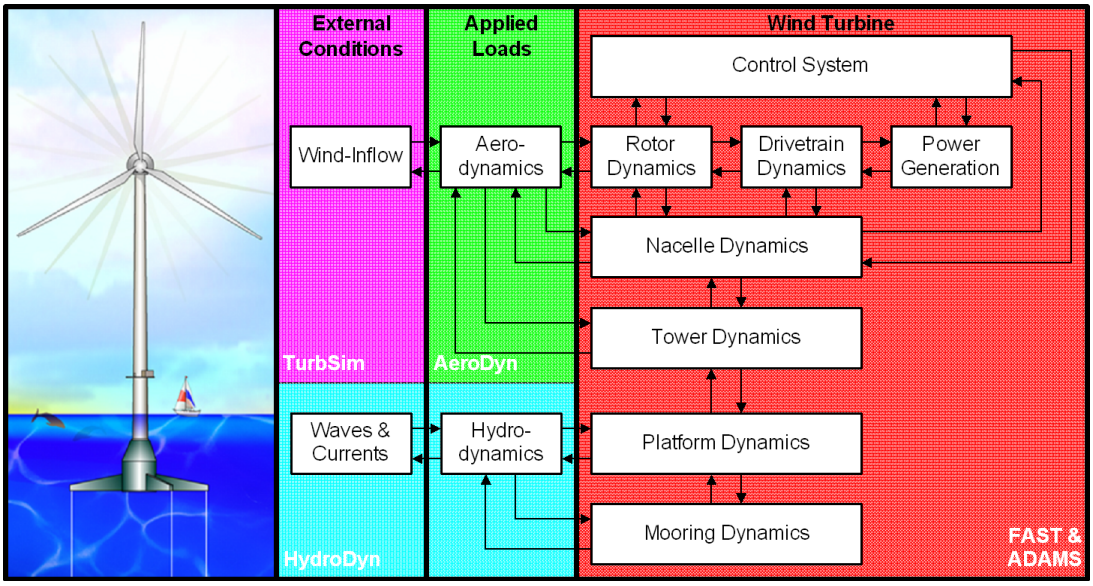

Figure 1.1 - Interfacing modules to achieve aero-hydro-servo-elastic simulation [18]

For our dynamic studies we used the program FAST (Fatigue, Aerodynamics, Structures and Turbulence). Our model can be broken into 3 different studies of physics: Aerodynamics, multi-body dynamics and hydrodynamics. For the aerodynamics analysis, FAST uses the program Aerodyn. Aerodyn uses airfoil tables and strip theory to calculate aerodynamic loads. Strip theory is similar to blade element momentum theory. Due to the similarity between strip theory and blade element theory not much time will be spent discussing Aerodyn. FAST uses the Kane Method of multi-body dynamics to model the interactive relationships of the wind turbine model. Hydrodyn is used to model the hydrodynamics. Hydrodyn was principally developed by Jason Jonkman at NREL [18]. It models the hydrodynamics by dividing the loads into static hydrodynamics, diffraction and radiation loads.

Section 1.4 – Outline of Thesis

The thesis is presented in five sections:

Section 1: Introduction – The motivation for this thesis, previous work, and tools used for study is presented here.

Section 2: Theory – This section covers the mathematical modeling and principle physics used to model floating platform wind turbines studied. First we consider Blade-Element Momentum Theory (BEM). Both WT_Perf and FAST use BEM. Second, we explain Kane Method of Multi-body Dynamics that FAST uses for calculation of the motions of the models tested.

Section 3: Model – Here we briefly look at the different components of the NREL wind turbine, and the three floating platforms. In this section we develop the two control algorithms used in our simulations.

Section 4: Results – First we compare the annual energy production of two-bladed and three-bladed wind turbines. Second we examine the results of the simulations performed in the time domain of the three floating platforms.

Section 5: Conclusion

Chapter 2

Theory

In this section a brief description of the major theoretical concepts used in this work is given. Specifically, we discuss:

- the Blade Element Momentum Theory (WT_Perf, Aerodyn)
- the Kane Method of Multibody Dynamics (FAST)
- the Hydrodynamic Model (HydroDyn)
- the Mooring System Model (HydroDyn)

2.1 - Blade Element Momentum Theory - Brief Overview

The Blade Element Momentum (BEM) Theory is the combination of the Momentum Theory and Blade Element Theory (or Propeller Theory). Estimates from BEM are found iteratively. We will give a synopsis on how WT_Perf performs this operation.

The BEM uses two methods of modeling the axial force and torque acting on a wind turbine blade to determine the rotor power and loads. The first method uses the conservation of momentum principle applied to the flow through a rotating stream tube. The second method uses the blade element theory. In combination, the two methods can

be used to determine the axial force and torque. The torque determines the power produced by the wind.

2.1.1 - Momentum Theory

Figure 2.1 presents a model of flow through a wind turbine. Station one is upstream from the turbine, station two is right before the blades, station three just after, and station four is far downstream. By assuming steady-state incompressible, homogenous, parallel flow and that $p_1=p_4$, it follows from the continuity equation that $V_2=V_3$. We can use momentum theory to find an expression for the axial force and torque. For this discussion, V_1 will be considered uniform.

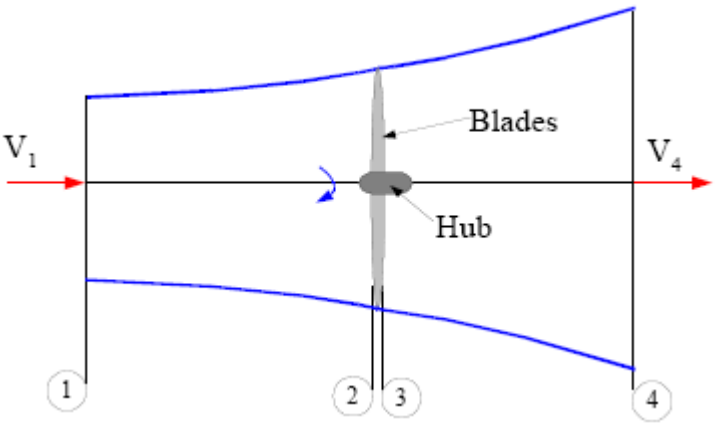

Figure 2.1 – Schematic of a Wind Turbine [5]

Applying the Bernoulli's equation to the flow between (1) and (2), then between (3) and (4), and combing the two equations yields:

$$p_2 - p_3 = \frac{1}{2}\rho\left(V_1^2 - V_4^2\right) \qquad 2.1$$

Remembering that the axial force is pressure times area

$$dF_x = (p_2 - p_3)\,dA \qquad 2.2$$

or

$$dF_x = \frac{1}{2}\rho(V_1^2 - V_4^2)\,dA \qquad 2.3$$

At this point we define the axial induction factor as the proportion of the velocity change due to the blades and the original wind.

$$a = \frac{V_1 - V_2}{V_1} \qquad 2.4$$

Having the velocity defined at the different points in terms of the induction factor will be useful in simplifying the equations. With some algebra it can be shown that:

$$V_2 = V_1(1 - a) \qquad 2.5$$

$$V_4 = V_1(1 - 2a) \qquad 2.6$$

Substituting Eqs. (2.5) and (2.6) into Eq. (2.3), we calculate the resulting axial force on a blade element.

$$dF_x = \frac{1}{2}\rho V_1^2 \left[4a(1 - a)\right]2\pi r\,dr \qquad 2.7$$

In a similar manner as above we look at the angular momentum. Consider Figure 2.2.

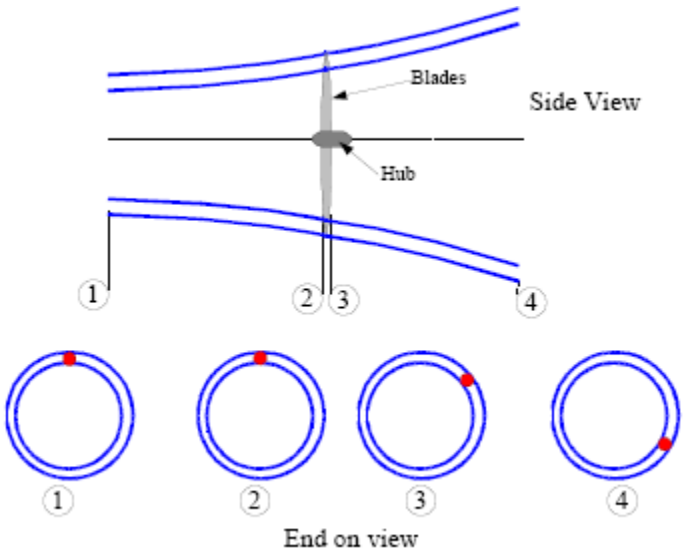

Figure 2.2 – axial wind flow past wind turbine [5]

As the flow moves past the blades, the blades are rotating; the rotating blades impart a rotation on the flow. The rotation in the flow means the flow across the blade in no longer straight. Figure 2.2 shows that at points one and two the wind element (marked by the red dot) is just cruising along in the homogenous flow. But during the meeting and transition with the moving blades a rotational effect enters its path that continues and seen at point 4. This rotational flow is characterized by the wake rotational speed, ω, and gives us the angular induction factor.

$$a' = \frac{\omega}{2\Omega} \qquad 2.8$$

ω=wake rotational speed

Ω=blade rotational speed

The definition of torque is:

$$T = \frac{dI\omega}{dt} = \frac{d\left(mr^2\omega\right)}{dt} = \frac{dm}{dt}r^2\omega \qquad 2.9$$

where I is the moment of inertia of the wind element.

The torque for a blade element is:

$$dT = d\dot{m}\omega r^2 \qquad 2.10$$

$$d\dot{m} = \rho dA V_2 = \rho 2\pi r dr V_2$$

$$dT = \rho 2\pi r dr V_2 \omega r^2$$

$$dT = 4a'(-a)\rho V \Omega r^3 \pi dr \qquad 2.11$$

This completes the description of the Momentum Theory. The above equations for the axial force and torque; (Eqs. 2.7 and 2.11) together with similar ones from the Blade Element Theory will be used to solve for the axial force and torque.

2.1.2 - Blade Element Theory (or propeller theory)

The Blade Element Theory is based on the principles of airfoil theory. The axial and rotational forces are calculated using the blade section lift and drag. A blade is divided into elements. It is assumed that each element does not interact with any other element. An example of a wind turbine blade broken up into several blade elements is represented in the accompanying Figure 2.3.

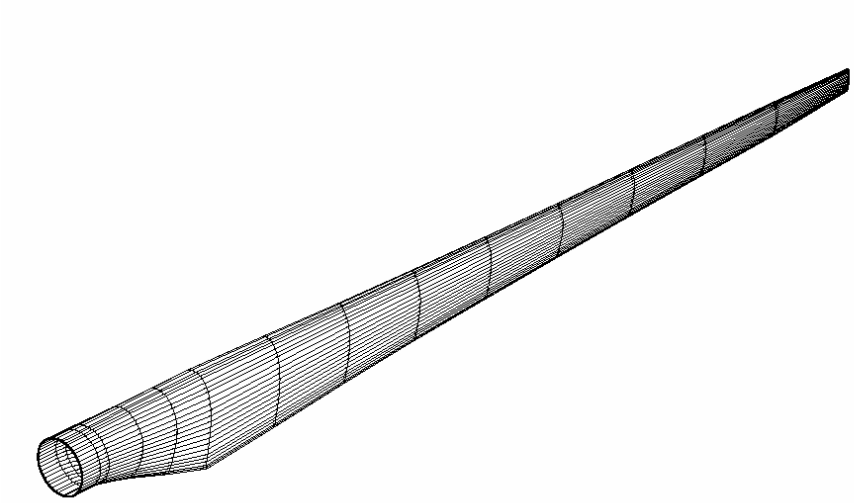

Figure 2.3 – wind turbine blade divided into elements [11]

The lift and drag forces acting on a blade element are determined using airfoil characteristics data which are presented as lift and drag coefficients. In order to determine the lift and drag from the airfoil data, the relative velocity over the airfoil must be determined. For a given rotor blade element, the velocity over the airfoil is made up of two components, the wind and a tangential velocity (the speed in which the blades are turning). Adding the two velocity vectors yields the flow of air over an airfoil.

The average rotational flow over the rotor plane due to rotor wake is $\frac{\omega}{2}$ [5]. The blade's rotational speed is Ω. The average tangential speed of the flow at the radial location *r* on the blade is:

$$V_t = \Omega r + \frac{1}{2}\omega r = \Omega r\left(1 + a'\right) \qquad 2.12$$

The axial velocity just before the rotor is:

$$V_2 = V_1(1-a) \qquad 2.5$$

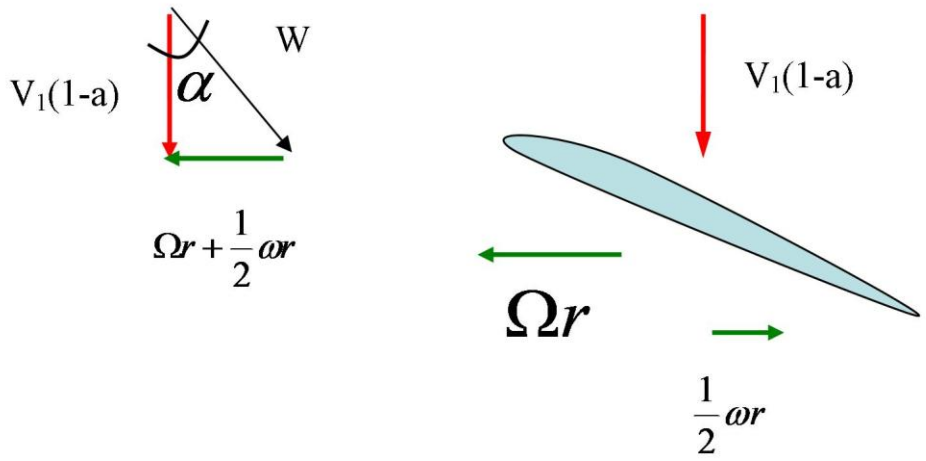

Figure 2.4 – Schematic of relative wind flow past blade

Adding the velocity vectors, shown in Fig. 2.4, results in the relative airflow over the airfoil. α is the angle of attack, at which the flow over the blade is changed from the wind due to the rotation of the blades and the flow induced by the wake. Lift and drag coefficients are found using airfoil data tables and the angle of attack.

$$W = \frac{V(1-a)}{\cos\alpha} \qquad 2.13$$

$$\tan\alpha = \frac{\Omega r(1+a')}{V(1-a)} = \lambda_r \frac{(1+a')}{(1-a)} \qquad 2.14$$

where local tip speed ratio, λ_r, is defined as

$$\lambda_r = \frac{\Omega r}{V} \qquad 2.15$$

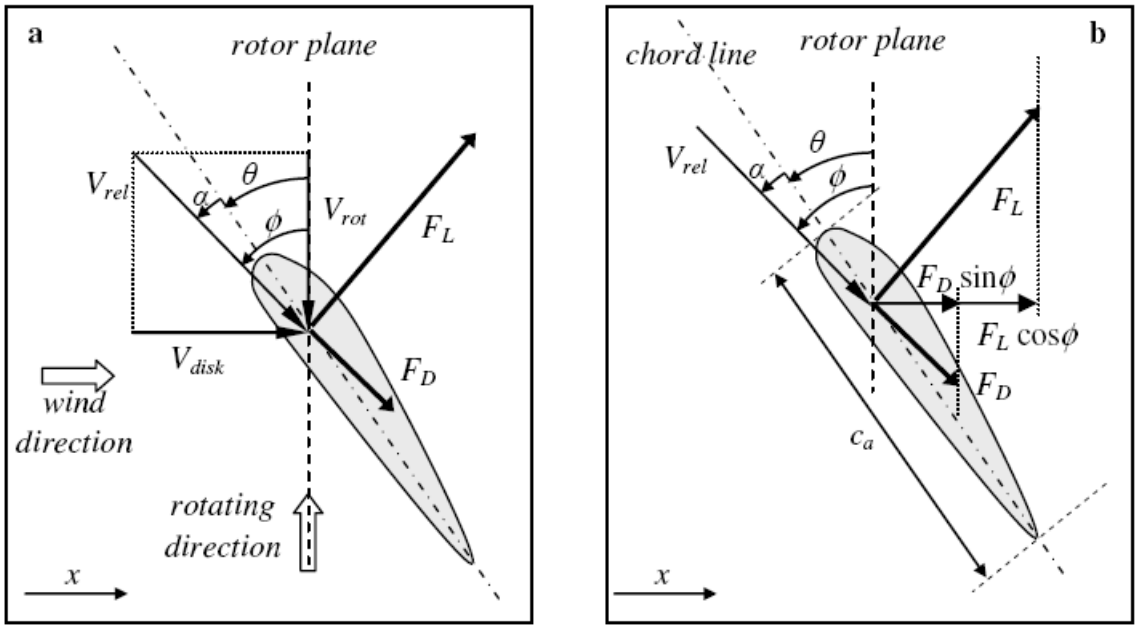

Figure 2.5 – airfoil – Lift and Drag Forces [11]

With the lift and drag coefficients and the angle of the relative wind the axial and tangential forces are found in the following equations.

$$dF_x = dL\sin\alpha + dD\cos\alpha \qquad 2.16$$

$$dF_\theta = dL\cos\alpha - dD\sin\alpha \qquad 2.17$$

The lift and drag forces are obtained from:

$$dL = C_L \frac{1}{2}\rho W^2 c dr \qquad 2.18$$

$$dD = C_D \frac{1}{2}\rho W^2 c dr \qquad 2.19$$

where

C_L is the lift coefficient of the airfoil

C_D is the drag coefficient of the airfoil

Assuming identical conditions for a multi-blade turbine, combining the above (B represents the number of blades):

$$dF_x = B\frac{1}{2}\rho W^2 \left(C_L \sin\alpha + C_D \cos\alpha\right) c\,dr \qquad 2.20$$

$$dF_\theta = B\frac{1}{2}\rho W^2 \left(C_L \cos\alpha - C_D \sin\alpha\right) c\,dr \qquad 2.21$$

Using the tangential force to determine the torque we get:

$$dT = B\frac{1}{2}\rho W^2 \left(C_L \cos\alpha - C_D \sin\alpha\right) c\,r\,dr \qquad 2.22$$

Combining the equations for the axial force and torque from the momentum theory (2.7 and 2.11) with the above, the axial force and torque can be obtained using airfoil data in an iterative procedure.

2.1.3 – WT Perf Iteration

With the axial and tangential force defined from both the momentum and blade element equations, the two methods are used to determine the induced flow.

$$\frac{a}{1-a} = \frac{\sigma'}{4Q\cos^2\alpha}\left(C_L \sin\alpha + C_D \cos\alpha\right) \qquad 2.23$$

$$\frac{a'}{1-a} = \frac{\sigma'}{4Q\lambda_r \cos^2 \alpha} \left(C_L \cos \alpha - C_D \sin \alpha \right) \qquad 2.24$$

The letter Q in the above equations represents correction factors that can include: tip loss, skew wake, shear, yaw and tilt. Please see the WT_Perf manual for more descriptions on correction factors. [36]

WT_Perf begins iteration assuming there is no induction effect. It finds the angle of attack (Eq. 2.14) then finds the lift and drag coefficients from airfoil data [36]. It then uses the Lift and Drag to find the induced velocity. With new values for induction, it begins the process again until the induced velocity converges.

Once the induction value is determined WT_Perf uses the average value of induction for the entire blade to calculate the correction factors. WT_Perf then begins the entire process again, recalculating the induced velocity with the corrected values. It repeats the calculation cycle until the corrected values converge.

Section 2.2 – Kane Method

2.2.1 – Brief Overview of Kane Method

Kane Method combines the advantages of both Newton-Euler and Lagrange methods of multi-body dynamics without the disadvantages. Kane method employs the use of generalized forces which avoids the need to define interactive and constraint forces between bodies (as is the case for Newton-Euler method). Kane's method also avoids the use of Energy functions (which arise with the Lagrange method). Differentiation needed for velocity and acceleration can be performed by algorithms based on vector products. Therefore, Kane's method lends itself for use with numerical computation. [7]

Kane's method for a system of bodies uses generalized coordinates to define movement. Forces are balanced in an inertial reference frame by the following equation: [12]

$$F_r + F_r^* = 0 \qquad \text{r=1,2,…\#DOF} \qquad 2.24$$

where F_r = generalized forces and F_r^* = generalized inertial forces.

In FAST, the generalized inertial forces in our wind turbine model is the sum of all the forces for all the bodies that have mass: [12]

$$F_r^* = F_r^*|_{Tower} + F_r^*|_{Nacelle} + F_r^*|_{Hub} + F_r^*|_{Blades} + F_r^*|_{Platform} \qquad 2.25$$

For the generalized active forces, FAST sums the aerodynamic forces, hydrodynamic forces, gravity, drive train forces and elastic forces [12, 18]:

$$F_r^* = F_r\ |_{Aero} + F_r\ |_{Gravity} + F_r\ |_{Elastic} + F_r\ |_{Drivetrain} + F_r\ |_{Hydro} + F_r\ |_{Mooring} \qquad 2.26$$

Coordinate systems give us reference frames to different sub-systems. The sub-systems are related and affect each other. It is easier to write an equation of motion for a specific sub-system, than for the whole system. Once an equation for a specific sub-system is written, using a local coordinate system, it can be related to the global coordinate system through coordinate transformations. It is at the different coordinate systems or reference frames that Kane Method defines each DOF or generalized coordinate. Once generalized coordinates are defined, derivatives define the partial velocities and accelerations. Once partial velocities and accelerations are determined, inertia forces can be calculated and then balanced with generalized active forces.

2.2.2 – Brief Procedure of Kane Method:

The method consists of the following six steps:

1. Define the model. Define rigid bodies or reference frames and points of interest.
2. Define Degrees of Freedom (DOF) or generalized coordinates.
3. Define generalized speeds, partial velocities and partial accelerations.
4. Define mass and inertias of bodies.
5. Define generalized active forces.
6. Solve $F_r + F_r^* = 0$

2.2.3 - FAST Degrees of Freedom (DOF)

FAST models a wind turbine with 9 rigid bodies and 4 flexible bodies: [12,13,18,20,21]

Below is a list of the rigid bodies:

1. earth
2. support platform
3. base plate

4. nacelle
5. armature
6. gears
7. hub
8. tail
9. structure furling with rotor.

The flexible bodies are:
1. tower
2. drive shaft
3. blades (in-plane)
4. blades (flapwise)

FAST uses nine different coordinate systems, to define input and output parameters which are defined below.

2.2.4 - Coordinate Systems

The platform reference frame is located at the center of mass of the platform, which is below the still water line, i.e. below the surface of the water.

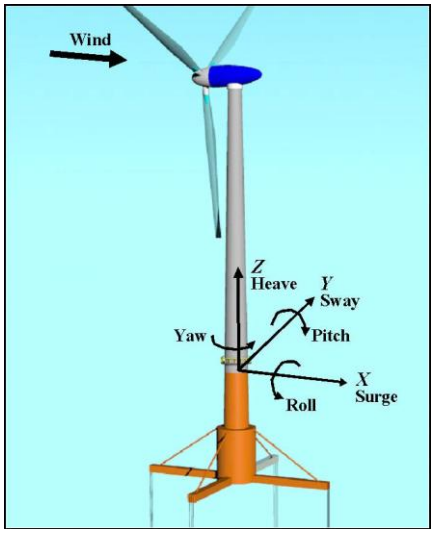

Figure 2.6 - platform coordinate system [18]

The inertial reference frame origin is used to define the translational motions of the platform. The tower base coordinate system is fixed at the center of the tower base (where it is connected to the support platform).

Figure 2.7- tower-base coordinate system [21]

The tower top coordinate system is located at the top of the tower. It translates and rotates as the tower bends and the platform moves, but it does not yaw with the nacelle.

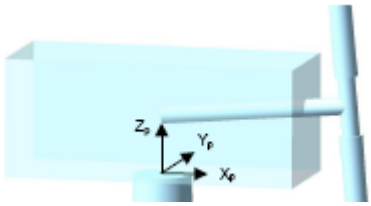

Figure 2.8 - tower-top/base-plate coordinate system [21]

The nacelle/yaw coordinate system is located at the tower-top/base-plate but is able to rotate or yaw.

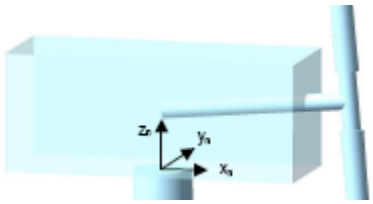

Figure 2.9 - nacelle/yaw coordinate system [21]

The shaft coordinate system is located at the intersection of the rotor and nacelle coordinate system. The shaft coordinate system does not rotate with the rotor. The azimuth coordinate system rotates with the rotor. For three-bladed rotors, blade 3 is ahead of blade 2, which is ahead of blade 1, so that the order of blades passing through a given azimuth is 3-2-1-repeat. When blade one is pointing up the azimuth and shaft coordinate system is identical.

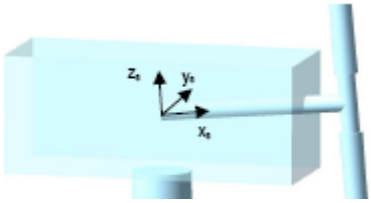

Figure 2.10 - shaft and azimuth coordinate system [21]

The hub coordinate system rotates with the rotor and teeters with two-bladed models.

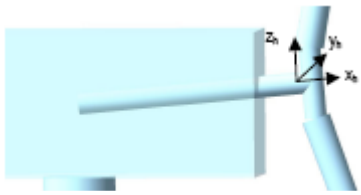

Figure 2.11 - hub coordinate system [21]

The coned coordinate system is located at the hub coordinate system. It does not pitch with the blades but describes how the blades angle from the tower.

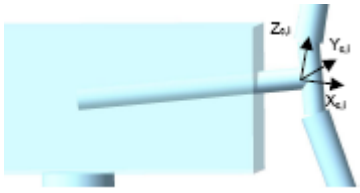

Figure 2.12 - coned coordinate system [21]

The blade coordinate system is the same as the coned coordinate system except that they pitch with the blades and their origins are at the blade root.

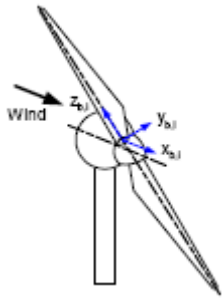

Figure 2.13 - blade coordinate system [21]

The rigid and flexible bodies relate to each other through 22 degrees of freedom (DOF) for a two-bladed machine, and 24 DOF for a three-bladed machine.

Table 2.1 – Degrees of Freedom for two and three blades [21]

For a two-bladed turbine:	For a three-bladed turbine:
platform translation and rotation (6 DOF)	platform translation and rotation (6 DOF)
tower flexibility (4 DOF)	tower flexibility (4 DOF)
nacelle yaw (1 DOF)	nacelle yaw (1 DOF)
variable generator and rotor speeds (2 DOF)	variable generator and rotor speeds (2 DOF)
blade teetering (1 DOF)	
blade flexibility (6 DOF)	blade flexibility (9 DOF)
rotor-furl (1 DOF)	rotor-furl (1 DOF)
tail-furl (1 DOF)	tail-furl (1 DOF)

Once the reference frames are defined, coordinate system transformations must be defined in order to relate the various coordinate systems and the degrees of freedom defined in each coordinate system to one coordinate system.

2.2.5 – Coordinate System Transformations

Coordinate systems are used to define the motion of objects in a reference frame. Each system represents a change in angular and translation orientation. Once all the systems are defined, a coordinate transformation can be developed. In FAST, coordinate systems are right-handed and all angular rotations are positive. The FAST_AD manual defines the coordinate transforms used in FAST [12].

An example of a coordinate system transformation is from the Nacelle/yaw to the tower-top: [12]

$$\begin{Bmatrix} x_p \\ y_p \\ z_p \end{Bmatrix} = \begin{bmatrix} cq_6 & 0 & sq_6 \\ 0 & 1 & 0 \\ -sq_6 & 0 & cq_6 \end{bmatrix} \begin{Bmatrix} x_n \\ y_n \\ z_n \end{Bmatrix} \quad \text{where } q_6 \text{ is the yaw angle} \qquad 2.27$$

The following notation is used in the above equation:

„c' = cosine and 's'=sine

x_p, y_p, z_p - tower-top/base-plate coordinate system

x_n, y_n, z_n – nacelle/yaw coordinate system

However, with the addition of the floating platform, 6 degrees of freedom have been added to the model. A floating platform implies that the wind turbine model is no longer rigidly connected to the inertial reference frame. Not being rigidly connected to the inertial reference frame means that the entire wind turbine model is allowed to translate

(surge, sway, heave) and rotate (roll, pitch, yaw). With this additional movement transformation matrices for the platform, tower-top, and blades have been changed from previous versions of FAST. Below is a representation of matrix transformation used to describe the transformation from platform, to the inertial reference frame. Small angle theory is used. More detailed explanation can be found in Jonkman [18].

$$\begin{Bmatrix} x \\ y \\ z \end{Bmatrix} = \begin{bmatrix} \dfrac{\theta_1^2\sqrt{1+\theta_1^2+\theta_2^2+\theta_3^2}+\theta_2^2+\theta_3^2}{(\theta_1^2+\theta_2^2+\theta_3^2)\sqrt{1+\theta_1^2+\theta_2^2+\theta_3^2}} & \dfrac{-\theta_3(\theta_1^2+\theta_2^2+\theta_3^2)+\theta_1\theta_2(\sqrt{1+\theta_1^2+\theta_2^2+\theta_3^2}-1)}{(\theta_1^2+\theta_2^2+\theta_3^2)\sqrt{1+\theta_1^2+\theta_2^2+\theta_3^2}} \\ \dfrac{\theta_2(\theta_1^2+\theta_2^2+\theta_3^2)+\theta_1\theta_3(\sqrt{1+\theta_1^2+\theta_2^2+\theta_3^2}-1)}{(\theta_1^2+\theta_2^2+\theta_3^2)\sqrt{1+\theta_1^2+\theta_2^2+\theta_3^2}} & \dfrac{\theta_3(\theta_1^2+\theta_2^2+\theta_3^2)+\theta_1\theta_2(\sqrt{1+\theta_1^2+\theta_2^2+\theta_3^2}-1)}{(\theta_1^2+\theta_2^2+\theta_3^2)\sqrt{1+\theta_1^2+\theta_2^2+\theta_3^2}} \\ \dfrac{\theta_1^2+\theta_1^2\sqrt{1+\theta_1^2+\theta_2^2+\theta_3^2}+\theta_3^2}{(\theta_1^2+\theta_2^2+\theta_3^2)\sqrt{1+\theta_1^2+\theta_2^2+\theta_3^2}} & \dfrac{-\theta_1(\theta_1^2+\theta_2^2+\theta_3^2)+\theta_2\theta_3(\sqrt{1+\theta_1^2+\theta_2^2+\theta_3^2}-1)}{(\theta_1^2+\theta_2^2+\theta_3^2)\sqrt{1+\theta_1^2+\theta_2^2+\theta_3^2}} \\ \dfrac{-\theta_2(\theta_1^2+\theta_2^2+\theta_3^2)+\theta_1\theta_3(\sqrt{1+\theta_1^2+\theta_2^2+\theta_3^2}-1)}{(\theta_1^2+\theta_2^2+\theta_3^2)\sqrt{1+\theta_1^2+\theta_2^2+\theta_3^2}} & \dfrac{\theta_1(\theta_1^2+\theta_2^2+\theta_3^2)+\theta_2\theta_3(\sqrt{1+\theta_1^2+\theta_2^2+\theta_3^2}-1)}{(\theta_1^2+\theta_2^2+\theta_3^2)\sqrt{1+\theta_1^2+\theta_2^2+\theta_3^2}} \\ \dfrac{\theta_1^2+\theta_2^2+\theta_3^2\sqrt{1+\theta_1^2+\theta_2^2+\theta_3^2}}{(\theta_1^2+\theta_2^2+\theta_3^2)\sqrt{1+\theta_1^2+\theta_2^2+\theta_3^2}} & \end{bmatrix} \begin{Bmatrix} X \\ Y \\ Z \end{Bmatrix}$$

Equation 2.28

2.2.6 – Generalized Coordinates, Generalized Speeds, and Partial Velocities and Accelerations:

In Kane's method a generalized coordinate, or Degree of Freedom, is the building block to describe motion. The generalized coordinates define the configuration of the wind turbine. A generalized coordinate is a single valued function of time that describes the

location in a particular coordinate system, and satisfies the constraints of other generalized coordinates that describe the motion of the system. A good example of a generalized coordinate is the yaw angle. The generalized coordinate of the yaw angle defines how the wind turbine is yawed, or angled into the wind. The derivative of the generalized coordinate defines how the different parts of the wind turbine move and interact with each other. Coordinate derivatives which are linear combinations of other coordinate derivatives are called generalized speeds.

Once the dynamic system is defined as a series of rigid body reference frames, related by several degrees of freedom, or generalized coordinates, the kinematics can be defined. [12]. Vectors from all coordinate systems can be related to a common coordinate system (the inertia reference frame).

For example, the angular velocity of the Nacelle can be defined by angular velocity of the base plate in the inertial reference frame as shown below [12, 21]:

$$^{E}\omega^{B} = \dot{\theta}_8 x_i - \dot{\theta}_7 y_i \qquad 2.29$$

$\dot{\theta}_7$ is the change in rotation about y_i

$\dot{\theta}_8$ is the change in rotation about x_i

x_i, y_i are the „x' and „y' directions in the inertial reference frame

where:

$$\theta_7 = -(\alpha_7 q_7 + \alpha_9 q_9)$$

$$\theta_8 = \alpha_8 q_8 + \alpha_{10} q_{10}$$

and,

$$\alpha_7 = \frac{\partial \phi_{1T}}{\partial h} \qquad \alpha_9 = \frac{\partial \phi_{2T}}{\partial h}$$
$$\alpha_8 = \frac{\partial \phi_{1T}}{\partial h} \qquad \alpha_{10} = \frac{\partial \phi_{2T}}{\partial h}$$

In the above equations $q_{7,}$ $q_{8,}$ $q_{9,}$ q_{10} are the generalized coordinates of the tower in the longitudinal and latitude directions.

The angular velocity of the nacelle relative to the base plate is: [12,21]

$$^{B}\omega^{N} = \dot{q}_6 z_n \qquad 2.30$$

where q_6 is the yaw angle and
z_n is the ‚z' direction nacelle/yaw coordinate system

Combining the two yields the angular velocity of the nacelle in the inertial reference frame: [12,21]

$$^{E}\omega^{N} = {}^{E}\omega^{B} + {}^{B}\omega^{N} = \dot{\theta}_8 x_i - \dot{\theta}_7 y_i + \dot{q}_6 z_n \qquad 2.31$$

Once the angular velocities are defined, linear velocities are found in a similar manner using the geometry of the system. See [12] for more information. Once the model has been defined as a series of different coordinate systems, or reference frames, and the location of each defined by a generalized coordinate, the velocity and acceleration can be found [12]. Transforming all the equations of motion to the reference frame leads to the equations below for velocity and acceleration:

$$^{E}v^{S} = \sum_{r=1}^{\#DOF} {}^{E}v^{S}\dot{q}_r + {}^{E}v_t{}^{S} \qquad 2.32$$

$$ {}^{E}a^{S} = \sum_{r=1}^{\#DOF} \frac{d}{dt}{}^{E}a^{S}\dot{q}_r + \frac{d}{dt}{}^{E}a_t{}^{S} \qquad 2.33 $$

2.2.7 – Generalized Inertia Forces

The motion that results when forces act on a material system depends not only on the forces, but also on the constitution of the system. In particular, the manner in which mass is distributed throughout a system generally affects the behavior of the system, [9].

Generalized inertia forces include the effects of linearly and angular accelerating mass. When using the Kane method the equation for generalized inertia forces is, [6]:

$$ F_r^* = \sum_r \left(-m \cdot {}^{N}\vec{a}^{A} \cdot {}^{N}\vec{v}_r{}^{A} - \left({}^{N}\vec{\alpha}^{A} \cdot \bar{\bar{I}} + {}^{N}\vec{\omega}^{A} \times \bar{\bar{I}} \cdot {}^{N}\vec{\omega}^{A} \right) \cdot {}^{N}\vec{\omega}_r{}^{A} \right) \qquad 2.34 $$

Every system within the floating wind turbine has mass, including the blades, hub, nacelle, tower, platform and mooring system, [12,18].

$$ F_r^* = F_r^*|_{Tower} + F_r^*|_{Nacelle} + F_r^*|_{Hub} + F_r^*|_{Blades} + F_r^*|_{Platform} + F_r^*|_{Mooring} \qquad 2.35 $$

Using our example of the yaw movement, the inertia force of the nacelle is defined as: [12]:

$$ F_r^*|_{Nacelle} = -m_{nacelle} \cdot {}^{E}\vec{a}^{D} \cdot {}^{E}\vec{v}_r{}^{D} - \left({}^{E}\vec{\alpha}^{N} \cdot \bar{\bar{I}}_{Nacelle} + {}^{E}\vec{\omega}^{N} \times \bar{\bar{I}}_{Nacelle} \cdot {}^{E}\vec{\omega}^{N} \right) \cdot {}^{E}\vec{\omega}_r{}^{N} \qquad 2.36 $$

More information regarding generalized inertia forces can be found in [12].

2.2.8 – Generalized Active Forces

The generalized active forces cause the wind turbine to move. As mentioned earlier, they are, [12,18]:

$$F_r = F_r|_{Aero} + F_r|_{Gravity} + F_r|_{Elastic} + F_r|_{Drivetrain} + F_r|_{Hydro} + F_r|_{Mooring} \qquad 2.38$$

In this next section, we briefly describe the different types of generalized active forces.

2.2.9 – Elastic Restoring Forces

The bending of the tower and blades produces forces that restore the tower and blades to the undeflected position. FAST calculates these forces using potential energy, V [12] ,

$$F_r|_{Elastic} = \frac{\partial V}{\partial q_r} \qquad 2.39$$

where q_r is the location of the deflection

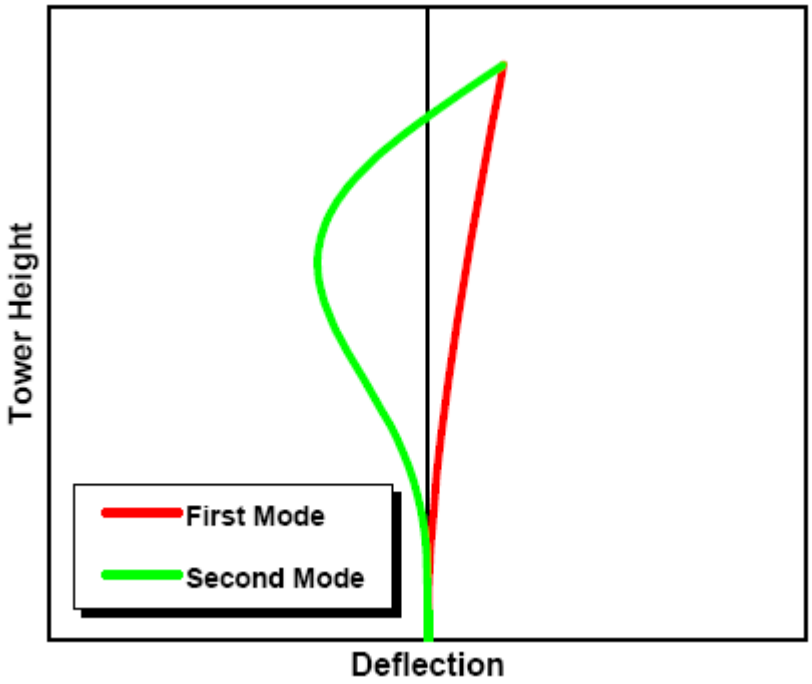

Figure 2.14 – Tower Mode Shapes [21]

For the tower the potential energy is, [12]:

$$V_{tower} = \frac{1}{2}\left(k_{77}q_7^2 + k_{88}q_8^2\right) + \frac{1}{2}\left(k_{99}q_9^2 + k_{1010}q_{10}^2\right) \qquad 2.40$$

where $k_{77,}$ $k_{88,}$ $k_{99,}$ k_{1010} are the tower stiffness, and $q_{7,}$ $q_{8,}$ $q_{9,}$ q_{10} are the generalized coordinates of the tower in the longitudinal and latitude directions. The tower stiffness is calculated using the stiffness of the tower element, gravity, and the mass of everything above the tower element, [12].

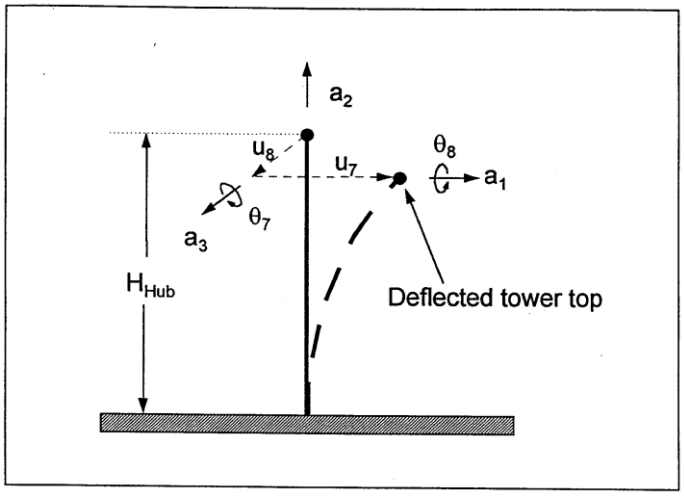

Figure 2.15 – Tower Bending and Location of Tower Top [12]

For the blades: [12]

$$V_{Blade1} = k_{11}q_1^2 + 2k_{12}q_1 q_2 + k_{22}q_2^2 + k_{33}q_3^2 \qquad 2.41$$

For this discussion let q_1 represent the first flapwise tip deflection, q_2 the second flapwise tip deflection and q_3 the edgewise tip deflection. For a more detailed description of the elastic forces see references [12, 21].

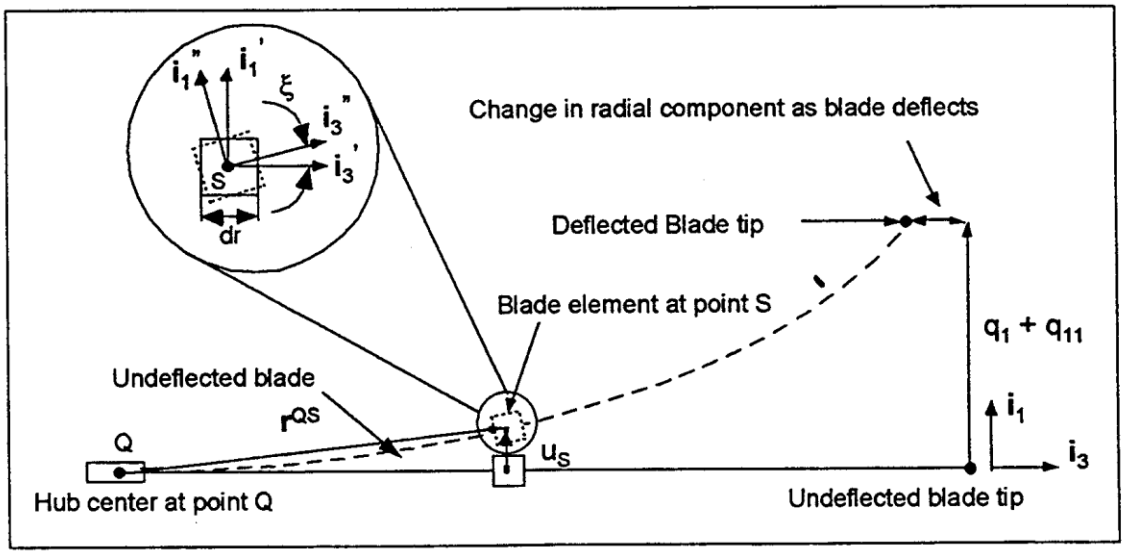

Figure 2.16 – Blade Bending in Flapwise Direction [12]

2.2.10 – Drive Train Loading

Drive train loading is experienced when the drive train and the rotor are out of sync. This can happen for a variety of reasons. FAST gives the user many options to model such occasions. A few examples of these options are: normal start-up sequences, normal shutdown sequences, and safety and protection functions. We will not be examining these models in our analysis. See the FAST manuals for further investigation.[21]

2.2.11 – Hydrodynamic Model

Total loads on the platform are represented by [18]:

$$F_i^{Platform} = -A_{ij}\ddot{q}_j + F_i^{Hydro} + F_i^{Lines} \qquad 2.42$$

A_{ij} - the ij component of the impulsive hydrodynamic-added-mass matrix
F_i^{Hydro} - Hydrodynamic Loads on support platform
F_i^{Lines} - mooring lines load

Consistent with FAST, we assumed that the floating support platform is represented well as a six-DOF rigid body with three small rotational displacements. We also assumed linearity. Linearity implies that amplitudes of incident waves are much smaller than their wavelengths. This allows the use of Airy Theory, and excludes breaking waves. Assuming linearity also implies that translational displacements are small compared to the characteristic length (size of body). This allows the hydrodynamic equations to be split into three separate equations: diffraction, radiation, and static. Finally, the assumption of linearity allows the use of superposition. [18]

$$F_i^{Hydro} = F_i^{Waves} + \rho g V_0 \delta_{i3} - C_{ij}^{Hydrostatic} q_j - \int_0^t K_{ij}(t-\tau)\dot{q}_j(\tau)\,d\tau \qquad 2.43$$

Diffraction loads - F_i^{Waves}

Hydrostatic loads - $\rho g V_0 \delta_{i3} - C_{ij}^{Hydrostatic} q_j$

Radiation loads - $\int_0^t K_{ij}(t-\tau)\dot{q}_j(\tau)\,d\tau$

Airy wave theory uses a potential flow approach to describe the motion of gravity waves on a fluid surface. For the diffraction and radiation potential-flow theory applies for all but the extreme wave conditions. In view of the validity of potential-flow theory across many conditions, the potential flow problem was solved using WAMIT [18]. Higher order potential-flow solutions such as mean and slow drift and cresting waves were not included in this model.

2.2.12 – Diffraction Loads

Diffraction considers loads associated with incident waves exciting the platform. Results for diffraction solutions are given in terms of wave-frequency and direction dependent hydrodynamic wave excitation vector, [18,13].

2.2.13 - Hydrostatic Loads

The equation for hydrostatic loads is: [18,13]

$$F^{Hydrostatic}(\omega) = \rho g V_0 \delta_{i3} - C_{ij}^{Hydrostatic} q_j \qquad 2.44$$

where
ρ is the density of water
g- gravity
V_0 - displaced volume of liquid
δ_{i3} - is the (i,3) component of the Kronecker-Delta function
$C_{ij}^{Hydrostatic}$ - - is the (i,j) component of the linear hydrostatic-restoring matrix of water-plane and center of buoyancy

The first term on the right hand side is the buoyancy force due to the displaced fluid of the platform. The buoyancy force is directed upward. The second term on the right-hand-side represents the force and moment as the platform is displaced, [18,13].

2.2.14 - Radiation loads

For this analysis, radiation considers the oscillation of the platform and the wave it creates, or radiates. Solutions to radiation are given in terms of oscillation-frequency-dependant hydrodynamic – added mass and –damping matrices. [18] Figure 2.6 shows

the flow of information for calculation of the hydrodynamic forces on the platform. The user specifies the platform geometry. WAMIT calculates the excitation forces and mass, damping and stiffness matrices. The latter is the matrix of restoring forces. HydroDyn generates a time history for a given power spectral density of the waves.

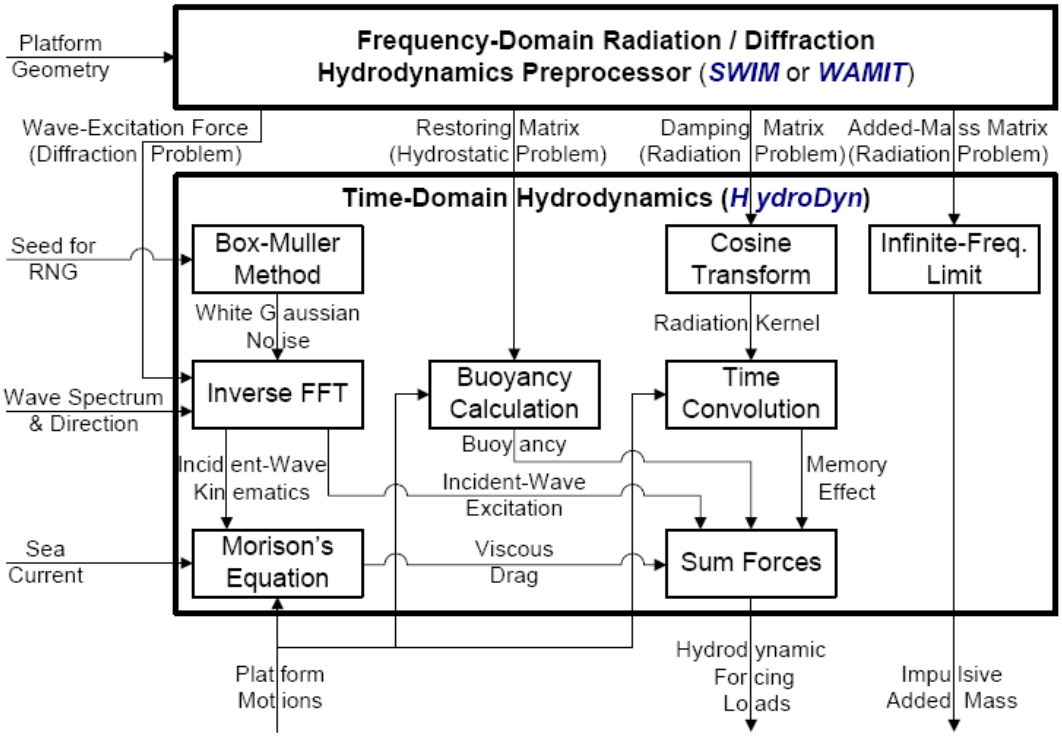

Figure 2.17 – Flow Chart of Hydrodynamic calculations [18]

Section 2.2.15 – Mooring System

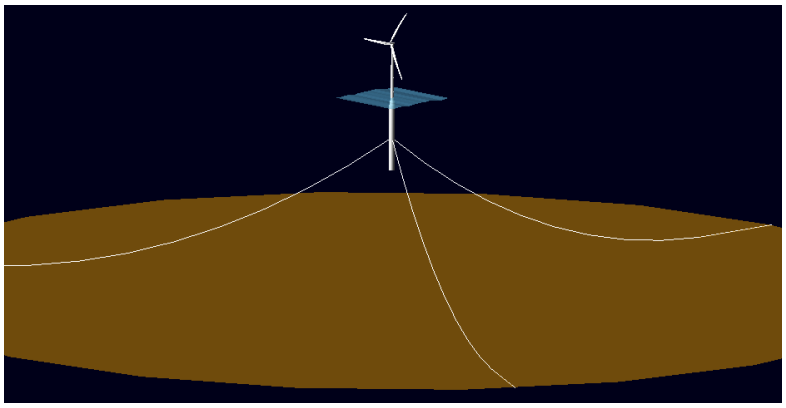

Figure 2.18 – Mooring configuration for Spar Buoy [13]

Below is a description of the mooring system used in the OC3/StatoilHydro model. It is described here to show one approach in modeling the mooring system of a floating platform wind turbine. This mooring system model is not the same as the mooring system models used for the ITI Barge or the MIT/NREL TLP floating platforms. For descriptions of these models, refer to [18, 31].

The spar buoy is held in position by 3 catenary lines. The first catenary line is located on the x-z axis. The following 2 catenary lines are located at 120 degrees on either side. The catenary lines are located 70 meters below the SWL (still water line). The StatoilHydro's platform uses a "crowfoot" (delta connection) to attach the lines to the platform. For our model, the crowfoot is replaced with a yaw spring to achieve proper stiffness. Catenary lines are normally constructed with multi-segment lines of chains, steel, and multi-fiber materials. For our model, the lines are assumed to be made of a homogeneous material. The mooring model ignores inertia and damping. The anchors

are located at a depth of 320 meters below the SWL, at a radius of 853.87 meters from the centerline of the platform, [13].

Modeling mooring systems can be difficult. Our model uses the work done for OC3.[13] The work presented in that paper uses a linear and nonlinear model. The linear model is only valid for small displacements and follows the equation: [18,13]

$$F_i^{Lines}(q) = F_i^{Lines,0} - C_{ij}^{Lines} q_j \qquad 2.45$$

where $F_i^{Lines}(q)$ is the *i*th component of the total mooring system
C_{ij}^{Lines} is the component of the linearized restoring matrix
$F_i^{Lines,0}$ is the pre-tension at the fairleads from the weight of the mooring lines not resting on the sea floor.
q_j is the *j*th DOF.

A linearization analysis was performed by perturbing one DOF and measuring the result. This analysis resulted in values for $F_i^{Lines,0}$ and C_{ij}^{Lines}. With values for $F_i^{Lines,0}$ and C_{ij}^{Lines}, load displacement relationships were found using discrete combinations of the displacements. Results can be found in, "Definition of the Floating System for PhaseIV of OC3." [13]

Chapter 3

Model Description

3.1 - Rayleigh Wind Distribution

The Rayleigh Wind Speed Distribution recommended by the IEC 61400-1 wind turbine design standard, [30], was used in this study. The Rayleigh distribution is defined by the probability density function, PDF(V), and cumulative density function, CDF(V), where V is the hub-height wind speed (10m/s):

$$PDF(V) = \frac{\pi V}{2V_{avg}^2} e^{-\pi\left(\frac{V}{2V_{avg}}\right)^2} \qquad 3.1$$

$$CDF(V) = 1 - e^{-\pi\left(\frac{V}{2V_{avg}}\right)^2} \qquad 3.2$$

Figures 3.1 and 3.2 show the cumulative wind distribution and the probability density function of the wind velocity.

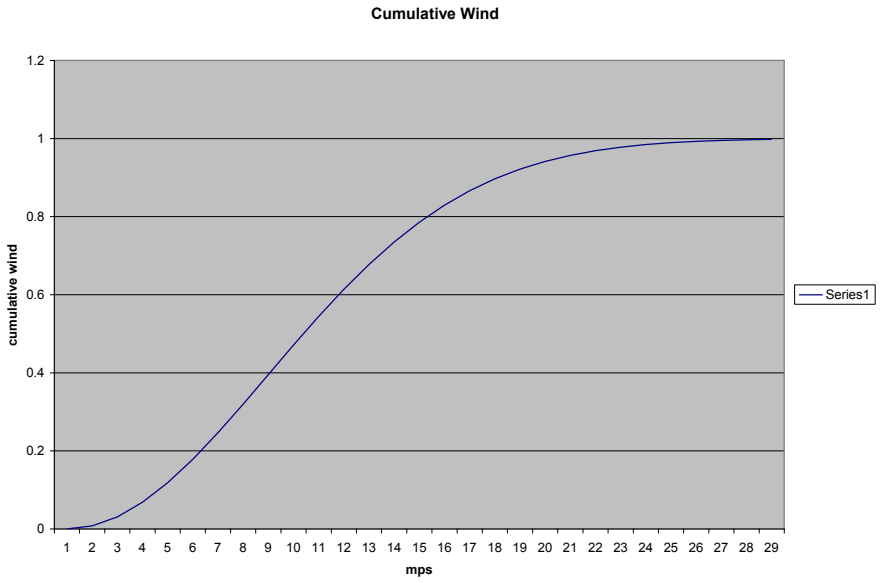

Figure 3.1 – Cumulative wind distribution recommended by the IEC 61400-1

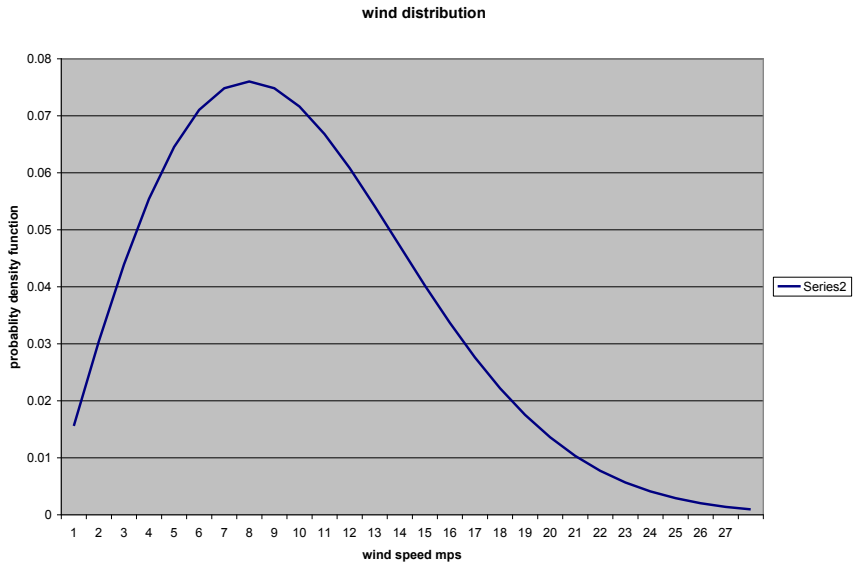

Figure 3.2 –Rayleigh Wind Speed Distribution recommended by the IEC 61400-1

3.2 - Model Description:

Figure 3.3 shows a model of the three-bladed wind turbine system consisting of the tower, platform (including mooring system), nacelle and the blades. This model was developed by using ADAMS. The inertial reference frame defines the point about which the support platform moves. The platform can translate (surge, sway, heave) and rotate (pitch, roll, yaw). The tower is rigidly connected to the platform and moves with the platform. The tower is flexible. The flexibility of the tower is represented in 4 mode shapes, with the 1st and 2nd bending moments in the longitudinal and transverse directions. At the tower top, the turbine base plate is rigidly attached, and moves with the top of the tower. The nacelle and yaw bearing is attached to the base plate. The nacelle houses the generator and gearbox.

Figure 3.3 – OC3 ADAMS Model [13]

The yaw bearing allows everything on top of the tower to rotate with the wind. A low speed shaft connects the rotor to the gearbox. For two-bladed machines the blades are allowed to teeter. The teeter joint is located between the low speed shaft and the rotor. The blades are made up of sections with different properties. The blades are allowed to be structurally pre-twisted. The blades are flexible. The flexibility is described by two modes of vibration out of the plane of rotation and one mode in the plane of rotation. [12,13,18,20,21] For analysis NREL's 5MW Reference Wind Turbine for Offshore System Development was used,[30]. Three different floating platforms were considered: ITI Energy barge, MIT/NREL's Tension Leg Platform, and OC3/Hywind's Spar buoy, [13,18]. The wind turbine for all three floating platform models remains the same; only the tower, control systems, and platform change. The wind turbine is a conventional three-bladed upwind variable-speed variable blade-pitch-to-feather-controlled turbine (for two-bladed analysis one blade was removed and teetering added).

Section 3.3 – Model Properties

The turbine uses some broad design information from turbine manufacturers, with heavy emphasis on the REpower 5MW [20] machine. Detailed data on the Repower machine was unavailable. Conceptual models from the WindPACT, RECOFF, and DOWEC research projects were used to create a representative composite 5MW machine similar to the REpower turbine. This model is commonly referred to as the NREL's offshore 5-MW baseline wind turbine.

The NREL offshore 5-MW baseline wind turbine has been adopted by the U.S. DOE's Wind & Hydropower Technologies Program, European Union's UpWind, and the International Energy Agency (IEA) Wind Annex XXIII Subtask 2 Offshore Code Comparison Collaboration (OC3) research programs, and has been and will likely continue to be used as a reference by research teams throughout the world.

In the following sections properties of the blades, hub and nacelle, drivetrain, and the three platforms (including tower modifications) used is given. The support structures (tower, platform) for each floating platform model have changed, and will be described separately. The towers for the ITI Barge and MIT/NREL TLP are the same, only the OC3/StatioHydro tower is different.

Section 3.3.1 – Blade Geometry and Structural Properties

The blades are 61.5 meters long. Because the blades used in our analysis have a mass is 17,740 kg [20]. The nominal second mass moment of inertia, nominal first mass moment of inertia, and the nominal radial Center of Mass location of each blade are 11,776,047 kg•m^2, 363,231 kg•m, and 20.475 m with respect to (w.r.t.) the blade root, respectively. Table 3.2 lists the undistributed blade structural properties. The structural properties of the blade are used by FAST to calculate loads and deflections and can be found in the NRELOffshrBsline5MW_Blade.dat file located in the AeroData file.

Table 3.1 – Undistributed Blade Structural Properties [20]

Length (w.r.t. Root Along Preconed Axis)	61.5m
Mass Scaling Factor	4.536%
Overall (Integrated) Mass	17,740kg
Second Mass Moment of Inertia (w.r.t. Root)	11,776,047kg•m^2
First Mass Moment of Inertia (w.r.t. Root)	363,231kg•m
CM Location (w.r.t. Root along Preconed Axis)	20.475m
Structural-Damping Ratio (All Modes)	0.477465%

Actual wind turbine blades have prebend. Prebend is used to increase tower clearance. Simulation tools used in this analysis are not equipped to model blades with prebend. Instead an upwind precone of 2.5 degrees was used to increase tower clearance. Precone increases the angle where the rotor attaches to the hub. A visual reference for precone can be seen in Fig. 3.4. Using precone reduces the swept area, hence the exact rotor diameter in the turbine specifications (assuming that the blades are undeflected) is set at (126 m) × cos(2.5°) = 125.88 m and the corresponding actual swept area is (π/4) × (125.88 m)^2 = 12,445.3 m^2.

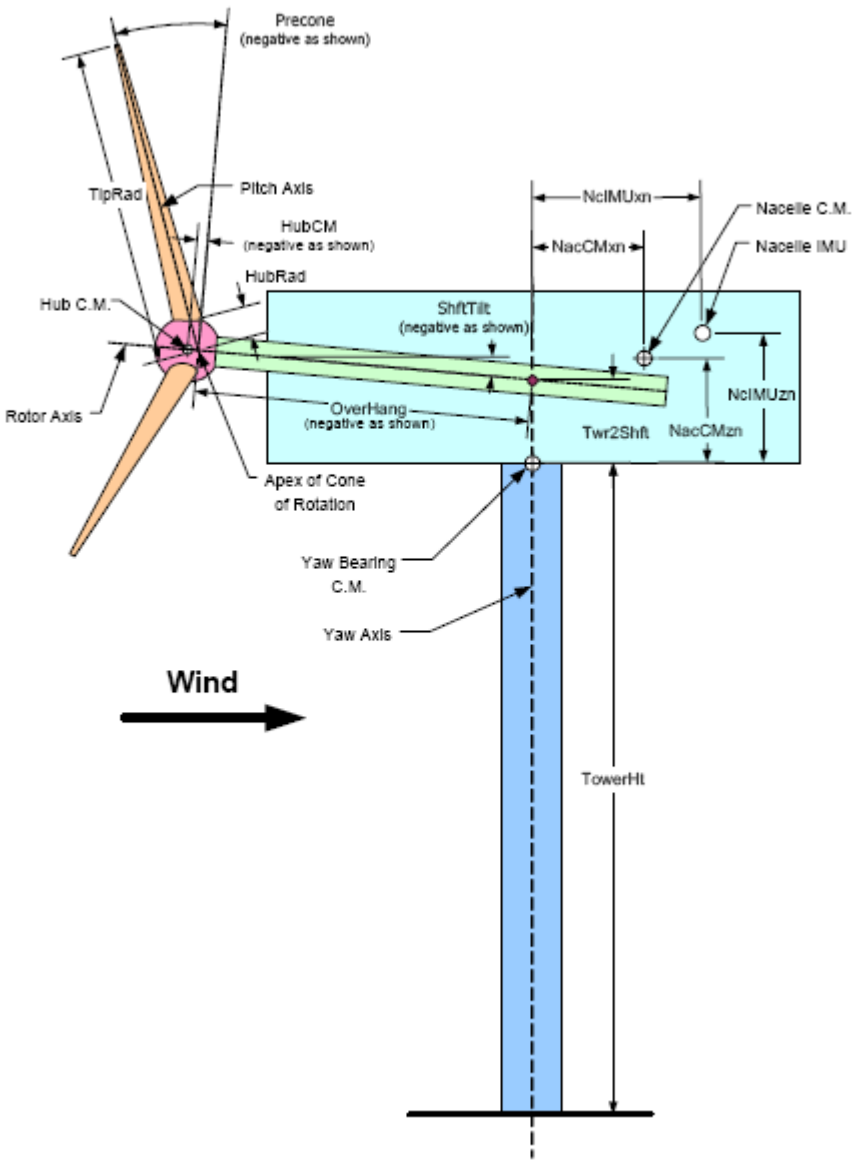

Figure 3.4 - Layout of a conventional, upwind, three-bladed turbine. (example of pre-cone) [21]

3.3.2 - Blade Aerodynamic Properties

Like the blade structural properties, the aerodynamic properties were based on other similar research programs. For our WTPerf and FAST analysis, we used 17 blade

elements and 8 unique air-foil data as tables listed in Table 3.3 – The aerodynamic properties at the blade nodes, are located at the center of the blade elements.

Table 3.2 – Distributed Blade Aerodynamic Properties [20]

Node	RNodes	AeroTwst	DRNodes	Chord	Airfoil Table
(-)	(m)	(º)	(m)	(m)	(-)
1	2.8667	13.308	2.7333	3.542	Cylinder1.dat
2	5.6	13.308	2.7333	3.854	Cylinder1.dat
3	8.3333	13.308	2.7333	4.167	Cylinder2.dat
4	11.75	13.308	4.1	4.557	DU40_A17.dat
5	15.85	11.48	4.1	4.652	DU35_A17.dat
6	19.95	10.162	4.1	4.458	DU35_A17.dat
7	24.05	9.011	4.1	4.249	DU30_A17.dat
8	28.15	7.795	4.1	4.007	DU25_A17.dat
9	32.25	6.544	4.1	3.748	DU25_A17.dat
10	36.35	5.361	4.1	3.502	DU21_A17.dat
11	40.45	4.188	4.1	3.256	DU21_A17.dat
12	44.55	3.125	4.1	3.01	NACA64_A17.dat
13	48.65	2.319	4.1	2.764	NACA64_A17.dat
14	52.75	1.526	4.1	2.518	NACA64_A17.dat
15	56.1667	0.863	2.7333	2.313	NACA64_A17.dat
16	58.9	0.37	2.7333	2.086	NACA64_A17.dat
17	61.6333	0.106	2.7333	1.419	NACA64_A17.dat

The innermost sections of the blades are cylinders. The remaining sections are based on airfoil tables used in other research where, “DU” refers to Delft University and “NACA” refers to the National Advisory Committee for Aeronautics. Previous studies used AirfoilPrep v2.0 to “tailor” these airfoil data. They first corrected the lift and drag coefficients for rotational stall delay using the Selig and Eggars method for 0° to 90° angles of attack. They then corrected the drag coefficients using the Viterna method for 0° to 90° angles of attack assuming an aspect ratio of 17. Finally, they estimated the Beddoes-Leishman dynamic-stall hysteresis parameters. They made no corrections to the DOWEC-supplied pitching-moment coefficients. The blades described here were used in both the WT_Perf and FAST analysis. [18]

3.3.3 - Hub and Nacelle

Table 3.4 presents the properties of the hub and nacelle. The hub is 5 meters upwind of the tower centerline, at an elevation of 90 meters or 2.4 meters to hub from the top of the tower top. The yaw bearing is 87.6 meters above the ground or MSL. The shaft tilt is 5 degrees.

Table 3.3 – Hub and Nacelle properties [20]

Elevation of Yaw Bearing above Ground	87.6m
Vertical Distance along Yaw Axis from Yaw Bearing to Shaft	1.96256m
Distance along Shaft from Hub Center to Yaw Axis	5.01910m
Distance along Shaft from Hub Center to Main Bearing	1.912m
Hub Mass	56,780kg
Hub Inertia about Low-Speed Shaft	115,926kg•m^2
Nacelle Mass	240,000kg
Nacelle Inertia about Yaw Axis	2,607,890kg•m^2
Nacelle CM Location Downwind of Yaw Axis	1.9m
Nacelle CM Location above Yaw Bearing	1.75m
Equivalent Nacelle-Yaw-Actuator Linear-Spring Constant	9,028,320,000N•m/rad
Equivalent Nacelle-Yaw-Actuator Linear-Damping Constant	19,160,000N•m/(rad/s)
Nominal Nacelle-Yaw Rate	0.3º/s

3.3.4 - Drivetrain

The drivetrain used in this study is described in [18,20], and is based on drivetrains in similar studies (DOWEC and RECOFF). The onland wind turbine rotor used in the referenced material runs at 12.1 rpm at a rated generator speed of 1173.7 rpm. In this study, the floating platform wind turbine models run at a rotor speeds of 13 rpm for the 3 bladed model and 16 rpm for the 2 bladed model. These turbine rotational speeds translate into a rated generator speed of 1261 rpm for 13 rpm and 1552 rpm for 16 rpm. Both drivetrain models, 13 rpm and 16 rpm, have a gearbox ratio of 97:1 and an electrical efficiency of 94.4%. Additional structural properties can be found in Table 3.5.

Table 3.4 – Drivetrain properties [20]

Gearbox Ratio	97:1
Electrical Generator Efficiency	94.4%
Generator Inertia about High-Speed Shaft	534.116kg•m_2
Equivalent Drive-Shaft Torsional-Spring Constant	867,637,000N•m/rad
Equivalent Drive-Shaft Torsional-Damping Constant	6,215,000N•m/(rad/s)
Fully-Deployed High-Speed Shaft Brake Torque	28,116.2N•m
High-Speed Shaft Brake Time Constant	0.6s

The higher generator speed used in the 13 and 16 rpm models was found by converting the higher rotor rpm through the gearbox. Additional assessments on system impact of increasing generator speed were not done. The blade geometry was not optimized for the two-blade configuration. Also it is expected that higher Reynold's numbers and lower gear ratios would improve performance of the two-blade system.

The drivetrain used in our analysis uses a conventional variable-speed, variable blade-pitch-to-feather control system. This means the control system uses two controllers to regulate power production. The generator-torque controller, is used in wind speeds below rated generator capacity. The purpose of this controller is to maximize power capture from the wind. Once the generator reaches its rated operational point, the second controller, blade-pitch controller, is used to maintain power at the rated operational point. Typically, wind turbine control is based on the measurement of generator torque (or generator speed). There are five different control regions: 1, 1 ½, 2, 2 ½, and 3 (see Fig. 3.5). Region 1 is the region before the generator starts working. In this region the wind is used to start the rotor spinning. Region 1 ½ , is a transitional region to set a lower limit on when the wind turbine starts operation. Region 2 is a control region used to optimize power capture. The generator speed is altered to match the optimal tip-speed ratio (further description is given in the next sub-section). Region 2 ½ is a linear transition

between Region 2 and 3. It has a torque slope corresponding to the induction machine. Region 2 ½ is typically needed to limit tip speed that can cause noise at rated power. Figure 3.5 shows a good example of the linear progression in region 2 ½. In region 3, the generator power is held constant by pitching the blades.

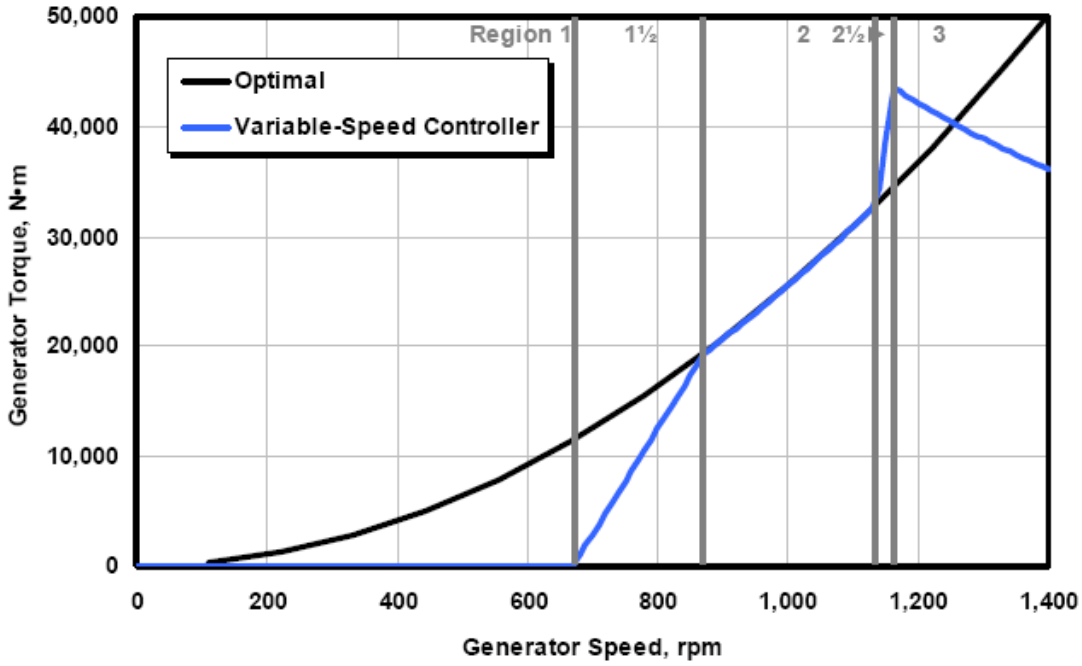

Figure 3.5 - Torque-versus-speed response of the variable-speed controller [18]

3.3.5 - Region 2 – Generator Torque Controller

As mentioned above, generator power can be changed by (1) pitching the blades to change the angle of the flow relative to the rotor, or (2) change the speed at which the rotor spins. In region 2, the latter control option is used; the rotor speed is increased or decreased to maximize power capture from the wind. By operating at this optimal speed we satisfy the goal in region 2; maximizing power capture. In order to determine this operating point we need to define a few variables: tip-speed ratio, coefficient of power, an operating equation, and generator torque constant.

For a given rotor, there is one maximum tip-speed ratio, λ_r. The tip-speed ratio is defined as the speed at the tip of the blade, compared to the wind speed.

$$\lambda_r = \frac{\Omega r}{V} \qquad 3.3$$

The coefficient of power, C_P, is the ratio of the power produced by the rotor, (mechanical power) compared to the power available in the wind. It is helpful to think of the coefficient of power as the percentage of power the wind turbine can extract from the wind.

$$C_P = \frac{T_{Aero}\Omega}{\frac{1}{2}\rho A V^3} = \frac{P_{Mech}}{P_{Wind}} \qquad 3.4$$

It can be shown that the coefficient of power is a function of the tip-speed ratio. Like the tip-speed ratio, there is a single maximum value of the coefficient of power. By operating at the optimum tip-speed ratio, theoretically, the rotor will be operating at maximum efficiency.

Using NREL's WT_Perf performance code, and the blades described in section 3.3.1 and 3.3.2 we found values for the a three-bladed and two-bladed rotor.

Table 3.5 – Maximum Tip-Speed Ratio, Coefficient of Power and Blade Pitch Degree

	3B	2B
tip-speed ratio	7.3	9.5
coefficient of power	0.4685	0.4345
degree	0	-1

In order to control the rotor speed we assume that the generator torque is proportional to the square of the generator speed.

$$T_{Gen} = k\omega^2 \qquad 3.5$$

where k = Generator-Torque Constant in Region 2

Using the tip-speed ratio and coefficient of power, the generator torque constant, k, is defined as:

$$k = \frac{1}{2}\frac{C_P \rho A r^3}{\lambda_r^3} \qquad 3.6$$

Using the values for tip-speed ratio, coefficient of power found in table 3.5 values for the generator torque constant are given in table 3.6.

Table 3.6 – Generator Torque Constant 3 and 2 Blades

	Generator Torque Constant N-m/(rad/s)^2
3 Blades	2.332287
2 Blades	1.136280794

Below the rated capacity of the generator the goal for the control system is to maximize power capture from the wind. For a given fixed rotor geometry there is a sweet spot. An optimal configuration of rotor speed, and blade pitch angle where the most power is taken from the wind. By measuring the generator speed we can increase or decrease the rotor speed to stay in the sweet spot. Once the generator reaches its rated capacity a second method of control is used to maintain operation at rated capacity.

3.3.6 - Region 3 - Blade Pitch Control System

Once the generator reaches its capacity the second control logic takes over. The blades are pitched to change the power produced by the blades. By changing the angle of attack the blades are pitched to match the torque needed to operate at capacity. This is done because at high wind speeds there is more power in the wind than the generator can convert into electricity.

The pitch angle is controlled to maintain generator speed using a gain-scheduled proportional integral (PI) control. In this section we will outline the equations that lead us to finding the gain values needed to control the pitch angle. Then we present the development of two types of controllers: pitch-to-feather and pitch-to-stall. Finally, we address modifications to the controller to include effects of a floating platform.

The purpose of the blade-pitch controller is to maintain the rated operational generator speed. Using the angular rotation of the low-speed shaft, a simple single degree of freedom equation is written.

$$T_{Aero} - N_{Gear}T_{Gen} = \left(I_{Rotor} + N_{Gear}^2 I_{Gen}\right)\frac{d}{dt}\left(\Omega_0 + \Delta\Omega\right) = I_{Drivetrain}\Delta\dot{\Omega} \tag{3.7}$$

where the generator torque is:

$$T_{Gen} = \frac{P_0}{N_{Gear}\Omega} \tag{3.8}$$

and the aerodynamic torque is:

$$T_{Aero}(\theta) = \frac{P(\theta, \Omega_0)}{\Omega_0} \tag{3.9}$$

In the above equations:

N_{Gear} is the gear ratio

Ω_0 is the rated low-speed shaft rotational speed,

$\Delta\dot{\Omega}$ is the low-speed shaft rotational acceleration,

$\Delta\Omega$ is the change in low-speed shaft rotational speed.

P_0 is the rated mechanical power.

θ is the full-span rotor-collective blade-pitch angle.

It is the full-span rotor-collective blade pitch angle that is controlled in order to maintain the proper generator speed. More insight can be found by looking at Taylor series expansion of the generator and aerodynamic torque.

$$T_{Gen} \approx \frac{P_0}{N_{Gear}\Omega_0} - \frac{P_0}{N_{Gear}\Omega_0^2}\Delta\Omega \tag{3.10}$$

$$T_{Aero} \approx \frac{P_0}{\Omega_0} + \frac{1}{\Omega_0}\left(\frac{\partial P}{\partial \theta}\right)\Delta\theta \tag{3.11}$$

where:

$\frac{\partial P}{\partial \theta}$ is the blade pitch sensitivity

$\Delta\theta$ is a small change in the blade-pitch angle

Equation 3.11 shows explicitly how changing the pitch angle can effectively change the torque produced by the rotor. We will use this relationship to maintain the power production at 5 MW. Using the speed error to determine the change in blade pitch angle, a proportional-integral-derivative (PID) control equation is written:

$$\Delta\theta = K_P N_{Gear}\Delta\Omega + K_I \int_0^t N_{Gear}\Delta\Omega dt + K_D N_{Gear}\Delta\dot{\Omega} \qquad 3.12$$

K_P is the proportional gain
K_I is the integral gain
K_D is the derivative gain

By substituting equation 3.12 into 3.11 and then substituting 3.11 and 3.10 into 3.7 rearranging and setting $\dot{\varphi} = \Delta\Omega$, we get the following equation:

$$\left[I_{Drivetrain} + \frac{1}{\Omega_0}\left(-\frac{\partial P}{\partial\theta}\right)N_{Gear}K_D\right]\ddot{\varphi} + \left[\frac{1}{\Omega_0}\left(-\frac{\partial P}{\partial\theta}\right)N_{Gear}K_P - \frac{P_0}{\Omega_0^2}\right]\dot{\varphi} + \left[\frac{1}{\Omega_0}\left(-\frac{\partial P}{\partial\theta}\right)N_{Gear}K_I\right]\varphi = 0 \qquad 3.13$$

Substituting the equations found in the brackets above:

$$M_\varphi = \left[I_{Drivetrain} + \frac{1}{\Omega_0}\left(-\frac{\partial P}{\partial\theta}\right)N_{Gear}K_D\right] \qquad 3.13a$$

$$C_\varphi = \left[\frac{1}{\Omega_0}\left(-\frac{\partial P}{\partial\theta}\right)N_{Gear}K_P - \frac{P_0}{\Omega_0^2}\right] \qquad 3.13b$$

$$K_\varphi = \left[\frac{1}{\Omega_0}\left(-\frac{\partial P}{\partial\theta}\right)N_{Gear}K_I\right] \qquad 3.13c$$

Leads to:

$$M_\varphi\ddot{\varphi} + C_\varphi\dot{\varphi} + K_\varphi\varphi = 0 \qquad 3.14$$

In region 3 of a pitch-to-feather wind turbine the sensitivity of aerodynamic power to rotor-collective blade pitch $\frac{\partial P}{\partial\theta}$, is negative [18]. Using positive control gains, the derivative control gain would increase effective inertia of the drivetrain (see Eq 3.13). The proportional gain adds damping. The integral gain adds restoring. The generator torque drops with increasing speed error (to maintain constant power) in region 3. Therefore the generator-torque controller introduces negative damping in the speed error

equation. The negative damping is found in equation (3.13b) in the $-\frac{P_0}{\Omega_0^2}$ term. The negative damping must be compensated by the proportional gain in the blade-pitch controller. [18, 20, 27]

In [27] it is recommended to neglect the derivative gain ($K_D = 0$), and ignore the negative damping introduced by the generator controller. This leads to following equations for the proportional and integral gains:

$$K_D = 0 \qquad 3.15$$

$$K_P = \frac{2I_{Drivetrain}\Omega_0\zeta_\varphi\omega_n}{N_{Gear}\left(-\frac{\partial P}{\partial \theta}\right)} \qquad 3.16$$

$$K_I = \frac{I_{Drivetrain}\Omega_0\omega_n^2}{N_{Gear}\left(-\frac{\partial P}{\partial \theta}\right)} \qquad 3.17$$

The below values for the natural frequency and damping coefficient are suggested:

$$\omega_n = \sqrt{\frac{K_\varphi}{M_\varphi}} = 0.6 \text{ rad/s} \qquad 3.18$$

$$\zeta_\varphi = \frac{C_\varphi}{2\sqrt{K_\varphi M_\varphi}} = 0.6 \text{ to } 0.7 \qquad 3.19$$

3.3.7- Development of Pitch-to-Feather and Pitch-to-Stall Control Systems

We developed control systems using two approaches to maintaining power production: pitch-to-feather and pitch-to-stall. Presently, pitch-to-feather control systems are the industry norm. In region 3, the pitch-to-feather control system reduces thrust with

increasing wind speed. Onshore this does not present a problem. In a floating offshore environment, however, the decreasing thrust may introduce negative damping. [18] Thrust increases with increasing wind speed with the pitch-to-stall control system. The increase in thrust may have positive damping effects in the floating offshore environment, [18].

In the following section we will outline the steps taken to create the control algorithms used in an external dynamic link library (DLL) to be used with NREL's FAST program. These steps follow the procedure for creating a blade-pitch controller outlined in Ref. [18]. First, we will use the outline to develop a pitch-to-feather control system. Then we will use the outlined steps to create a pitch-to-stall control algorithm.

Steps for creating a controller:

1. Find blade pitch angle that corresponds to producing 5.2966 MW of Rotor Power.
2. Find $\frac{\partial P}{\partial \theta}$ (blade pitch sensitivity) at that angle.
3. Plot pitch sensitivity $\frac{\partial P}{\partial \theta}$, to pitch angle . How does it vary?
4. If variation of $\frac{\partial P}{\partial \theta}$ to blade pitch angle can be represented by an equation, develop a gain correction factor, $GK(\theta)$
5. Find values for $K_P(\theta = 0)$ and $K_I(\theta = 0)$

3.3.8 - Pitch-to-Feather Algorithm

For the development of the pitch-to-feather control system we developed five controller cases:

1. 12.1 rpm three-bladed model
2. 12.1 rpm two-bladed model

3. 13 rpm three-bladed model
4. 13 rpm two-bladed model
5. 16 rpm two-bladed model

Although we do not use the 12.1 controllers in our final analysis of the floating platform wind turbines, we developed them to check our results to those in [18]. In the following tables and graphs "Ref." refers to the three-bladed 12.1 rpm controller developed in Ref. [18].

For step one, we used NREL's performance code WT_Perf to find the blade pitch angles. The higher value of the rotor power compared to the rated power of 5MW is due to the generator efficiently losses.

For step two, we used a special version of FAST developed by NREL to calculate the blade pitch sensitivity, $\frac{\partial P}{\partial \theta}$. Blade pitch sensitivity is an aerodynamic property. The special version of FAST uses a frozen wake assumption to better calculate the pitch sensitivity. For more on the frozen wake assumption please refer to [18]. Using the linearization option, at a number of steady uniform wind speeds, and rotor speeds of 12.1, 13, and 16 rpm we found values for $\frac{\partial P}{\partial \theta}$. Our results are presented in tables 3.7-3.9. computed above are at a constant 12.1 rpm.

For step three, we plotted our results in figures 3.6-3.8. The values for the blade pitch sensitivity in the pitch-to-feather region are negative and decrease with the increase in wind speed.

Table 3.7 – Sensitivity of Aerodynamic Power to Blade Pitch in Region 3, values

Wind Speed	Pitch Angle (deg)	Computed 3B $\frac{\partial P}{\partial \theta}$	Ref. 3B $\frac{\partial P}{\partial \theta}$		2B Pitch Angle (deg)	Computed 2B $\frac{\partial P}{\partial \theta}$
11.4	0	-27.48E+06	-28.24E+06			
12	3.83	-43.73E+06	-43.73E+06		-1.91	-10.92E+06
13	6.6	-51.64E+06	-51.66E+06		3.36	-26.81E+06
14	8.7	-58.42E+06	-58.44E+06		5.95	-32.41E+06
15	10.45	-64.49E+06	-64.44E+06		8.04	-38.04E+06
16	12.06	-70.49E+06	-70.46E+06		9.88	-41.74E+06
17	13.54	-76.47E+06	-76.53E+06		11.56	-45.51E+06
18	14.92	-83.95E+06	-83.94E+06		13.11	-49.26E+06
19	16.23	-90.65E+06	-90.67E+06		14.57	-53.12E+06
20	17.47	-94.70E+06	-94.71E+06		15.95	-57.11E+06
21	18.7	-98.91E+06	-99.04E+06		17.26	-61.76E+06
22	19.94	-01.06E+08	-01.06E+08		18.51	-65.96E+06
23	21.18	-01.14E+08	-01.14E+08		19.72	-68.78E+06
24	22.35	-01.20E+08	-01.20E+08		20.9	-72.06E+06
25	23.47	-01.25E+08	-01.25E+08		22.03	-75.62E+06

For step four, we performed a best-fit using linear regression. The linear equations can be related to equation 3.20.

$$\frac{\partial P}{\partial \theta} = \left[\frac{\left(\frac{\partial P}{\partial \theta} \middle| \theta = 0 \right)}{\theta_K} \right] \theta + \left[\left(\frac{\partial P}{\partial \theta} \middle| \theta = 0 \right) \right] \qquad 3.20$$

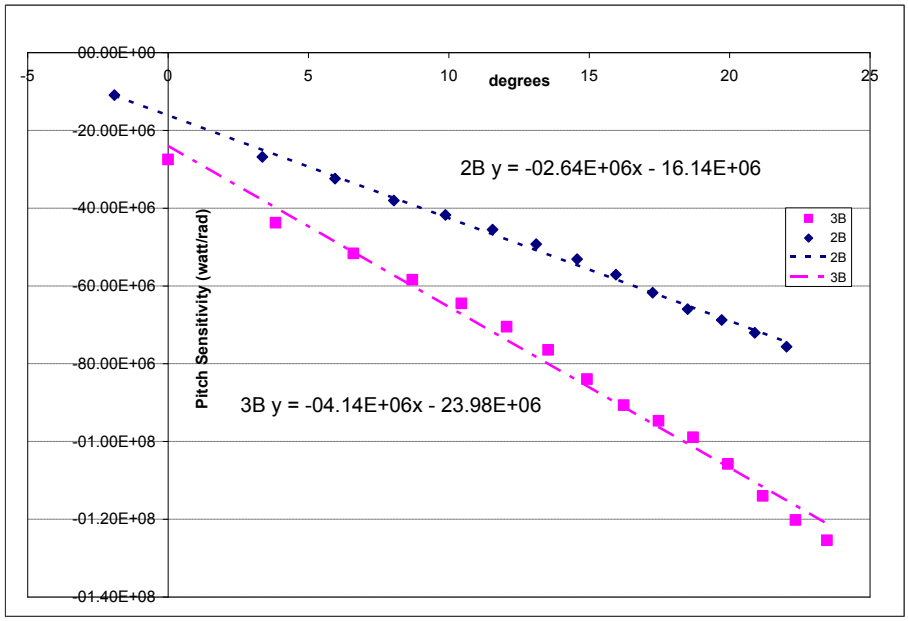

Figure 3.6 – Best fit line of pitch sensitivity in Region 3, 12.1 rpm

In equation 3.20, $\frac{\partial P}{\partial \theta}\left(\theta = 0\right)$ is equal to the pitch sensitivity when rotor reaches rated power production. θ_K is the angle at which $\frac{\partial P}{\partial \theta}$ reaches twice the value of $\frac{\partial P}{\partial \theta}\left(\theta = 0\right)$ equation 3.21. θ_K does not have a physical meaning and simply used as a mathematical tool.

$$\frac{\partial P}{\partial \theta}\left(\theta = \theta_K\right) = 2\frac{\partial P}{\partial \theta}\left(\theta = 0\right) \qquad 3.21$$

The wide variation in values for $\frac{\partial P}{\partial \theta}$ throughout region 3, does not lend itself to single value gains. However, the approximate linear progression of its values does lead itself to using a dimensionless gain correction factor, $GK(\theta)$

$$GK(\theta) = \frac{1}{1+\frac{\theta}{\theta_K}} \qquad 3.22$$

Table 3.8 – Sensitivity of Aerodynamic Power to Blade Pitch in Region 3, values computed above are at a constant rotor speed of 13 rpm.

Wind Speed	Pitch Angle (deg)	2B $\frac{\partial P}{\partial \theta}$		pitch angle (deg)	3B $\frac{\partial P}{\partial \theta}$
12	0.54	-20880000		4.22	-5.2E+07
13	3.89	-35250000		6.62	-6E+07
14	6.13	-41640000		8.49	-6.8E+07
15	8.01	-46200000		10.11	-7.5E+07
16	9.69	-50610000		11.59	-8.2E+07
17	11.22	-54720000		12.96	-9E+07
18	12.65	-58790000		14.24	-9.9E+07
19	13.99	-62860000		15.45	-1.1E+08
20	15.27	-67810000		16.62	-1.1E+08
21	16.49	-73360000		17.75	-1.1E+08
22	17.66	-77090000		17.75	-1.2E+08
23	18.79	-80020000		19.93	-1.3E+08
24	19.89	-83370000		20.96	-1.4E+08
25	20.96	-88990000		21.96	-1.5E+08

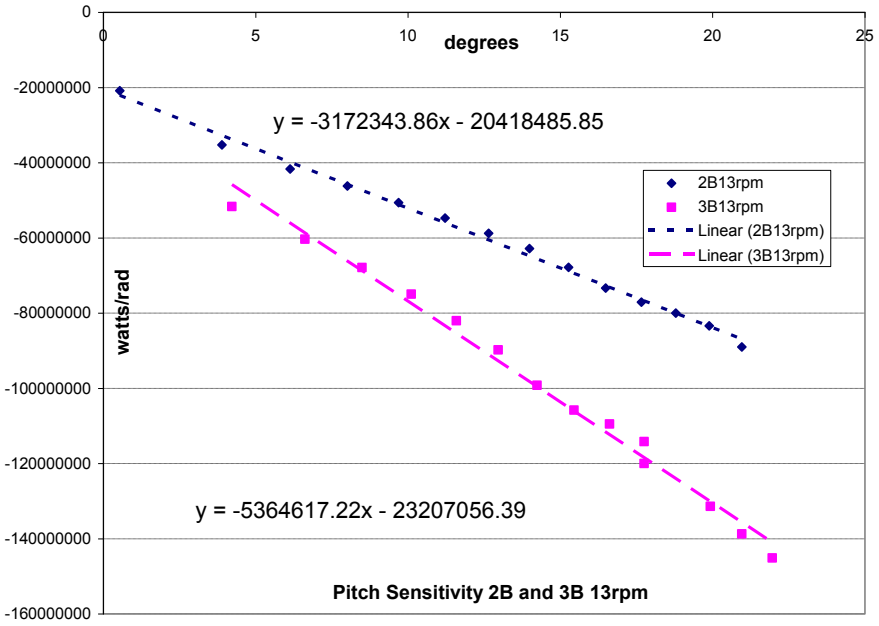

Figure 3.7 - Best fit line of pitch sensitivity in Region 3, 13 rpm

Table 3.9 – Sensitivity of Aerodynamic Power to Blade Pitch in Region 3, values computed above are at a constant rotor speed of 16 rpm.

Wind Speed	Pitch Angle (deg.)	2B $\frac{\partial P}{\partial \theta}$
12	2.04	-48910000
13	4.32	-57470000
14	6.01	-65060000
15	7.46	-71980000
16	8.77	-78400000
17	9.97	-85140000
18	11.1	-91590000
19	12.18	-100300000
20	13.2	-109300000
21	14.17	-115800000
22	15.12	-119900000
23	16.06	-122600000
24	16.97	-127800000
25	17.87	-136100000

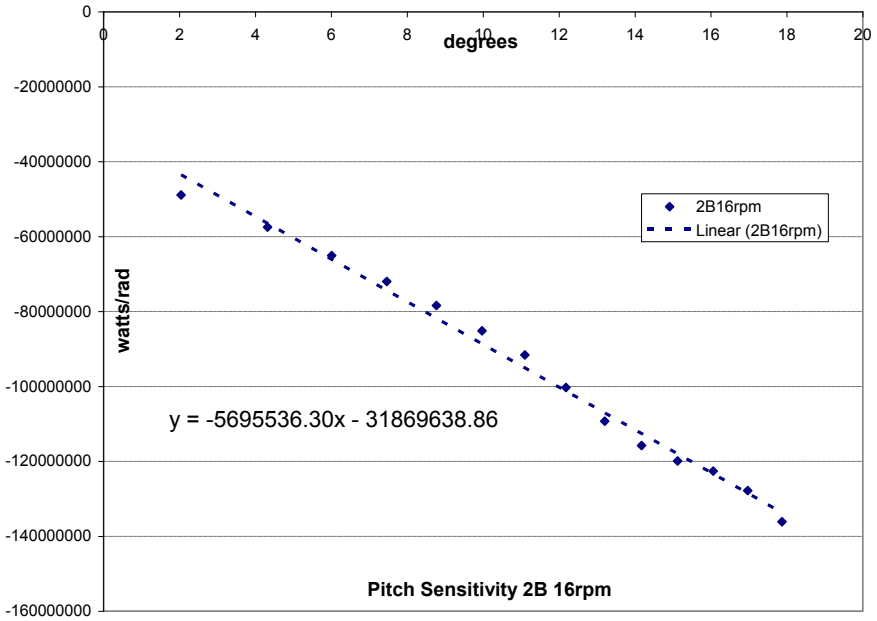

Figure 3.8 - Best fit line of pitch sensitivity in Region 3, 2 blades, 16 rpm

For step five, the gain correction factor and equations developed for the proportional and integral gains (eq. 3.16 and 17) are used to develop a gain schedule based on the blade pitch angle from the previous time step (eq. 3.23 and 3.24).

$$K_P(\theta) = \frac{2I_{Drivetrain}\Omega_0\zeta_\varphi\omega_n}{N_{Gear}\left[-\frac{\partial P}{\partial\theta}(\theta = 0)\right]} GK(\theta) \qquad 3.23$$

$$K_I(\theta) = \frac{I_{Drivetrain}\Omega_0\omega_n^2}{N_{Gear}\left[-\frac{\partial P}{\partial\theta}(\theta = 0)\right]} GK(\theta) \qquad 3.24$$

Figures 3.9 through 3.11 show performance outputs of the pitch-to-feather control system we have outline here. The figures show the controllers working as expected as the steady wind is increased from 13 to 17 mps.

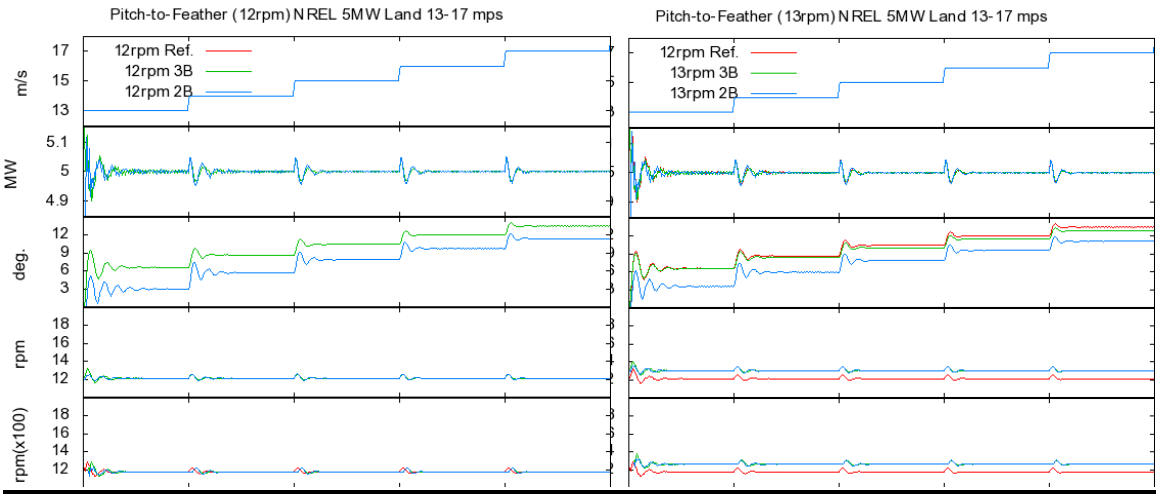

Figure 3.9 and 3.10 – Performance Parameters from top: Wind Speed, Generator Power, Blade Pitch, Rotor Speed, Generator Speed (values are multiplied by 100)

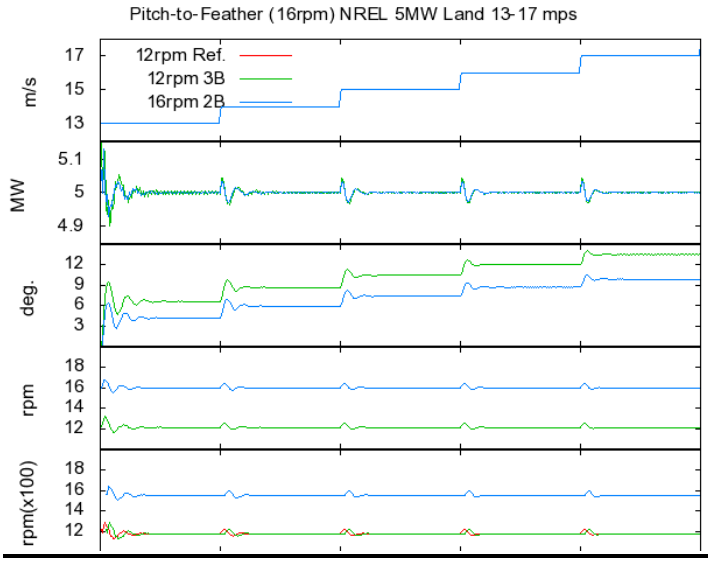

Figure 3.11 - Performance Parameters from top: Wind Speed, Generator Power, Blade Pitch, Rotor Speed, Generator Speed (values are multiplied by 100)

3.3.9 - Pitch-to-Stall Algorithm

We developed two Pitch-to-Stall controllers:

1. 13 rpm three-bladed model
2. 16 rpm two-bladed model

For steps 1 and 2 we used the same procedure and tools to find pitch angles and blade pitch sensitivity as we did for the pitch-to-feather controllers. Unlike the pitch-to-feather controller the blade pitch angles for the pitch-to-stall controller are negative and double-valued. The pitch angles decrease then increase as the wind speed increases.

Table 3.10 – Pitch-to-Stall values for Pitch Sensitivit

wind speed (m/s)	rpm	pitch angle	2B $\frac{\partial P}{\partial \theta}$		rpm	pitch angle	3B $\frac{\partial P}{\partial \theta}$
12	16	-6.84	-12550000		13	-6.7	-13850000
13	16	-8.81	66540000		13	-8.02	-710300
14	16	-8.96	70480000		13	-8.27	23520000
15	16	-9.1	71750000		13	-8.54	84360000
16	16	-9.28	68540000		13	-8.83	105500000
17	16	-9.5	69370000		13	-9.04	109000000
18	16	-9.68	71280000		13	-9.15	103700000
19	16	-9.85	74420000		13	-9.08	108400000
20	16	-9.93	82530000		13	-8.9	114800000
21	16	-9.9	96780000		13	-8.67	113700000
22	16	-9.77	104400000		13	-8.41	117300000
23	16	-9.61	109000000		13	-8.13	126000000
24	16	-9.42	114700000		13	-7.84	138400000
25	16	-9.22	121000000		13	-7.54	153200000

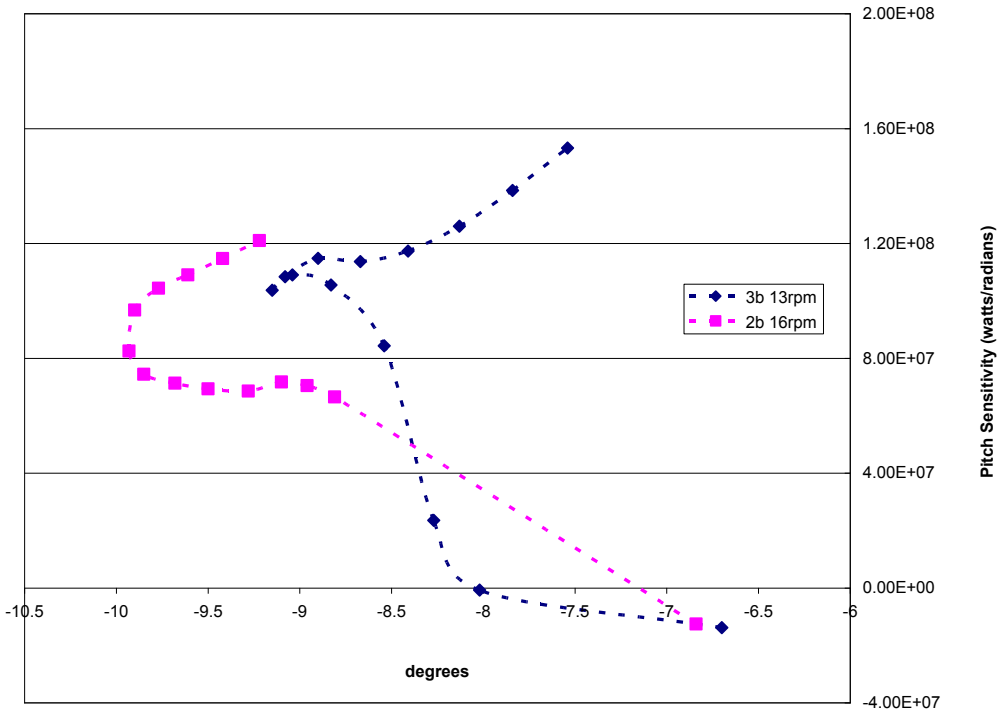

Figure 3.12 – Pitch Sensitivity with regard to Blade Pitch Angle

Because the blade pitch angles do not follow a linear progression we can not use the linear approximation we did for the pitch-to-feather controllers. However, there is

approximately a 3 degree difference between the minimum and maximum blade pitch angles for the two and three-bladed models. With such small variation in blade pitch angles we chose to use a constant values for our control gains. Using the minimum pitch angle to determine the pitch sensitivity

$$K_P(\theta) = \frac{2 I_{Drivetrain} \Omega_0 \zeta_\varphi \omega_n}{N_{Gear}\left[-\frac{\partial P}{\partial \theta}(\theta = \theta_{\min})\right]} \qquad 3.25$$

$$K_I(\theta) = \frac{I_{Drivetrain} \Omega_0 \omega_n^2}{N_{Gear}\left[-\frac{\partial P}{\partial \theta}(\theta = \theta_{\min})\right]} \qquad 3.26$$

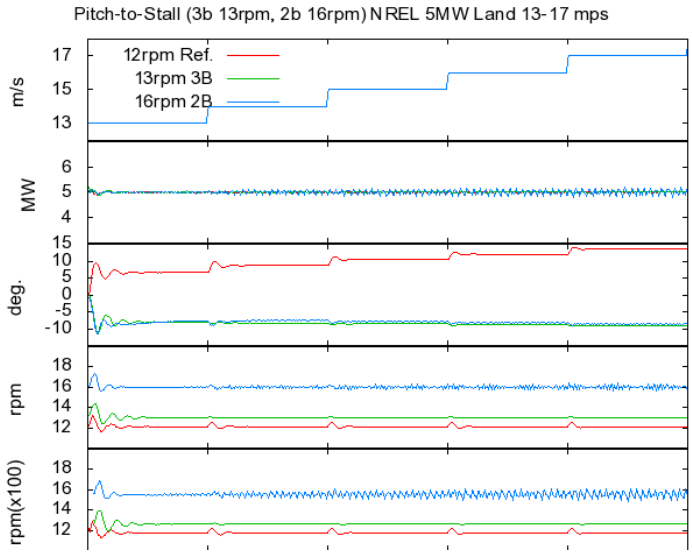

Figure 3.13 – Performance Parameters from top: Wind Speed, Generator Power, Blade Pitch, Rotor Speed, Generator Speed (values are multiplied by 100)

3.3.10 - Floating Platform affects on Control System

Floating platform wind turbines are subjected to different dynamics and lower natural frequencies than onshore wind turbines. The lower natural frequencies of the floating platform wind turbine can lead to an unfavorable coupling between the drivetrain controller and the floating platform wind turbine. It is important that the natural frequency of the drivetrain controller be lower than the lowest natural frequency of the floating platform wind turbine. [27]

Table 3.11 – Barge Drivetrain controller natural frequency and control gain values

Barge Pitch-to-Feather				Barge Pitch-to-Stall		
NF	0.4	rad/s		NF	0.4	rad/s
2B Kp 16 rpm	0.009379878	sec		2B Kp 16 rpm	-0.003622117	sec
2B Ki 16 rpm	0.002679965			2B Ki 16 rpm	-0.001034891	
3B Kp 13 rpm	0.014828282	sec		3B Kp 13 rpm	-0.003318426	sec
3B Ki 13 rpm	0.004236652			3B Ki 13 rpm	-0.000948122	

Table 3.12 – Spar Drivetrain controller natural frequency and control gain values

Spar Controller Pitch-to-Feather				Spar Controller Pitch-to-Stall		
NF	0.2	rad/s		NF	0.2	rad/s
2B Kp 16 rpm	0.004689939	sec		2B Kp 16 rpm	-0.001811059	sec
2B Ki 16 rpm	0.000669991			2B Ki 16 rpm	-0.000258723	
3B Kp 13 rpm	0.007414141	sec		3B Kp 13 rpm	-0.001659213	sec
3B Ki 13 rpm	0.001059163			3B Ki 13 rpm	-0.00023703	

Table 3.13 – TLP Drivetrain controller natural frequency and control gain values

TLP Controller Pitch-to-Feather				TLP Controller Pitch-to-Stall		
NF	0.6	rad/s		NF	0.6	rad/s
2B Kp 16 rpm	0.014069817	sec		2B Kp 16 rpm	-0.005433176	sec
2B Ki 16 rpm	0.006029921			2B Ki 16 rpm	-0.002328504	
3B Kp 13 rpm	0.022242423	sec		3B Kp 13 rpm	-0.004977639	sec
3B Ki 13 rpm	0.009532467			3B Ki 13 rpm	-0.002133274	

3.3.11 – ITI Barge and MIT/NREL TLP Tower

For both the ITI Barge and MIT/NREL TLP the tower starts at the platform base and ends at the yaw bearing 87.6 meters above the SWL. It has a base diameter of 6.0 meters with a 0.027 meter thickness. The tower tapers to a diameter of 3.87 meters, at the top, with a thickness of 0.019 meters. The tower is made of steel with a Young's modulus of 210 GPa and sheer modulus of 80.8 GPa, and a density of 8,500 kg/m^3 (which is higher than the typical steel, to account for paint, bolts, welds and flanges). The overall integrated tower mass is 347,460 kg. The center of mass is located on the center-line at 38.234 meters.

Table 3.14 – Distributive Tower Properties [18, 31] Barge, TLP

(m)	(-)	(kg/m)	(Nm^2)	(Nm^2)	(Nm^2)	(N)	(kg m)	(kg m)	(m)	(m)
0.00	0	5590.87	614.3E+9	614.3E+9	472.8E+9	138.1E+9	24866.3	24866.3	0.0	0.0
8.76	0.1	5232.43	534.8E+9	534.8E+9	411.6E+9	129.3E+9	21647.5	21647.5	0.0	0.0
17.52	0.2	4885.76	463.3E+9	463.3E+9	356.5E+9	120.7E+9	18751.3	18751.3	0.0	0.0
26.28	0.3	4550.87	399.1E+9	399.1E+9	307.1E+9	112.4E+9	16155.3	16155.3	0.0	0.0
35.04	0.4	4227.75	341.9E+9	341.9E+9	263.1E+9	104.5E+9	13838.1	13838.1	0.0	0.0
43.80	0.5	3916.41	291.0E+9	291.0E+9	223.9E+9	96.8E+9	11779	11779	0.0	0.0
52.56	0.6	3616.83	246.0E+9	246.0E+9	189.3E+9	89.4E+9	9958.2	9958.2	0.0	0.0
61.32	0.7	3329.03	206.5E+9	206.5E+9	158.9E+9	82.2E+9	8356.6	8356.6	0.0	0.0
70.08	0.8	3053.01	171.9E+9	171.9E+9	132.2E+9	75.4E+9	6955.9	6955.9	0.0	0.0
78.84	0.9	2788.75	141.8E+9	141.8E+9	109.1E+9	68.9E+9	5738.6	5738.6	0.0	0.0
87.60	1	2536.27	115.8E+9	115.8E+9	89.1E+9	62.7E+9	4688	4688	0.0	0.0

Table 3.15 – Undistributive Tower Properties [18, 31] Barge, TLP

Hieght above Ground	87.6 m
Overall (Integrated) Mass	347,460 kg
CM Location (w.r.t. Ground along Tower Centerline)	38.234 m
Structural-Damping Ratio (All Modes)	1%

3.3.12 – OC3/Hywind Tower

The tower starts at the platform base 10 meters above the Still Water Line (SWL) and ends at the yaw bearing 87.6 meters above the SWL. It has a base diameter of 6.5 meters with a 0.027 meter thickness. The tower tapers to a diameter of 3.87 meters, at the top, with a thickness of 0.019 meters. The tower is made of steel with a Young's modulus of 210 GPa and sheer modulus of 80.8 GPa, and a density of 8,500 kg/m^3 (which is higher than the typical steel, to account for paint, bolts, welds and flanges). The overall integrated tower mass is 249,718 kg. The center of mass is located on the center-line at 43.4 meters.

Table 3.16 – Distributive Tower Properties [13] buoy

Elevation	HtFract	TMassDen	TwFAStif	TwSSStif	TwGJStif	TwEAStif	TwFAIner	TwSSIner	TwFAcgOf	TwSScgOf
(m)	(-)	(kg/m)	(N•m2)	(N•m2)	(N•m2)	(N)	(kg•m)	(kg•m)	(m)	(m)
10.00	0.00000	4667.00	603.903E+9	603.903E+9	464.718E+9	115.302E+9	24443.7	24443.7	0.0	0.0
17.76	0.10000	4345.28	517.644E+9	517.644E+9	398.339E+9	107.354E+9	20952.2	20952.2	0.0	0.0
25.52	0.20000	4034.76	440.925E+9	440.925E+9	339.303E+9	99.682E+9	17847.0	17847.0	0.0	0.0
33.28	0.30000	3735.44	373.022E+9	373.022E+9	287.049E+9	92.287E+9	15098.5	15098.5	0.0	0.0
41.04	0.40000	3447.32	313.236E+9	313.236E+9	241.043E+9	85.169E+9	12678.6	12678.6	0.0	0.0
48.80	0.50000	3170.40	260.897E+9	260.897E+9	200.767E+9	78.328E+9	10560.1	10560.1	0.0	0.0
56.56	0.60000	2904.69	215.365E+9	215.365E+9	165.729E+9	71.763E+9	8717.2	8717.2	0.0	0.0
64.32	0.70000	2650.18	176.028E+9	176.028E+9	135.458E+9	65.475E+9	7124.9	7124.9	0.0	0.0
72.08	0.80000	2406.88	142.301E+9	142.301E+9	109.504E+9	59.464E+9	5759.8	5759.8	0.0	0.0
79.84	0.90000	2174.77	113.630E+9	113.630E+9	87.441E+9	53.730E+9	4599.3	4599.3	0.0	0.0
87.60	1.00000	1953.87	89.488E+9	89.488E+9	68.863E+9	48.272E+9	3622.1	3622.1	0.0	0.0

Table 3.17 – Undistributive Tower Properties [13] buoy

Elevation to Tower Base (Platform Top) Above SWL	10 m
Elevation to Tower Top (Yaw Bearing) Above SWL	87.6 m
Overall (Integrated) Tower Mass	249,718 kg
CM Location of Tower Above SWL Along Tower Centerline	43.4 m
Tower Structural-Damping Ratio (All Modes)	1%

3.3.13 - Platform OC3/Hywind Spar Buoy

Figures 3.14 shows the platform buoy. This platform starts at the tower base 10 meters above the SWL and has a draft of 120 meters. There is a tapered region that starts at 4 meters above the SWL and ends at 12 meters below the SWL that connects the top diameter of 6.5 meters to the base diameter of 9.4 meters.

The center of mass is located, on the centerline, 89.9155 meters below the SWL. The mass of the platform is 7,466,330 kg. The combined weight of the rotor-nacelle, tower, platform and mooring system balances with the buoyancy of the displaced fluid.

The spar buoy is held in position by 3 catenary lines. This first catenary line is located on the x-z axis. The following 2 catenary lines are located at 120 degrees on either side. The catenary lines are located 70 meters below the SWL.

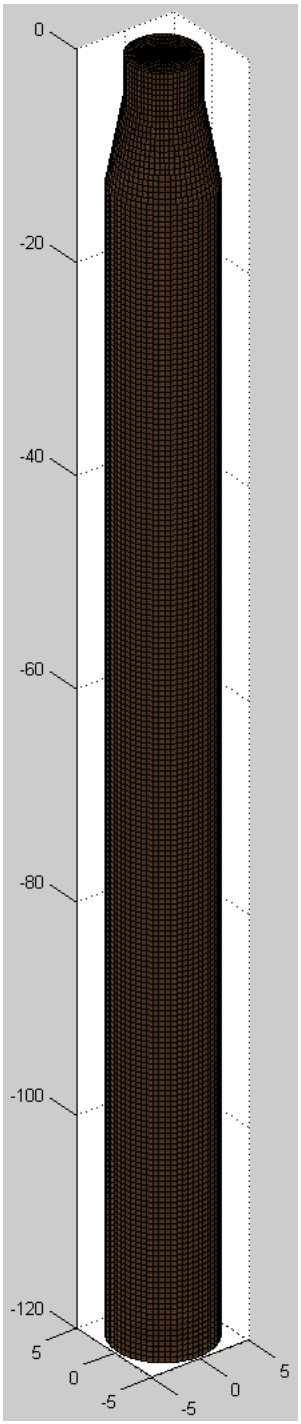

Figure 3.14 – OC3 Spar Buoy Platform [13]

3.3.14 - Platform ITI Energy Barge

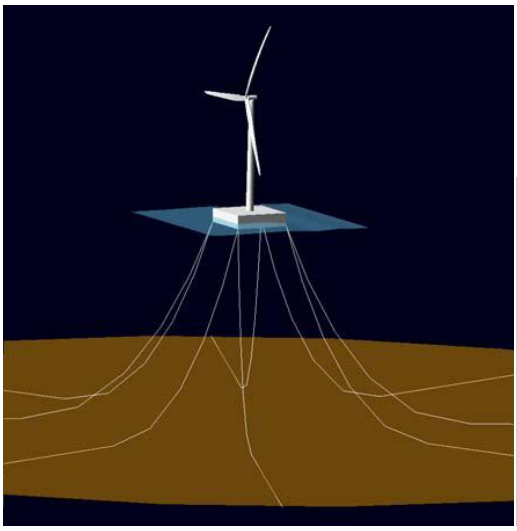

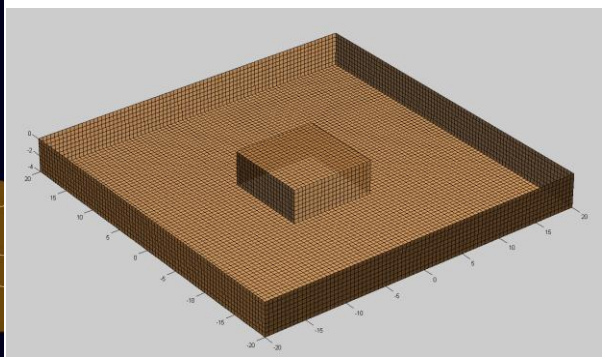

Figures 3.15 and 3.16 - Illustration of the 5-MW wind turbine on the ITI Energy barge and Panel mesh of the ITI Energy barge used within WAMIT [18]

The floating barge platform used in our analysis is the barge developed at the Universities of Glasgow and Strathclyde through a contract with ITI Energy.[32] The barge was designed to support a 5MW wind turbine, but is also an OWC (Oscillating Water Column) wave power device. The barge is a 40 mx 40m x 10m (W x L x H) square. It is ballasted with seawater to achieve reasonable draft. It is moored with a system of 8 catenary lines. Two of these lines emanate from each corner of the bottom of the barge such that they would be 45 degrees apart at the corner.

The barge has a mass of 5,452,000 kg (including ballast sea water). The Center of Mass (CM) is located 0.281768 m below the SWL

More information can be found in [18, 32].

3.3.15 - Platform NREL/MIT Tension Leg Platform

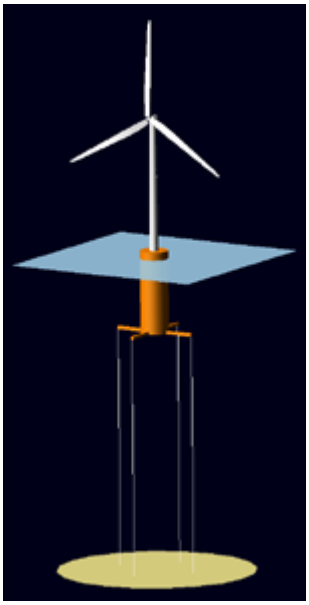

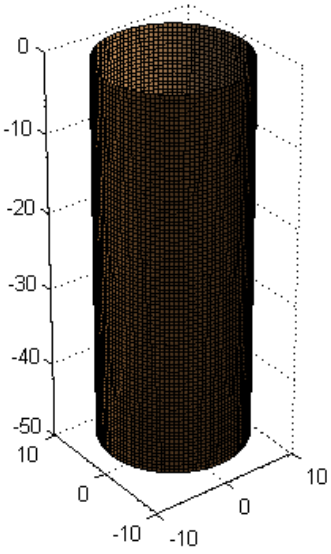

Figure 3.17 and 3.18 – Conceptual Tension Leg Platform [31]

The tension leg platform used in our analysis is named the MIT/NREL TLP. It was developed at the Massachusetts Institute of Technology (MIT) and refined at NREL. The model is described in the [31]. The MIT/NREL TLP is a cylindrical platform, ballasted with concrete, and moored by four pairs of vertical tendons in tension. The platform has a diameter of 18m and a draft of 47.89 m below the SWL. The total mass including the ballast is 8,600,000 kg with a center of mass located at 40.61 m below the SWL. The mooring system is connected to the bottom of the platform (47.89 m below the SWL) with the use of fairlead "arms". The fairlead arms are 27m in radius from the center of the platform. The unstreched length of the mooring lines is 151.7 m.

The concrete ballast of this design is different from most tension leg platform designs. The concrete ballast is used to achieve favorable conditions to tow the platform out to sea.

Chapter Four

Results

4.1 - Annual Energy

In simple terms the motion of wind turbine blades is produced by the balance between the mechanical torque generated by the aerodynamics and the electrical torque provided by the generator. The equation of motion can be written to describe this relationship.

$$I_{Rotor}\dot{\Omega} = T_{Aero} - T_{Gen} \qquad 4.1$$

I_{Rotor} - rotor inertia kg-m^2
$\dot{\Omega}$ - angular rotor acceleration
T_{Aero} -aerodynamic torque N-m
T_{Gen} - generator torque N-m

The torque produced by the aerodynamic forces on the rotor can be controlled two ways: changing the blade geometry by changing the pitch angle or changing the rotor's rotational speed. Most wind turbines use both concepts to control power production. Below the rated capacity of the generator, the speed is controlled so as to maximize the wind power captured. Once the wind turbine reaches its rated capacity the rotor blades

are pitched to alter the power produced by the rotor to match the generator's capacity. We used this control strategy concept and calculated the annual energy.

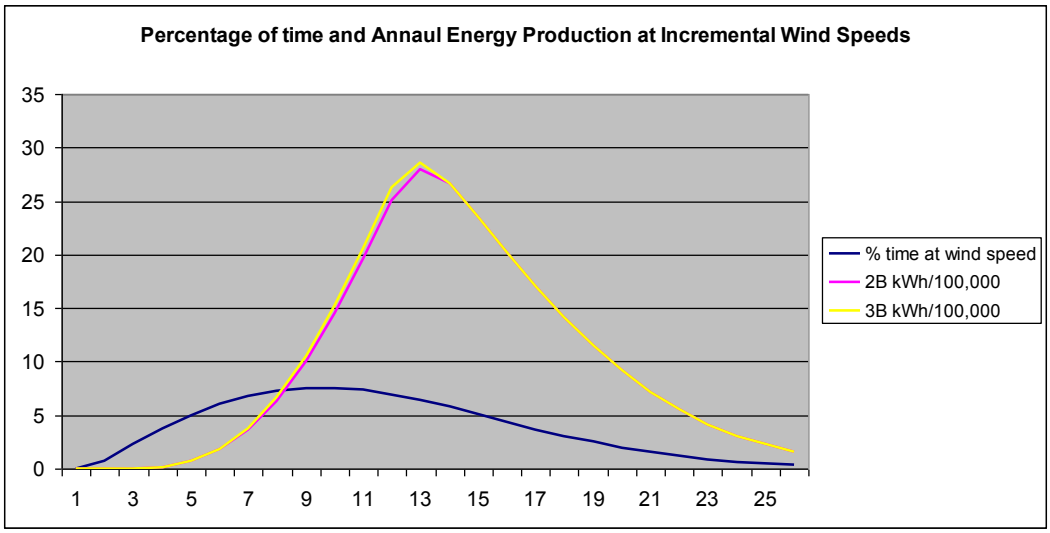

Figure 4.1 – The percentage of time at each wind speed (multiplied by 100 for graph) and the annual energy produced at each wind speed (values have been divided by 100,000 for graph)

Our first step in calculating the annual energy was to find the maximum power coefficient. The power coefficient is the ratio of the mechanical power produced by the rotor to the power available in the wind, for a given geometry. It is the maximum amount of energy the rotor can extract from the wind. For the purpose of this analysis, the coefficient of power is considered to be only a function of tip-speed ratio.

$$C_P = \frac{T_{Aero}\Omega}{\frac{1}{2}\rho A V^3} = \frac{P_{Mech}}{P_{Wind}} \qquad 4.2$$

where:

T_{Aero} is the aerodynamic torque, Ω is the rotor rotational speed, ρ is the air density, V is the wind speed, P_{Mech} is the mechanical power, and P_{Wind} is the power available in the wind.

The aerodynamic performance of a rotor is based on the blade pitch (angle of attack), taper (solidity), and twist distribution. For a given fixed rotor configuration there is one maximum coefficient of power and one corresponding tip-speed ratio. For the blades used in our analysis the maximum power coefficient and tip-speed ratio were 0.4685 and 7.3 at a blade pitch angle of 0 degrees for the three-bladed model and 0.4345 and 9.5 at a blade pitch angle of -1 degrees for two-bladed tested model.

The second step is using the tip-speed ratio, rotor radius, and wind speed to find the rotor speed (equation 4.3)

$$\Omega = \frac{\lambda_r V}{r} \qquad 4.3$$

The results can be found in Table 4.1.

In the third step we calculated the power. Once we knew the rotor rpm needed to obtain maximum power capture (or to maintain the tip-speed ratio) from the wind, we calculated the power produced at that wind speed. The maximum power the generator can produce is 5MW. The drivetrain is 94.4% efficient, losing 5.6% of the energy from the rotor in the transformation into electricity. This translates into a maximum value of 5296 kW of power produced by the rotor at the name-plate capacity. Once the rotor power reaches this value the blades are pitched to maintain this power. Maximum power is reached at a wind speed of 11.3 mps and a rotor speed of 13 rpm for the three-bladed model and at 11.5 mps and 16 rpm for the two-bladed model.

Table 4.1 – Rotor rpm needed to maintain tip-speed ratio

Wind Speed	rpm	
	2B	3B
0.00	0.00	0.00
1.00	1.45	1.14
2.00	2.90	2.29
3.00	4.34	3.43
4.00	5.79	4.58
5.00	7.24	5.72
6.00	8.69	6.87
7.00	10.13	8.01
8.00	11.58	9.16
9.00	13.03	10.30
10.00	14.48	11.44
11.00	15.92	12.59
11.20	16.21	12.82
11.30	16.36	12.93
11.40	16.50	13.05
11.50	16.65	13.16
12.00	17.37	13.73
13.00	18.82	14.88
14.00	20.27	16.02
15.00	21.71	17.17
16.00	23.16	18.31
17.00	24.61	19.45
18.00	26.06	20.60
19.00	27.50	21.74
20.00	28.95	22.89
21.00	30.40	24.03
22.00	31.85	25.18
23.00	33.29	26.32
24.00	34.74	27.47
25.00	36.19	28.61

At this point we shift our attention to the wind distribution. We used the cumulative wind distribution to determine how often the wind would blow at a particular speed over a course of a year. By differentiating the cumulative distribution, one obtains the density function of the wind speed. Because we used a cumulative distribution, we then averaged the power production between the current wind speed and the previous wind speed. Then

we put it all together. We multiplied the average power output, the difference in the cumulative wind distribution, 8760 hours (hours in a year) to get the annual energy production at a particular speed. We then summed our results over the entire wind range. Figure 4.2 compares the energy produced two and three-bladed rotors.

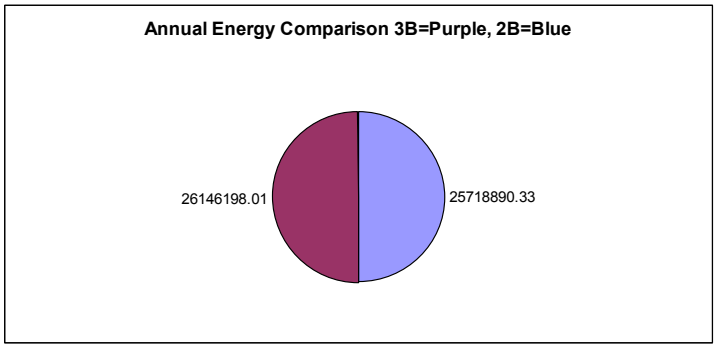

Figure 4.2 – Using a Circle Graph to Compare the Annual Energy of a 2 and 3 Bladed Wind Turbine Rotor (note: for black and white printers 3B is on the left of the circle graph)

The first difference between the two rotor models is the rotor rpm at which the wind turbine reaches capacity. The three-bladed model reaches capacity at 11.3 mps and a rotor rpm of 12.93 rpm. The two-bladed model reaches capacity at 11.5 mps and a rotor rpm of 16.65. This was to be expected. Our analysis is shows that there is about a 1.6 percent difference between the two and three-bladed model. This is without any blade optimization for the two-bladed model. Increasing the chord length, and changing the geometry of the two-bladed model would increase its coefficient of power and ultimately increase the amount of energy it produces.

Table 4.2 – Power Production over the operating range of wind turbine (kw), and Annual Energy Produced at each Wind Speed (kWh)

			2B		3B	
WS	cumulative	% at WS	kw	kwh	kw	kwh
0	0		0		0	
1	0.0078	0.0078	0		0	
2	0.0309	0.0231	0		0	
3	0.0682	0.0373	95.58	15623.42	100.15	16369.25
4	0.1181	0.0498	226.56	70328.50	237.39	73689.65
5	0.1783	0.0602	442.49	176373.95	463.65	184806.52
6	0.2463	0.0680	764.62	359588.34	801.17	376779.66
7	0.3194	0.0732	1214.25	634083.88	1272.26	664387.11
8	0.3951	0.0756	1812.49	1002680.93	1899.15	1050607.43
9	0.4707	0.0756	2580.65	1454845.88	2704.03	1524402.76
10	0.5441	0.0734	3539.95	1967088.50	3709.19	2061134.16
11	0.6134	0.0693	4711.81	2505607.57	4937.00	2625372.84
11.2	0.6266	0.0132	4973.51	562065.57	5211.11	588922.24
11.3	0.6332	0.0065	5107.83	288778.36	5352.01	302579.04
11.4	0.6397	0.0065	5244.73	293919.64	5296.00	302307.99
11.5	0.6461	0.0064	5384.05	299017.81	5296.00	297983.28
12	0.6773	0.0312	5296.00	1459462.40	5296.00	1447430.50
13	0.7348	0.0575	5296.00	2669114.12	5296.00	2669114.12
14	0.7855	0.0507	5296.00	2350836.59	5296.00	2350836.59
15	0.8292	0.0437	5296.00	2027100.35	5296.00	2027100.35
16	0.8661	0.0369	5296.00	1712555.05	5296.00	1712555.05
17	0.8967	0.0306	5296.00	1418369.57	5296.00	1418369.57
18	0.9215	0.0248	5296.00	1152187.47	5296.00	1152187.47
19	0.9413	0.0198	5296.00	918382.24	5296.00	918382.24
20	0.9568	0.0155	5296.00	718521.92	5296.00	718521.92
21	0.9687	0.0119	5296.00	551950.26	5296.00	551950.26
22	0.9777	0.0090	5296.00	416401.43	5296.00	416401.43
23	0.9843	0.0067	5296.00	308582.24	5296.00	308582.24
24	0.9892	0.0048	5296.00	224676.65	5296.00	224676.65
25	0.9926	0.0035	5296.00	160747.71	5296.00	160747.71
			annual energy	25718890	annual energy	26146198

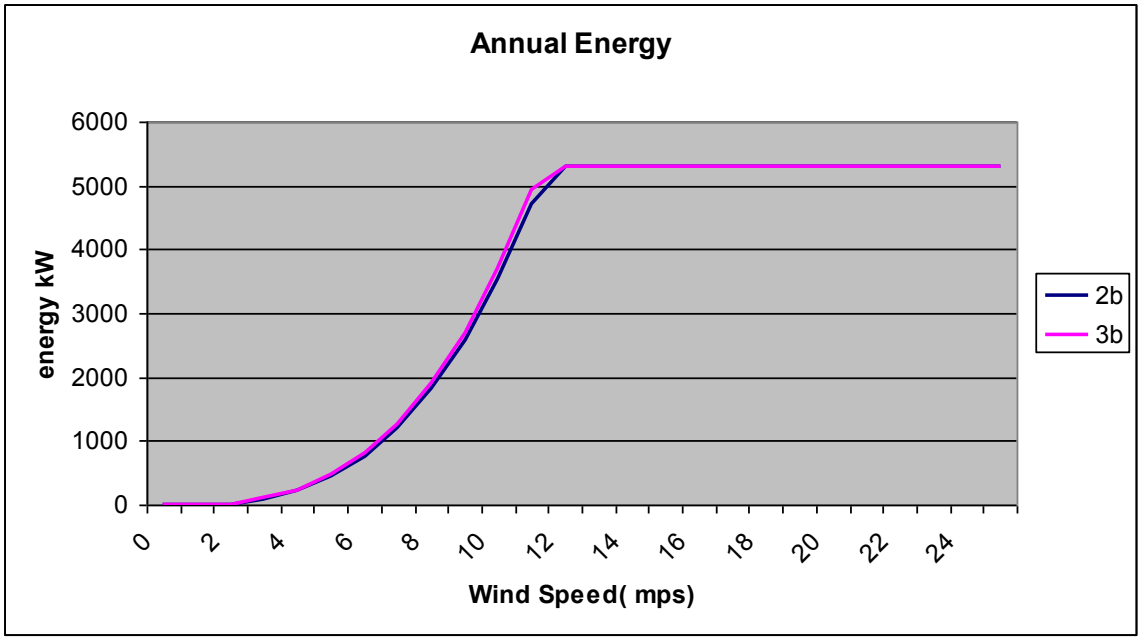

Figure 4.3 – Annual energy production at each wind speed

4.2 – Multi-body Dynamic Floating Platform Wind Turbine Results

4.2.1 - Description of Test Cases

We used NREL's FAST to compare floating platform three and two-bladed models. The three-bladed rotors ran at a rotor speed of 13 rpm. The two bladed models ran at a rotor speed of 16 rpm. The two bladed models used a teeter hinge at the hub. We used two different control systems: pitch-to-feather and pitch-to-stall (described earlier). We used the control system natural frequencies reported earlier for each platform, with one exception. For the two-bladed, pitch-to-stall, configuration of the MIT/NREL tension leg platform we used a natural frequency of 0.1 rad/s. We chose a lower natural-frequency because at higher natural frequencies we encountered instability. Four different platform configurations were tested: rigidly cantilevered to inertia frame, OC3/Hywind spar buoy, MIT/NREL tension leg platform (TLP), and ITI Energy barge. We ran all models for a hundred seconds at a steady 13 mps wind speed.

We choose six outputs for this thesis: Flap-wise bending moment of blade 1, the low-speed shaft bending moment, low-speed shaft torque, tower-top bending moment and tower-base bending moment, and rotor power. We choose these outputs because they are important design drivers and represent the loads moving through the wind turbine; starting at the blades, and ending at the base of the tower and platform. For each output there are time domain results for both the pitch-to-feather and pitch-to-stall. Below the time domain graphs are graphs containing the average, max and min values for each

configuration. The average and maximum and minimum values were taken from 30 to 100 seconds to allow for convergence.

Generally, the floating platform models experience higher loads and variation than the on-land model. The two-bladed models have higher blade loads but lower low-speed shaft bending and torque. This was to be expected. The teeter hinge decouples the shaft from the rotor reducing the variation and bending moment, however, two-blades carry more steady aerodynamic loading than three. The two-bladed models also experience lower torque than the three-bladed models. Again this is expected because the two-bladed models are running at a higher rotor rpm.

4.2.2 - Results

Figure 4.4-4.7 – Blade Root Flapwise Bending Moment Pitch-to-Feather and –Stall, Time Series and Maximum, Minimum, and Average (See Appendix for larger graphs)

Flapwise bending moment is the out-of-plane bending moment acting at the root of the blade. The floating platform models all oscillate more than the on-land reference. Comparing the floating platform models the two-bladed models have a higher mean than the three. The pitch-to-feather (P2F) barge has a larger range than the other P2F models. The two-bladed TLP pitch-to-stall (P2S) model operates much differently than the other models. This is due to the lower natural frequency of the control system.

Figure 4.8-4.11 – Low-Speed Shaft Bending Moment Pitch-to-Feather and –Stall, Time Series and Maximum, Minimum, and Average (See Appendix for larger graphs)

The low-speed shaft bending moment is the resultant of the 0 and 90 degree bending moments at the main bearing. The low-speed shaft feeds into the gearbox. The two-bladed models operate at a lower mean than the three-bladed models, including the on-land model. This is largely due to the addition of the teeter hinge in the two-bladed models. The teeter hinge decouples the out-of-plane bending loads on the rotor to the low-speed shaft. The barge model has the largest range of oscillation.

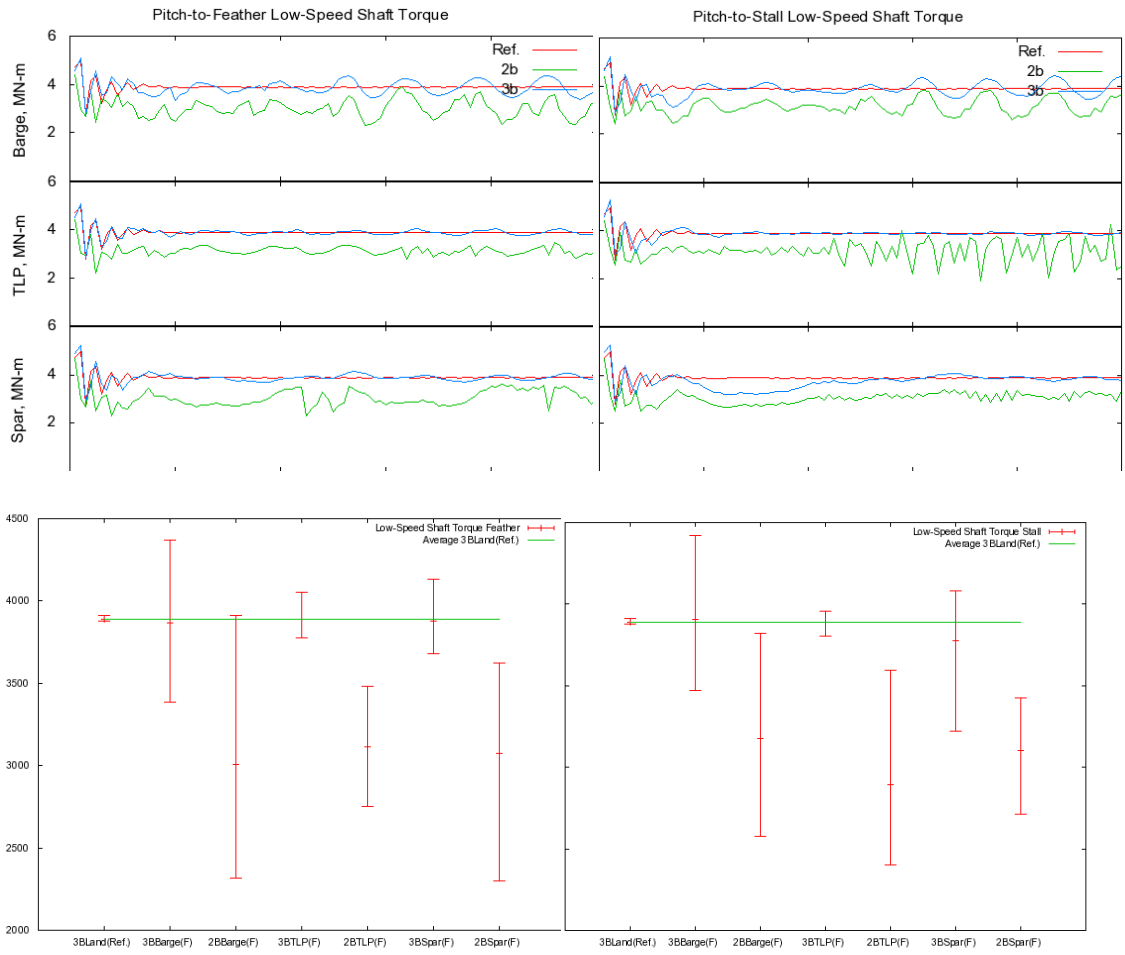

Figure 4.6 – Low-Speed Shaft Torque Pitch-to-Feather and –Stall, Time Series and Maximum, Minimum, and Average (See Appendix for larger graphs)

Low-speed shaft torque is constant along the shaft and is equivalent to the rotor torque. The mean value of the torque for the two-bladed models is lower than that for three-bladed models. This makes sense. Power is torque multiplied by rotational speed ($P = T\omega$). The two-bladed models operate at 16 rpm and the three-bladed models at 13 rpm. If the power is held constant, as it is in our case, and you increase the rotational speed the torque decreases.

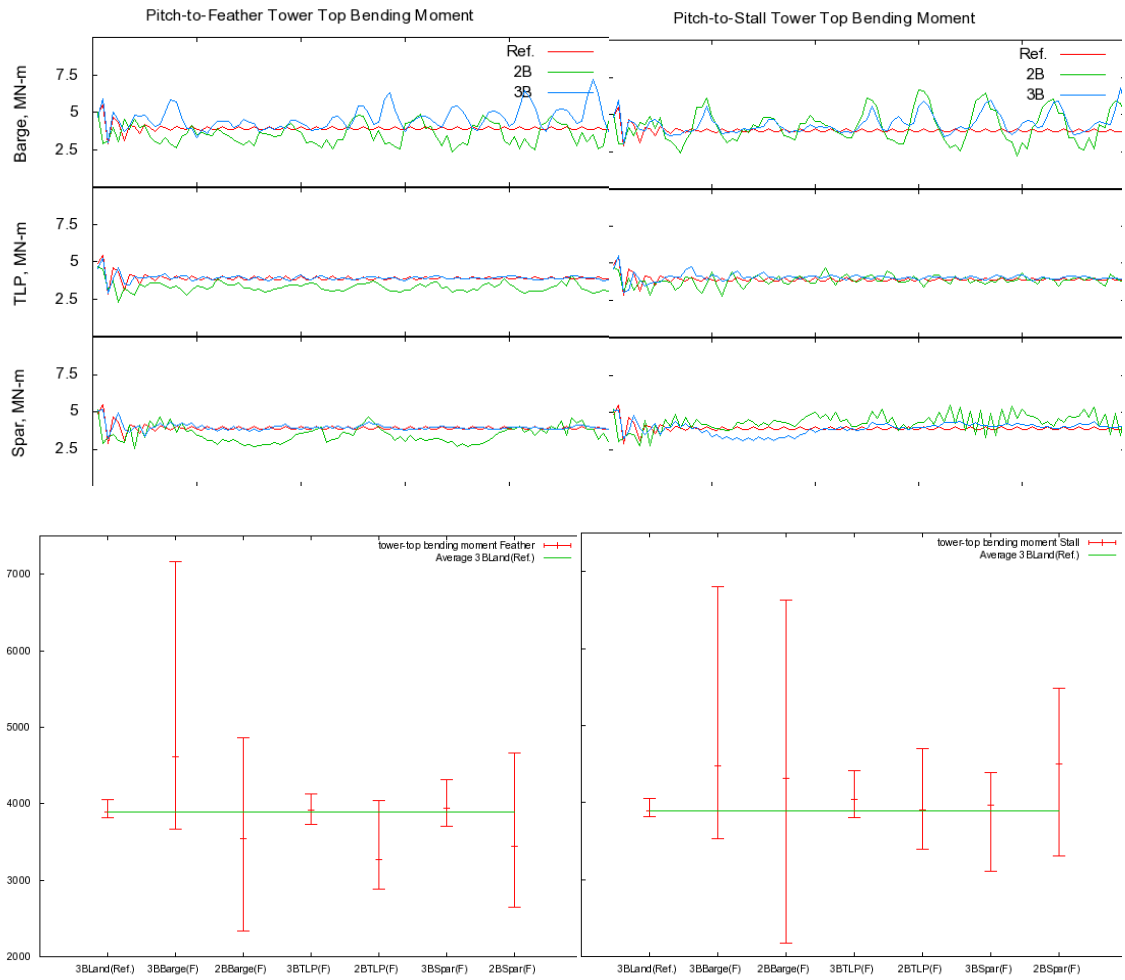

Figure 4.7 – Tower-Top Bending Moment Pitch-to-Feather and –Stall, Time Series and Maximum, Minimum, and Average (See Appendix for larger graphs)

The tower-top bending moment is the resultant bending moment of the tower-top / yaw bearing roll and pitch moments. The two-bladed models have a larger range than the three-bladed models. The P2S models have larger means than the P2F models. The P2F TLP three-bladed model acts very similar to the on-land reference model. The two-bladed P2F TLP and Spar models have lower means than the reference on-land turbine. The barge models oscillate the most of all the floating platforms.

Figure 4.8 – Tower-Base Bending Moment Pitch-to-Feather and –Stall, Time Series and Maximum, Minimum, and Average (See Appendix for larger graphs)

The Tower-Base Moment is the resultant of the tower base roll (or side-to-side) moment (i.e., the moment caused by side-to-side forces) and the tower base pitching (or fore-aft) moment (i.e., the moment caused by fore-aft forces). For both control systems the floating platforms operate at much wider max-min range than the on-land reference. The P2S models operate at a higher mean than P2F models. This is expected. P2S control operates in the stall region - where thrust is much higher than in P2F control. The P2F TLP designs operate close to the reference mean with smallest max-min range. There is

very little difference between two and three blades in the P2F models, with the two-bladed models operating at a slightly higher mean. However, with the P2S control models the two-bladed barge and spar models have slightly lower averages than the three-bladed models. The P2S TLP two-bladed model has higher mean and wider max-min range. This is different than the other models and may mean that the two-bladed configuration with the lower natural frequency did not address the instability in the two-bladed TLP P2S model.

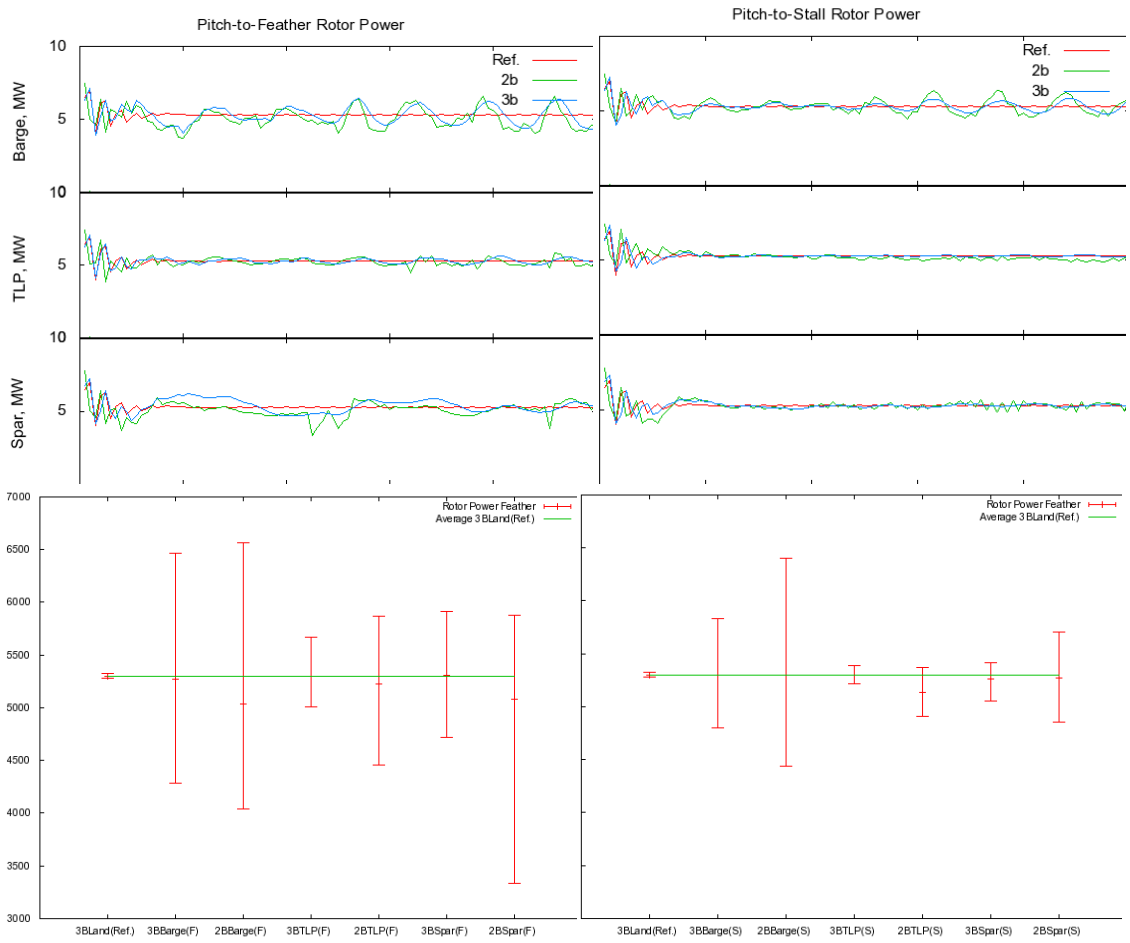

Figure 4.9 – Rotor Power Pitch-to-Feather and –Stall, Time Series and Maximum, Minimum, and Average (See Appendix for larger graphs)

Finally, we look at the rotor power. There is considerable variation between the on-land and floating platform power production. The barge has the largest range. The TLP has the least. The stall controlled floating platform has less variation compared to the P2F control. The increased thrust in the stall control shows the added damping effects on power production.

Chapter Five

Conclusions and Recommendations

FAST was used in this thesis to study multibody dynamics of three floating platform wind turbine systems. FAST determines loads and dynamics by balancing the inertial and external forces (aero-hydro-elastic). The aerodynamics are computed with Aerodyn and the hydrodynamics with Hydrodyn. Hydrodyn interfaces with an external wave-body interaction program, WAMIT and a quasi-static mooring system model.

A generator torque constant was found for the control law used for both the two and three bladed rotors. The generator torque constant is used to maintain tip-speed ratio in region 2 (below rated generator capacity). Pitch-to-Feather and Pitch-to-Stall control algorithms were developed for a 13 rpm three blade rotor, and a 16 rpm two blade rotor. To maintain power production at 5MW above rated wind speed, WT_Perf was used to determine the required pitch angle at various wind speeds. A frozen-wake version of

FAST was used to determine the pitch sensitivity at incremental wind speeds above rated. For the Pitch-to-Feather control logic a linear relationship was deduced from the pitch sensitivity plot. The linear relationship found was used to create a Gain Correction Factor. For the Pitch-to-Stall control logic the pitch sensitivity was double valued to reduce complexity; single value gains were chosen for the control algorithm.

It was noted for the floating offshore configurations considered, lower wind turbine natural frequencies to exist. Using published results, different/lower values for the natural frequency were used to determine the control gains.

Using a Rayleigh wind speed distribution and WT_Perf the annual energy production was determined. We took advantage of the control concept that below the rated capacity of the generator the rotor speed is changed to match the tip-speed ratio, and at rated the capacity the power produced remains constant. By using the optimal tip-speed ratio we found the rotor speed for incremental wind speeds. The two bladed rotor reached rated capacity around 16 rpm and the three bladed rotor at 13 rpm. Finding the power produced at incremental wind speeds, the amount of time spent at each wind speed and multiplying by the number of hours in a year we computed the annual energy.

There is a 1.6% difference in annual energy production between the two and three bladed rotors used in our analysis. This result was obtained without optimizing the blade of the two bladed rotor, as the two-bladed configuration was selected by simply removing one blade from a three blade configuration. If the two-bladed rotor were optimized by

increasing the chord length and adjusting for Reynolds number an increase if rotor efficiency would be found. Increase in efficiency would lead to an increase in the annual energy production of a two bladed rotor.

All analyses used NREL's 5MW Baseline Offshore wind turbine. We modeled a two-bladed rotor with teeter hinge and a three-bladed rotor. Four different platform configurations were used for comparisons: rigidly cantilevered to inertia frame, spar buoy, tension leg platform (TLP), and barge. For each configuration, we used a pitch-to-feather and pitch-to-stall control algorithms. The rated speed for the three-bladed rotor was 13 rpm and 16 rpm for the two-bladed rotor. All tests were conducted at a wind speed of 13 mps for 100 seconds

A general observation from our results is the large variability entered into the maximum and minimum values due to the floating platform environment. This was expected, but this study provides a quantitative basis for the variability range. The floating platform wind turbine designs presented here are simply the combination of on-land wind turbine technology on a floating platform.

Another general observation was the problems we experienced with the two-bladed pitch-to-stall TLP model. The natural frequency of the control algorithm was reduced (from 0.6 rad/s to 0.1 rad/s) to reduce the effects of an instability. The reduction in natural frequency removed most of the problem but the instability can be seen growing in the low-speed shaft torque. Of the three platforms, the TLP is the most complex. For the TLP model, reducing the number of blades by one, while maintaining the remaining

design elements may not be sufficient to obtain stability. Reconfiguring of the tension in the lines and size and shape of the ballasts may need to be redesigned to maintain stability. The instability does raise questions about the current design. If tension is lost in one of the cables, the turbine will fall into the ocean. Given the extreme variability of the ocean environment having such a complex mechanism to find stability may not be the best path for a floating platform wind turbine.

The low speed shaft connects the rotor and gearbox (or direct-drive generator). In the two-bladed model a teeter hinge was added to the model. The low-speed shaft moment was the smallest and shows the benefits of decoupling the tangential and thrust loads. The lower bending moments in the shaft and smaller variations could be a major advantage in the offshore environment. Failures in the gearboxes are major source of downtime in on-land wind turbines. Lowering the low-speed shaft moments could increase the operation life of the gearbox. Maintenance and operation costs in the offshore environment are expected to be higher than on-land. Decreasing downtime due to faulty gearbox operation will increase the economic viability of a floating wind turbine.

Based on the results of this study of two-bladed rotors should be further developed and optimized for offshore floating wind turbines. The potential reduction in costs by eliminating one blade, reducing top-of-tower weight, and the reducing the loads on the critical drive train components are significant advantages for two-bladed . It would be of

interest to perform a statistical analysis of an optimized two-bladed model based on the design loads outlined in the standard IEC 61400-3. Also a more complete picture of how the 2 bladed concept would perform in extreme conditions would be beneficial. In the longer term, it would also be of interest to perform a fatigue analysis on a complete system design.

Modeling a downwind two-bladed wind turbine should be considered. Currently adding a coning angle to an upwind machine is done largely to avoid the blades hitting the tower. In a downwind configuration, blades bend further awary for the tower under higher aerodynamic thrust. In this case the coning angle could be used to reduce mean bending moments and counter the aerodynamic thrust loads to the blades. It might also allow for passive yaw control removing the need for an additional complex control system.

Our results are not as dramatic as expected. Upon a closer look, the weight of the platforms might explain this effect. The NREL baseline 5MW wind turbine model weighs just under 1,000,000 million kgs. The OC3 spar buoy and TLP models are 7,000,000 and 8.000,000 kgs respectfully. The barge is the least heavy at 5,000,000 kgs. Such a large increase in weight makes the removable of one blade almost insignificant. The large weights of the floating platform are probably due to wanting to add stability to the tower motions. These large weights have a cost.

As the floating platform offshore wind turbine design process moves forward a more integrated approach to platform, wind turbine and the environment should be considered.

The evolution of design for the current on-land wind turbine however helpful may not be applicable. Current platform models follow the three basic physical classifications to find stability in an offshore environment. An on-land wind turbine was simply added to these platforms. New "out-side-the-box" designs for the tower and platforms for the unique loads and dynamics a floating wind turbine would experience.

References

1. "Energy from Offshore Wind," W. Musial and S. Butterfield, B. Ram, National Renewable Energy Lab, Feb. 2006
2. "Engineering Challenges for Floating Offshore Wind Turbines," S. Butterfield, W. Musial, J. Jonkman, P. Sclavounos, National Renewable Energy Lab, Sept. 2007
3. "MOD-5B Wind Turbine System Final Report, Volume 1, Executive Summary," prepared by Beoing Aerospace Company for National Aeronautics and Space Administration, March 1988
4. Engineering Fluid Mechanics, Crowe Elgar Roberson, Wiley Books
5. "Wind Turbine Blade Analysis using the Blade Element Momentum Method. Version 1.0" Grant Ingram, School of Engineering, Durham University, December 2005.
6. "A Brief Synopsis of Kane's Method" paper synopisis
7. Multibody Dynamics Ronald L. Huston, Butterworth-Heinemann , 1990
8. Computational Methods in Multibody Dynamics, Faid. M. L. Amirouche, Prentice Hall, 1992.
9. Dynamics: Theory and Applications, Thomas R. Kane and David A. Levinson, Mcgraw-Hill Book Company. 1985

10. Engineering Mechanics, Dynamics, R. C. Hibbeler, Pearson Prentice Hall, Tenth Edition, 2004
11. "Design of Support Structures for Offshore Wind Turbines," Jan VAN DER TEMPEL, PhD thesis, de Technische Universiteit Delft, April 2006
12. FAST_AD Advanced Dynamics Code, Wilson, Walker and Heh, Oregon State University and NREL, 1999
13. "Definition of the Floating System for Phase IV of OC3," J. Jonkman, NREL Wind Technology Center, February, 2009
14. "Aeroelastic Instabilities of large Offshore and Onshore Wind Turbines," G. Bir and J. Jonkman, National Renewable Energy Lab, Aug. 2007
15. "Development and Verifiction of a Fully Coupled Simulator for Offshore Wind Turbines," J. Jonkman, andM. Buhl, Jr. 45th AIAA Aerospace Sciences Meeting and Exhibit, Wind Energy Symposium, Reno, Nevada Jan. 2007
16. Low Wind Speed Technology Phase II: Offshore Floating Wind Turbine Concepts:
17. Fully Coupled Dynamic Response Simulations
18. "Dynamics Modeling and Loads Analysis of an Offshore Floating Wind Turbine," J. Jonkman, Technical Report, NREL, November, 2007.
19. "Guided Tour on Wind Energy," presentation, www.windpower.org
20. "Definition of a 5-MW Reference Wind Turbine for Offshore System Development," J. Jonkman, S. Butterfield, W. Musial, and G. Scott, NREL Technical Report, February 2009

21. FAST User's Guide, Jason M. Jonkman, Marshall L. Buhl Jr., NREL Technical Report, August 2005

22. Bulder, B. H., et al, *Study to Feasibility of and Boundary Conditions for Floating Offshore Wind Turbines*, Novem 2002-CMC-R43, ECN, MARIN, Lagerway the Windmaster, TNO, TUD, MSC, December 2002.

23. Lee, K. H., *Responses of Floating Wind Turbines to Wind and Wave Excitation*, M.S. Dissertation, Department of Ocean Engineering, Massachusetts Institute of Technology, Cambridge, MA, USA, January 2005

24. Wayman, E. N., Sclavounos, P. D., Butterfield, S., Jonkman, J., and Musial, W., "Coupled Dynamic Modeling of Floating Wind Turbine Systems," *2006 Offshore Technology Conference, 1–4 May 2006, Houston, TX* [CD-ROM], Richardson, TX: Offshore Technology Conference, May 2006, OTC 18287, NREL/CP-500-39481, Golden, CO: National Renewable Energy Laboratory.

25. Wayman, E., *Coupled Dynamics and Economic Analysis of Floating Wind Turbine Systems*, M.S. Dissertation, Department of Mechanical Engineering, Massachusetts Institute of Technology, Cambridge, MA, USA, June 2006.

26. Henderson, A. R. and Patel, M. H., "On the Modelling of a Floating Offshore Wind Turbine," *Wind Energy*, Vol. 6, No. 1, February 2003, pp. 53–86.

27. Larsen, T. J. and Hanson, T. D., "A Method to Avoid Negative Damped Low Frequent Tower Vibrations for a Floating, Pitch Controlled Wind Turbine," *Journal of Physics: Conference Series, The Second Conference on The Science of Making Torque From Wind, Copenhagen, Denmark, 28–31 August 2007*, [online journal], Vol. 75, 2007, 012073, URL: http://www.iop.org/EJ/article/1742-

6596/75/1/012073/jpconf7_75_012073.pdf?request-id=SpEuhRBu3BG0xV3r2wi7Kg, [cited 28 August 2007].

28. Nielsen, F. G., Hanson, T. D., and Skaare, B., "Integrated Dynamic Analysis of Floating Offshore Wind Turbines," *Proceedings of OMAE2006 25th International Conference on Offshore Mechanics and Arctic Engineering, 4–9 June 2006, Hamburg, Germany* [CD-ROM], Houston, TX: The American Society of Mechanical Engineers (ASME International) Ocean, Offshore and Arctic Engineering (OOAE) Division, June 2006, OMAE2006-92291.
29. Skaare, B., Hanson, T. D., and Nielsen, F. G., "Importance of Control Strategies on Fatigue Life of Floating Wind Turbines," *Proceedings of OMAE2007 26th International Conference on Offshore Mechanics and Arctic Engineering, 10–15 June 2007, San Diego, CA* [CD-ROM], Houston, TX: The American Society of Mechanical Engineers (ASME International) Ocean, Offshore and Arctic Engineering (OOAE) Division, June 2007, OMAE2007-29277.
30. email conversation with Jason Jonkman, march 4, 2009
31. "Model Development and Loads Analysis of an Offshore Wind Turbine on a Tension Leg Platform, with a Comparison to Other Floating Turbine Concepts," Murtha, Denis, NREL, April 2009
32. Vijfhuizen, W. J. M. J, Design of a Wind and Wave Power Barge, M.S. Dissertation, Department of Naval Architecture and Mechanical Engineering, Universities of Glasgow and Strathclyde, Glasgow, Scotland, September 2006
33. "Design of Support Structures for Offshore Wind Turbines," Jan VAN DER TEMPEL, de Technische Universiteit Delft, April 2006

34. “A Quantitative Comparison of the Responses of Three Floating Platforms,” Jonkman, and Mutha, NREL, 2009

35. “Seeking Wind Energy, Some Consider the Sea,” Henry Fountain, The New York Times, November 18, 2009

36. “WT_PERF USER’S GUIDE,” Marshall L. Buhl, Jr. National Wind Technology Center, National Renewable Energy Laboratory, Golden, Colorado

Appendix

Time Domain Results

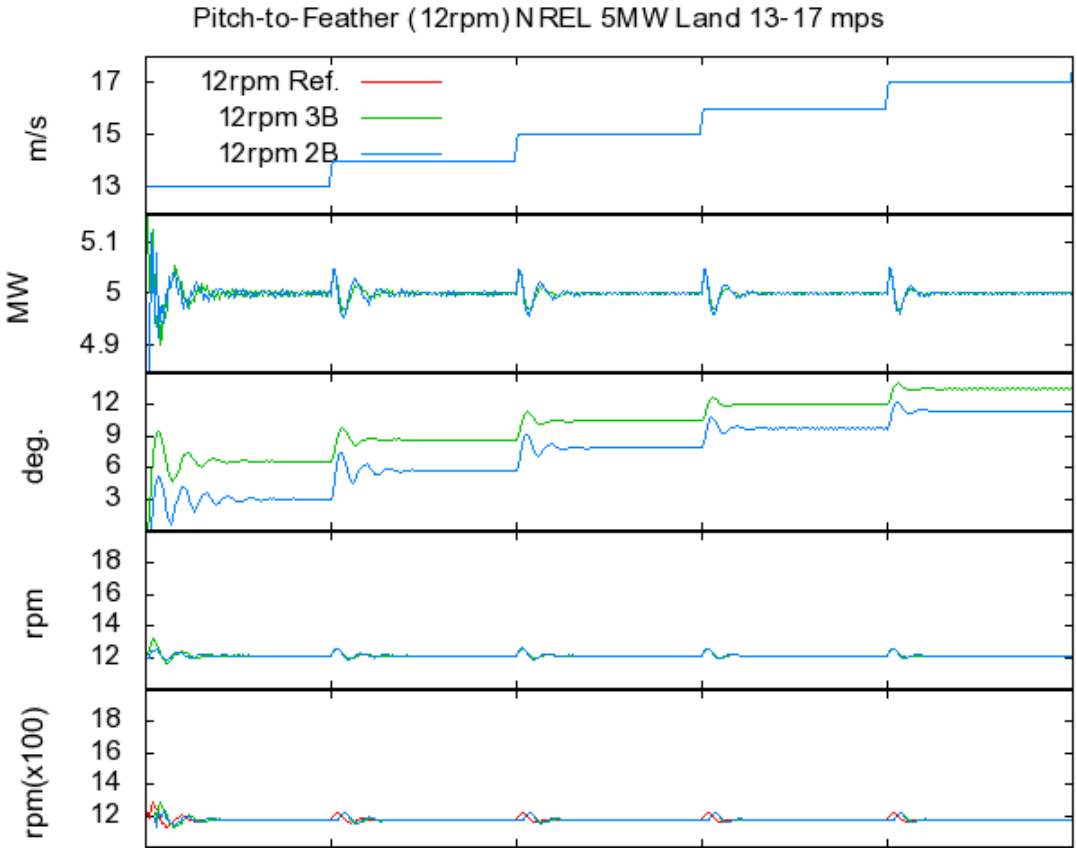

Figure A.1 – Performance Parameters from top: Wind Speed, Generator Power, Blade Pitch, Rotor Speed, Generator Speed (values are multiplied by 100) – two and three blade 12 rpm – Pitch-to-Feather Control Algorithm

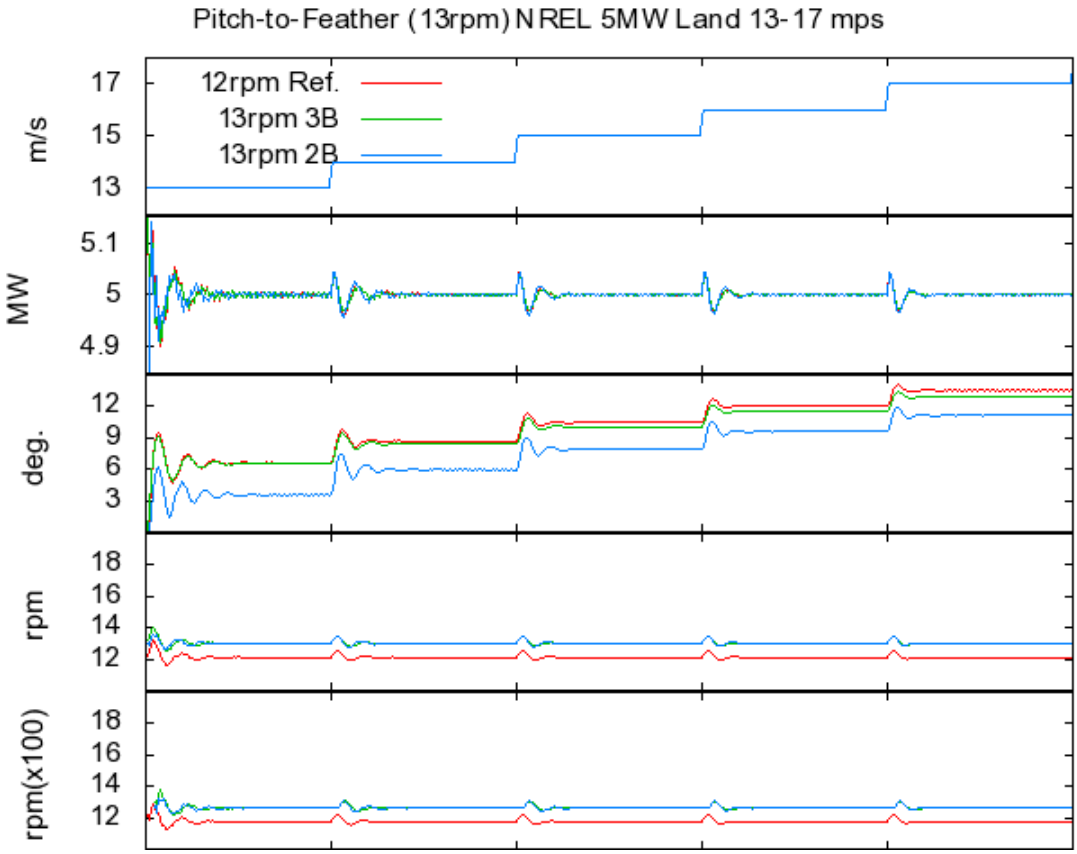

Figure A.2 – Performance Parameters from top: Wind Speed, Generator Power, Blade Pitch, Rotor Speed, Generator Speed (values are multiplied by 100) – two and three blade 13 rpm – Pitch-to-Feather Control Algorithm

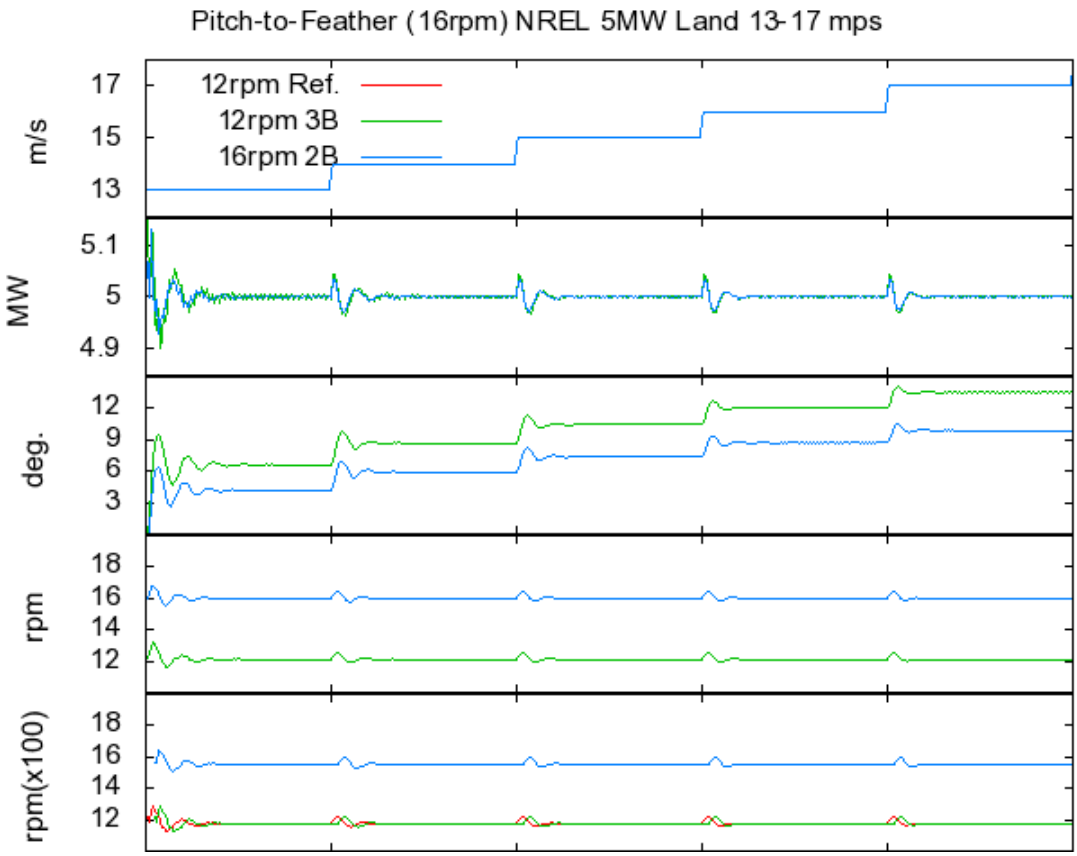

Figure A.3 - Performance Parameters from top: Wind Speed, Generator Power, Blade Pitch, Rotor Speed, Generator Speed (values are multiplied by 100) – two blade 16 rpm and three blade 13 rpm – Pitch-to-Feather Control Algorithm

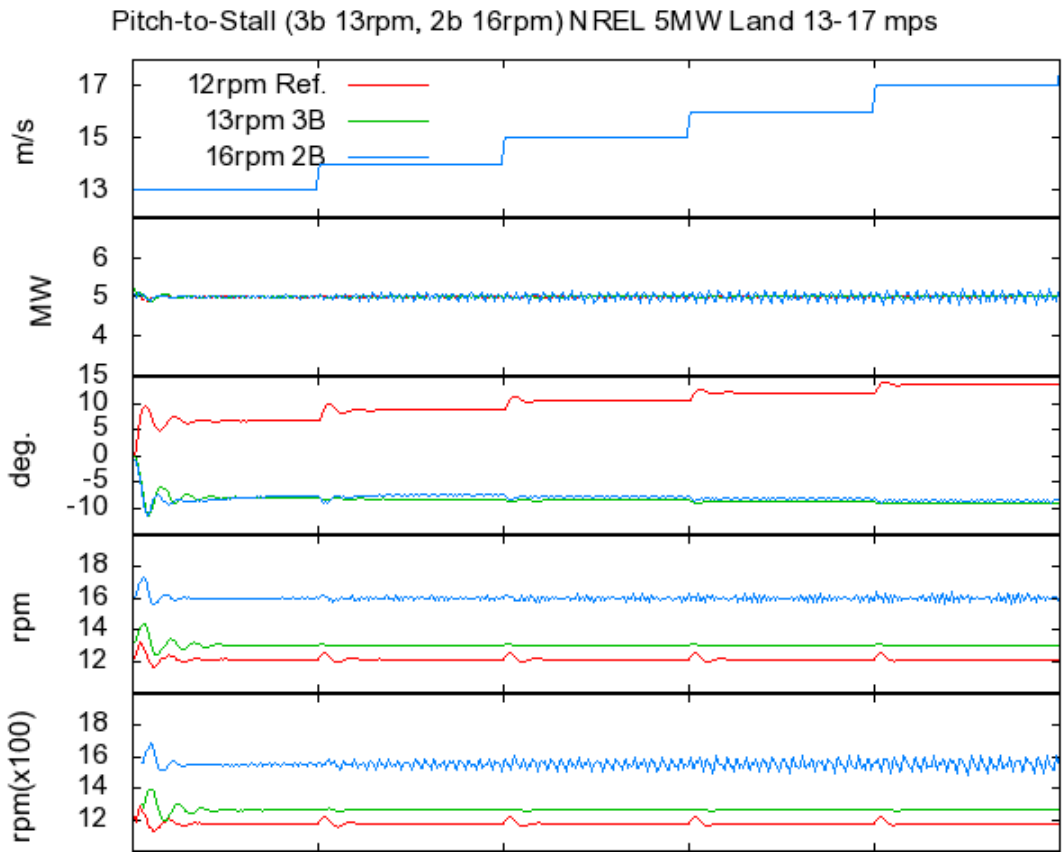

Figure A.4 - Performance Parameters from top: Wind Speed, Generator Power, Blade Pitch, Rotor Speed, Generator Speed (values are multiplied by 100) – two blade 16 rpm and three blade 13 rpm – Pitch-to-Stall Control Algorithm

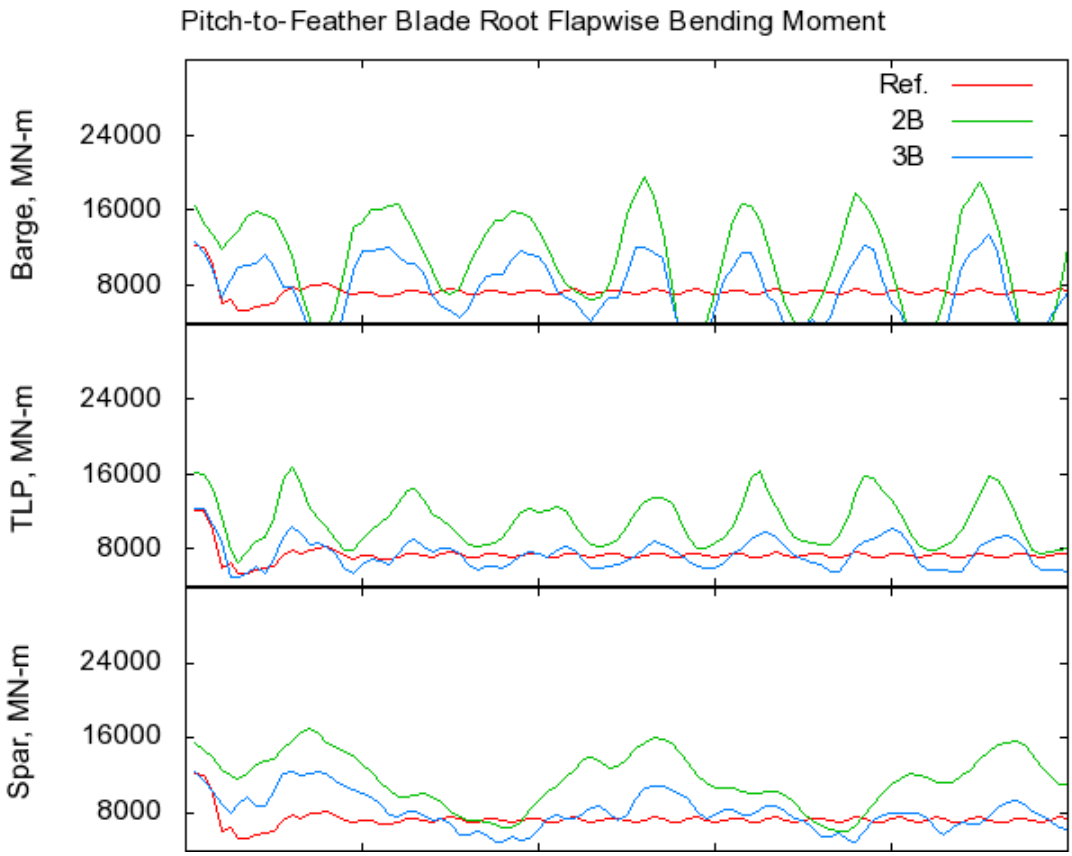

Figure A.5 - Blade Root Flapwise Bending Moment Pitch-to-Feather Time Series

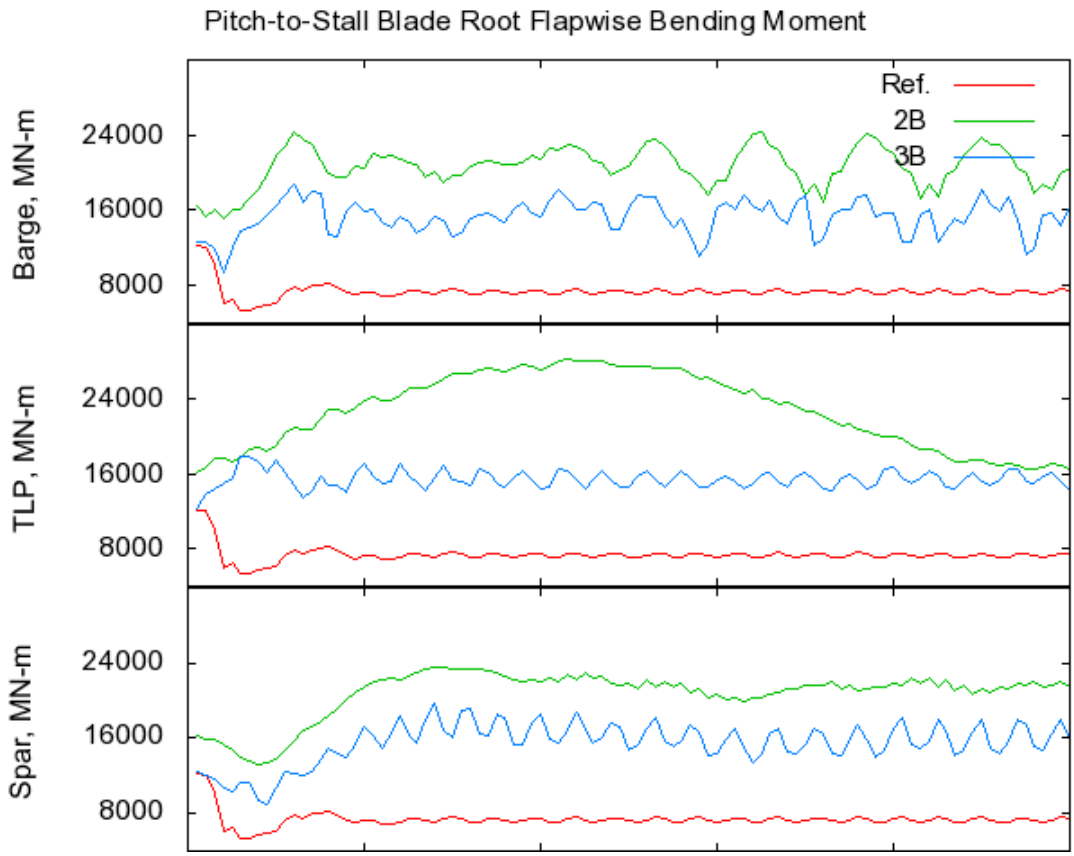

Figure A.6 - Blade Root Flapwise Bending Moment Pitch-to–Stall, Time Series

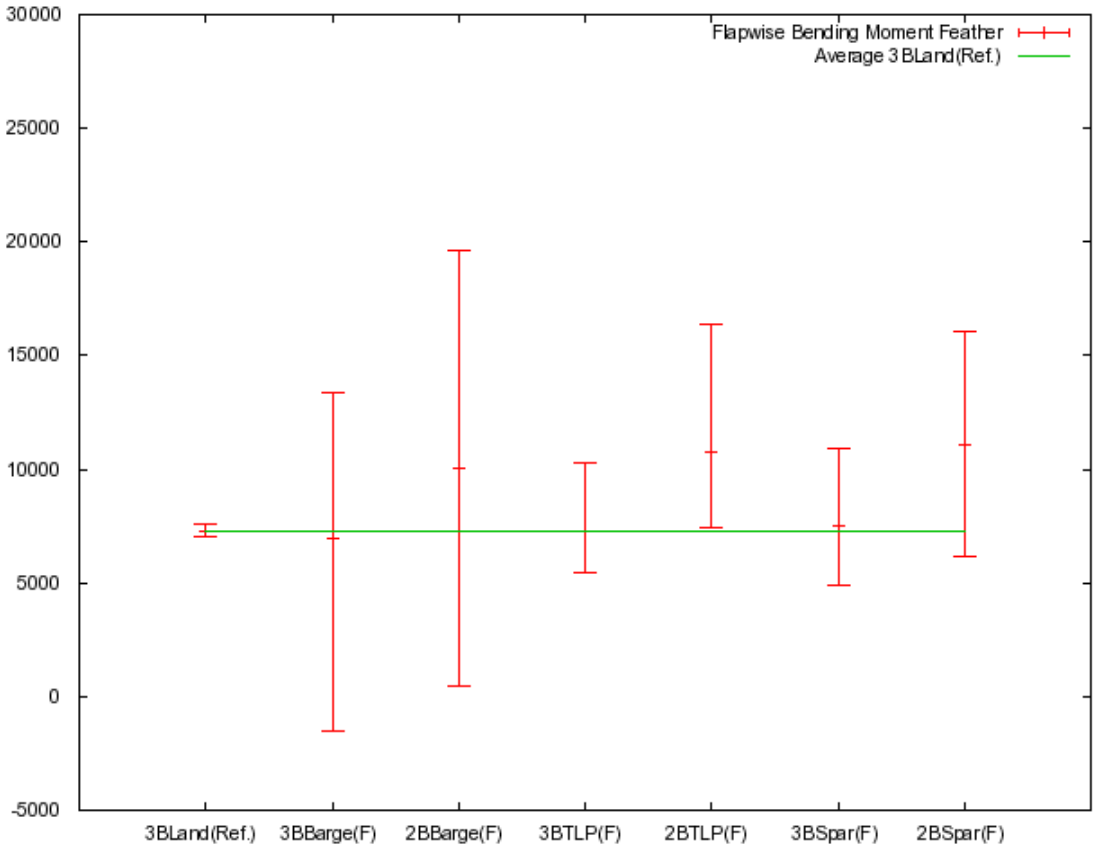

Figure A.7 - Blade Root Flapwise Bending Moment Pitch-to-Feather Maximum, Minimum, and Average

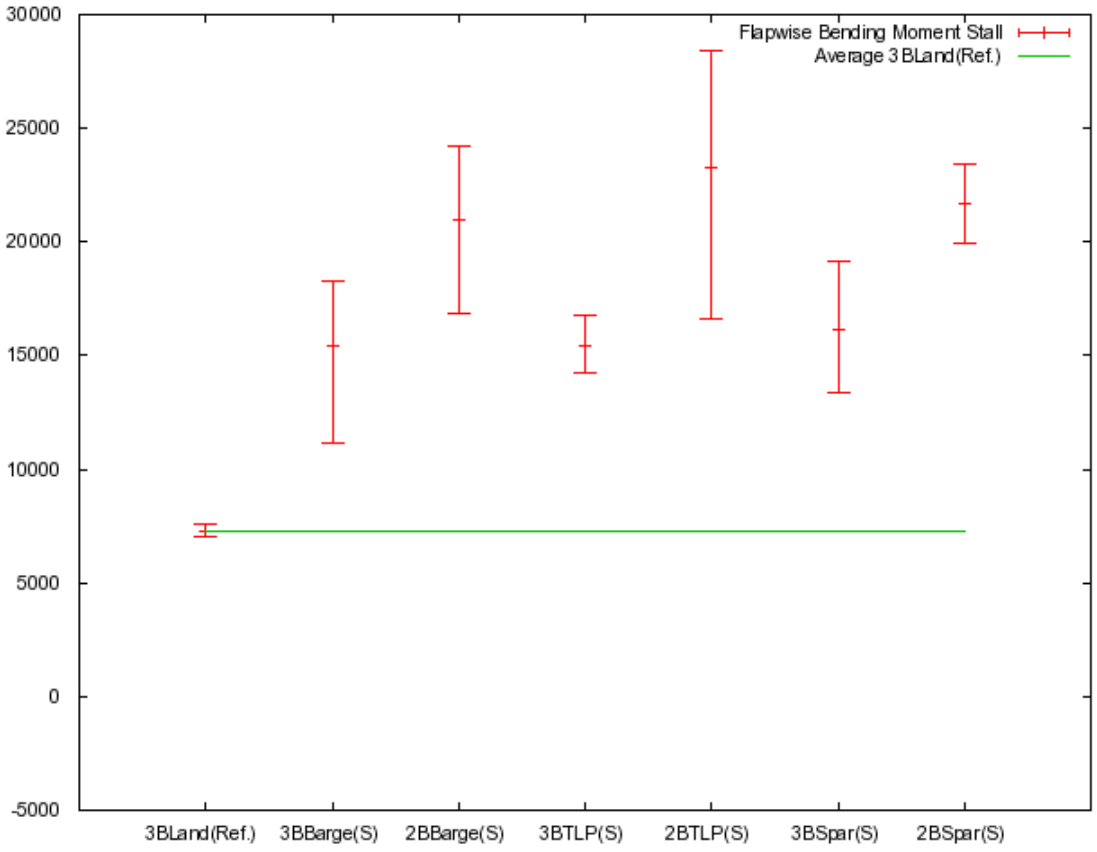

Figure A.8 - Blade Root Flapwise Bending Moment Pitch-to-Stall, Maximum, Minimum, and Average

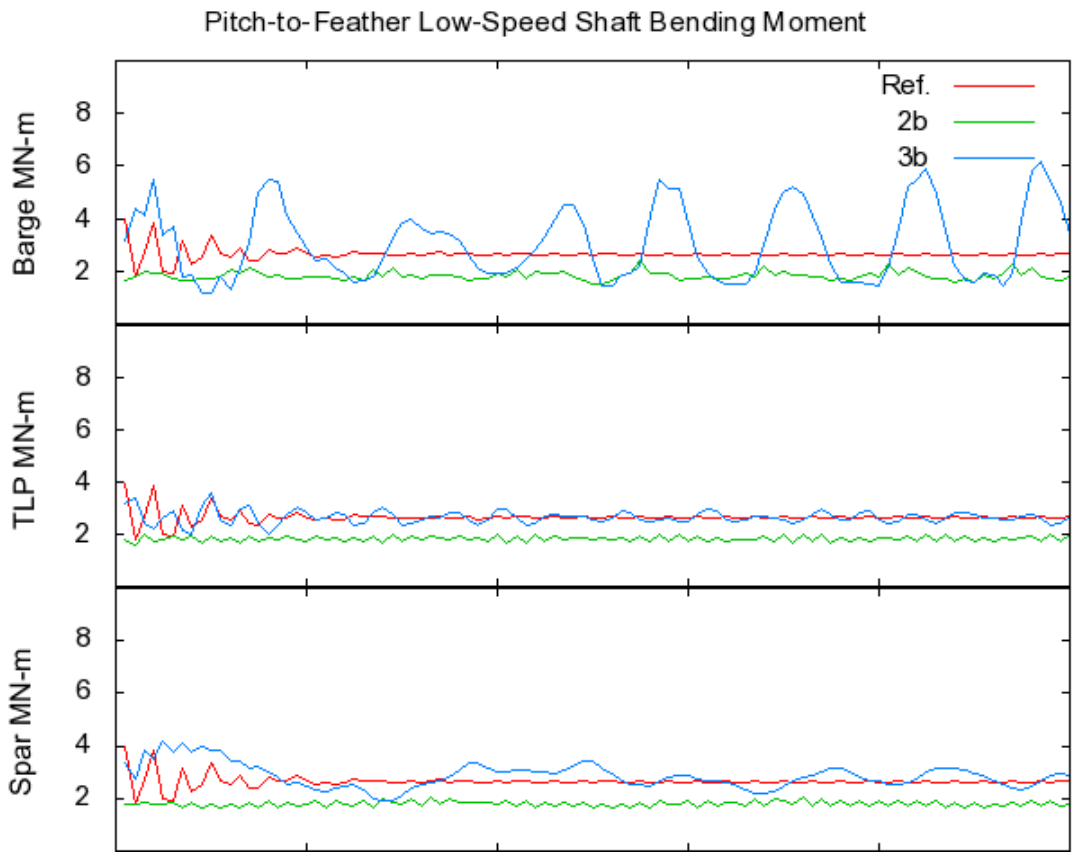

Figure A.9 - Low-Speed Shaft Bending Moment Pitch-to-Feather, Time Series

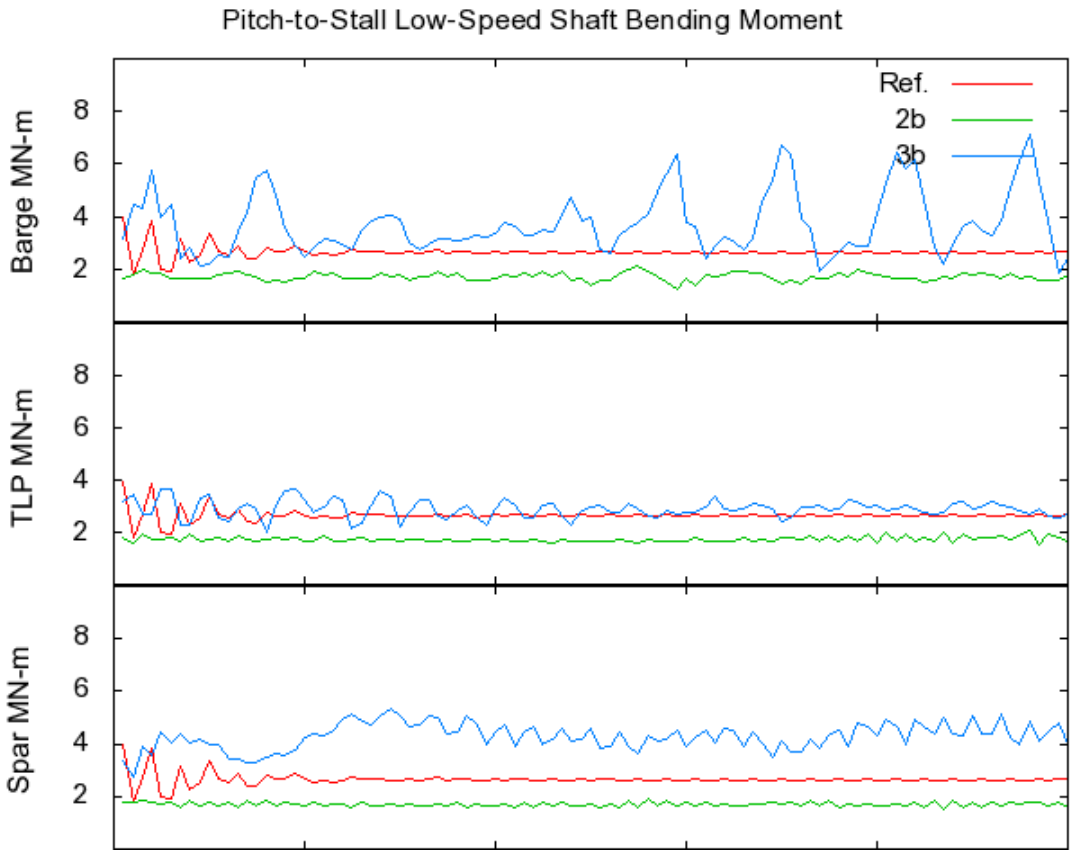

Figure A.10 - Low-Speed Shaft Bending Moment Pitch-to-Stall, Time Series

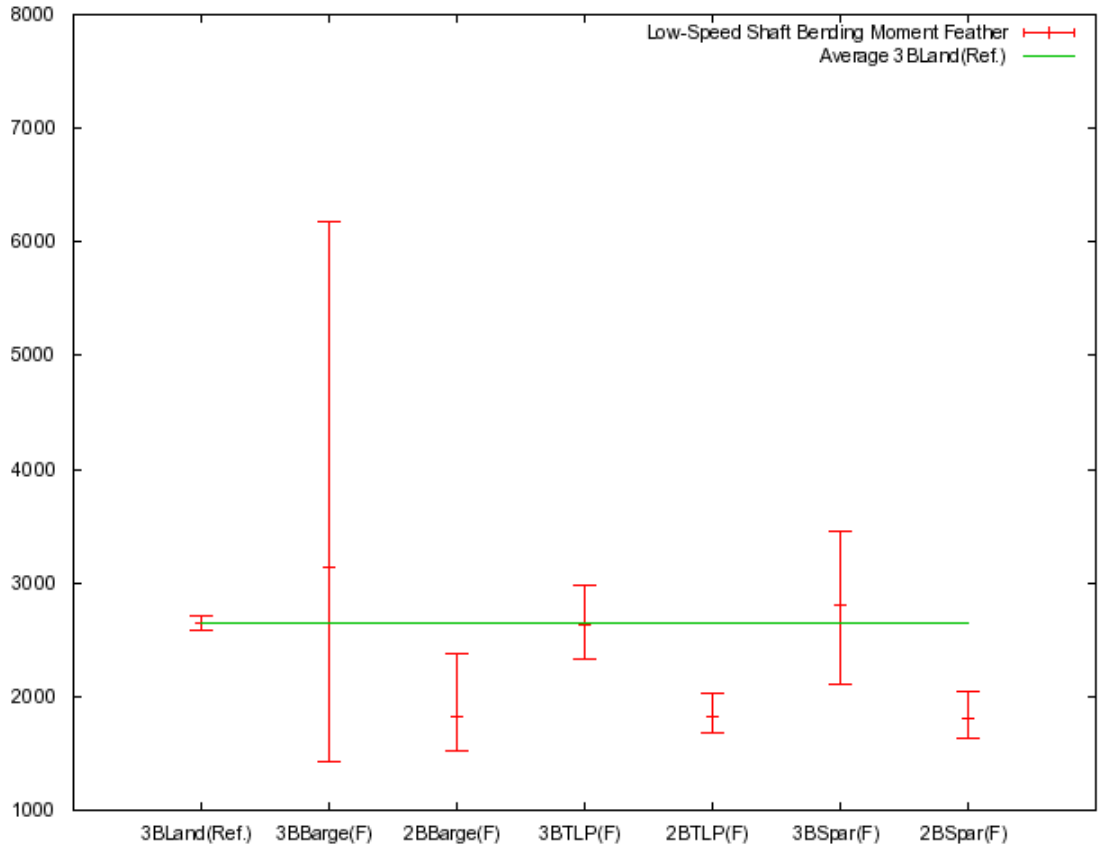

Figure A.11 - Low-Speed Shaft Bending Moment Pitch-to-Feather Maximum, Minimum, and Average

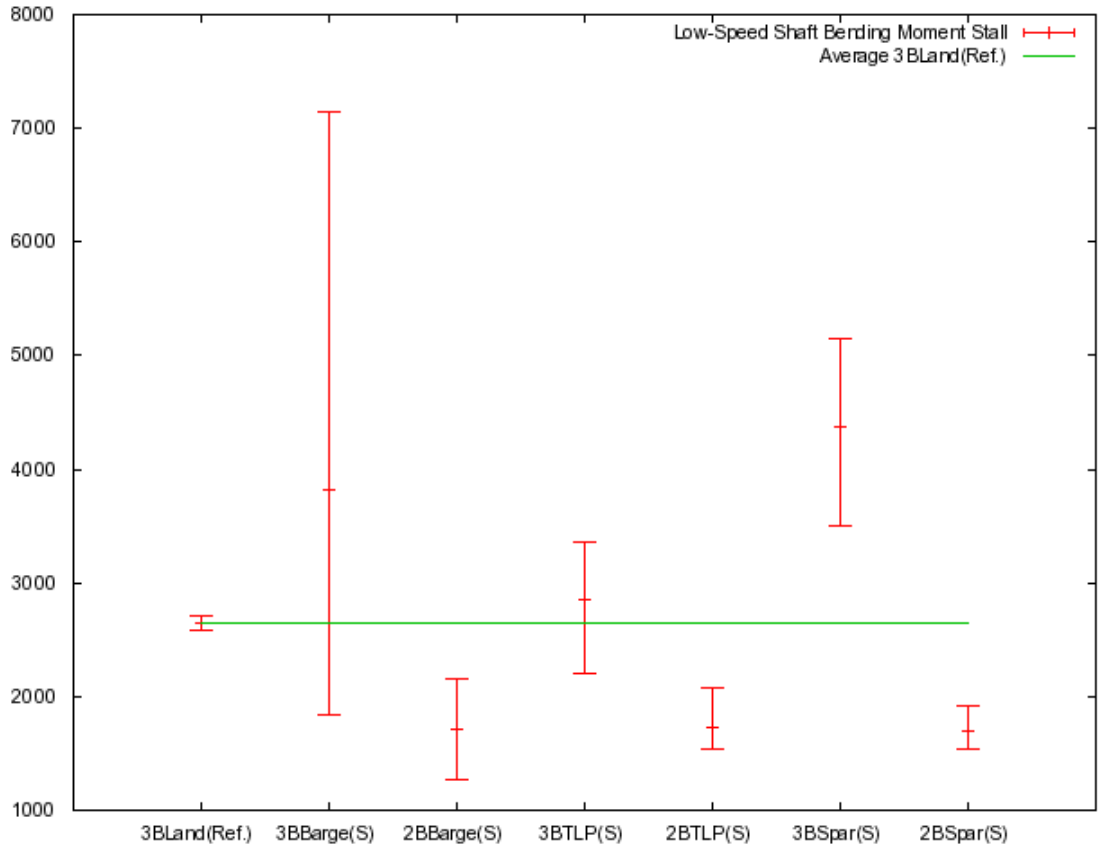

Figure A.12 - Low-Speed Shaft Bending Moment Pitch-to- Stall, Maximum, Minimum, and Average

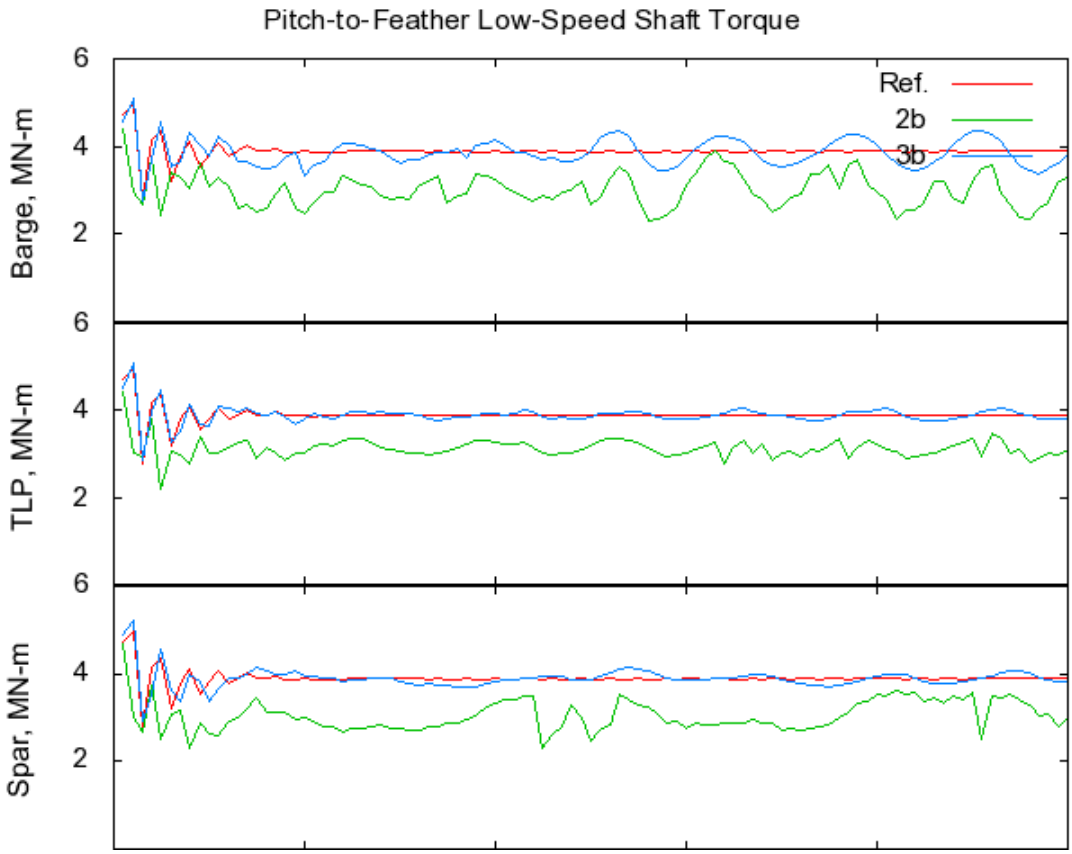

Figure A.13 - Low-Speed Shaft Torque Pitch-to-Feather Time Series

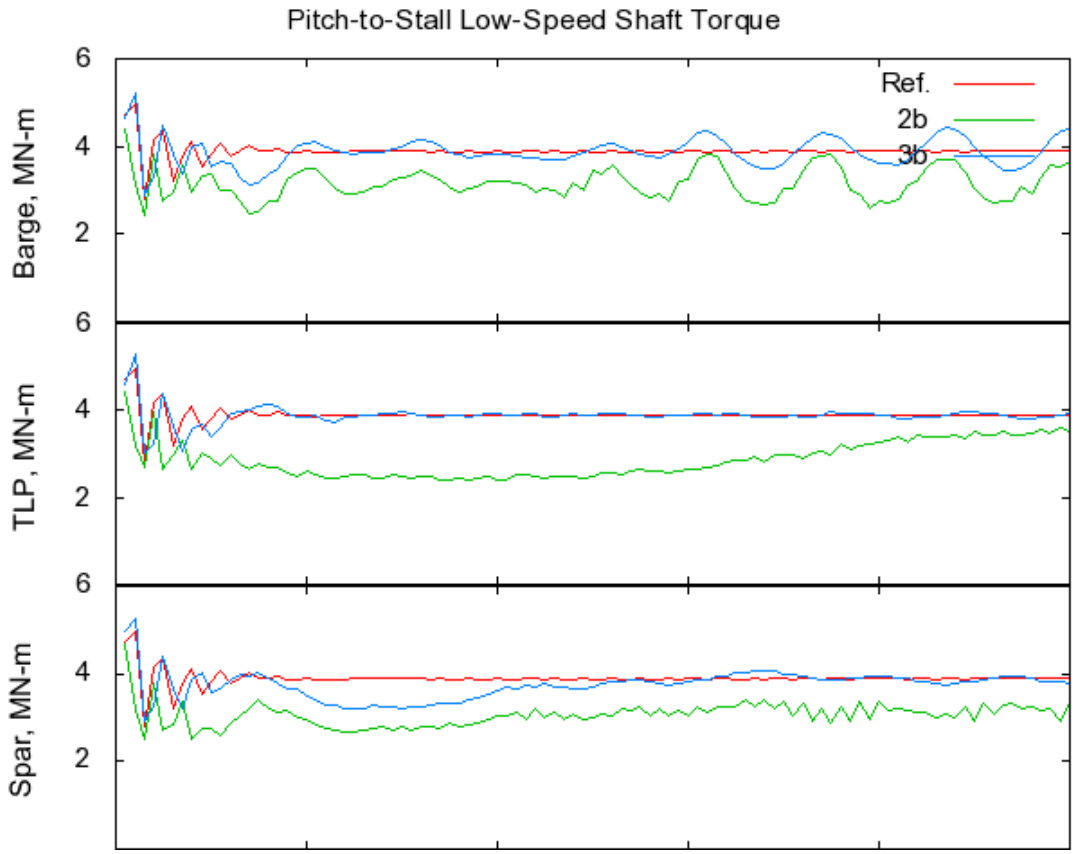

Figure A.14 - Low-Speed Shaft Torque Pitch-to-Stall, Time Series

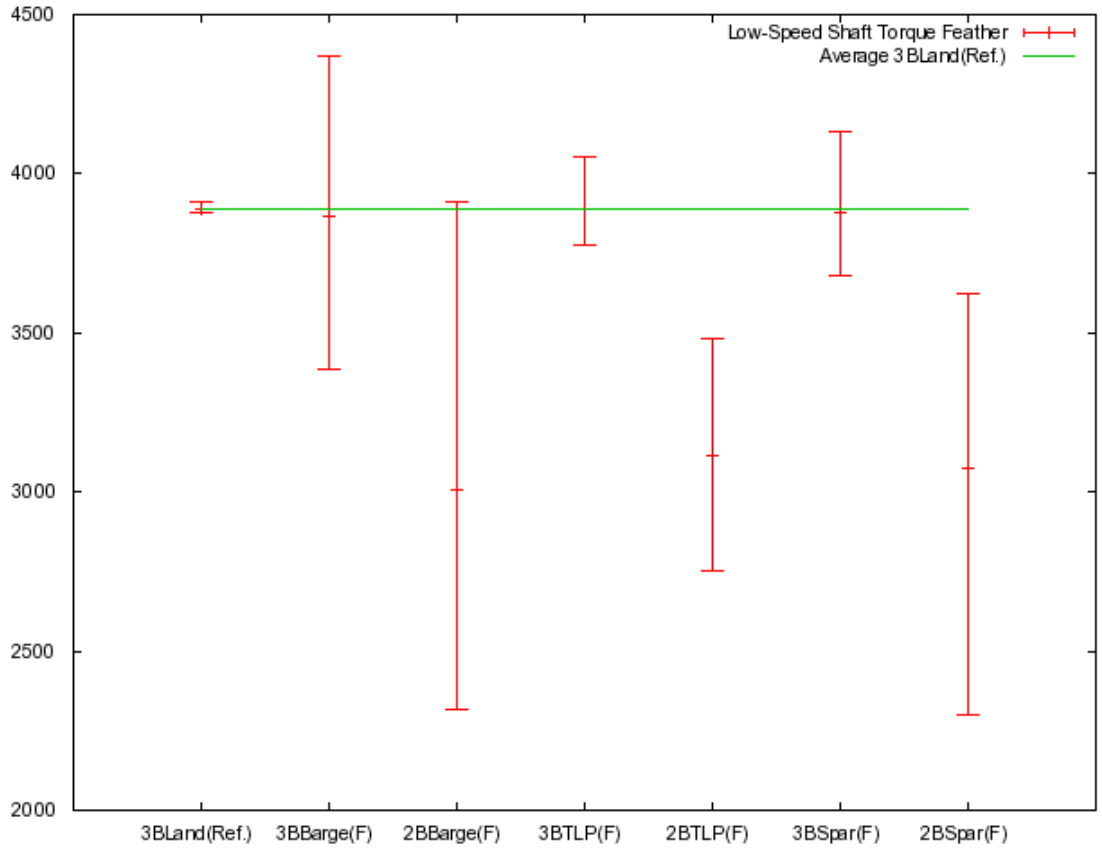

Figure A.15 - Low-Speed Shaft Torque Pitch-to-Feather Maximum, Minimum, and Average

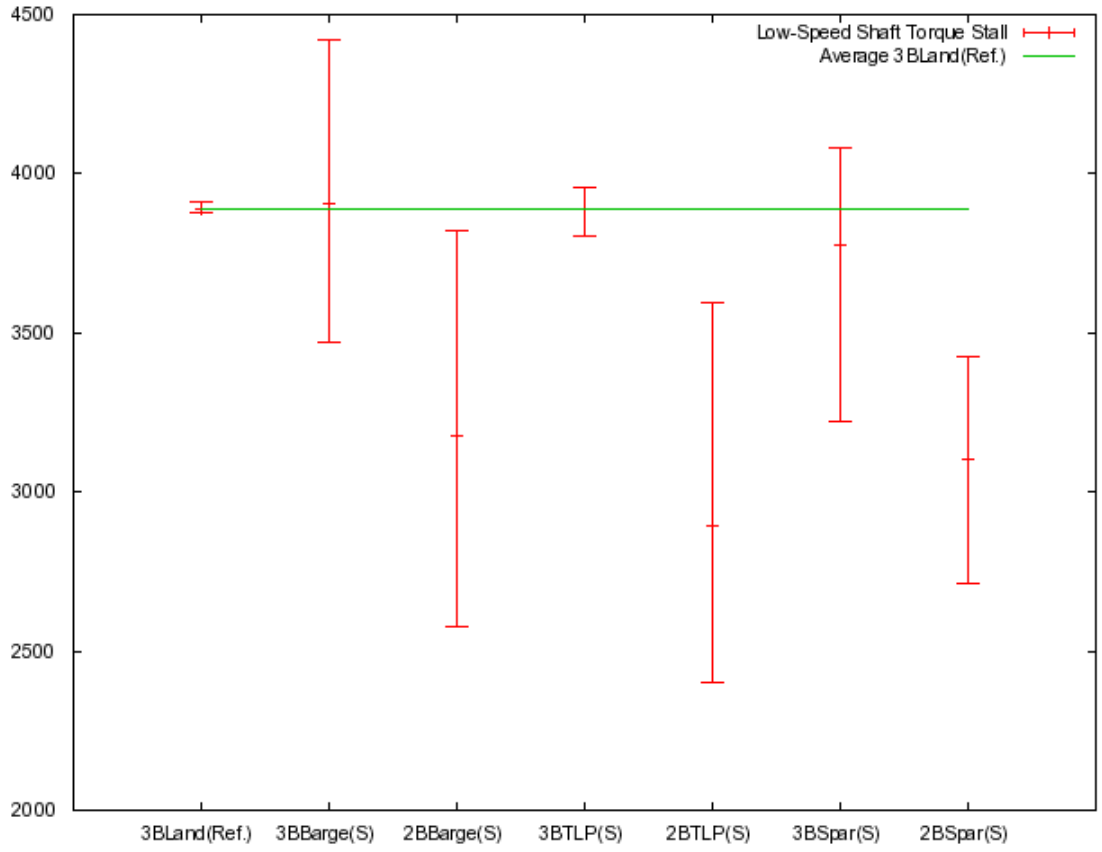

Figure A.16 - Low-Speed Shaft Torque Pitch-to-Stall, Maximum, Minimum, and Average

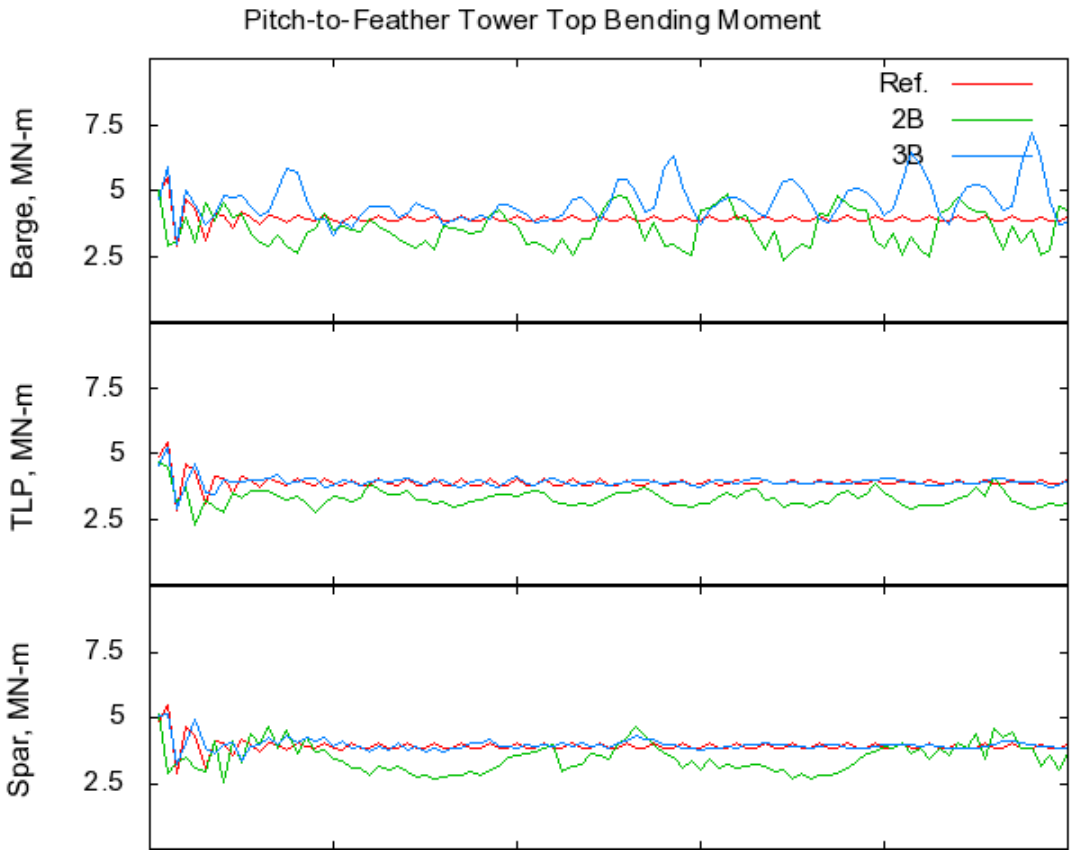

Figure A.17 - Tower-Top Bending Moment Pitch-to-Feather Time Series

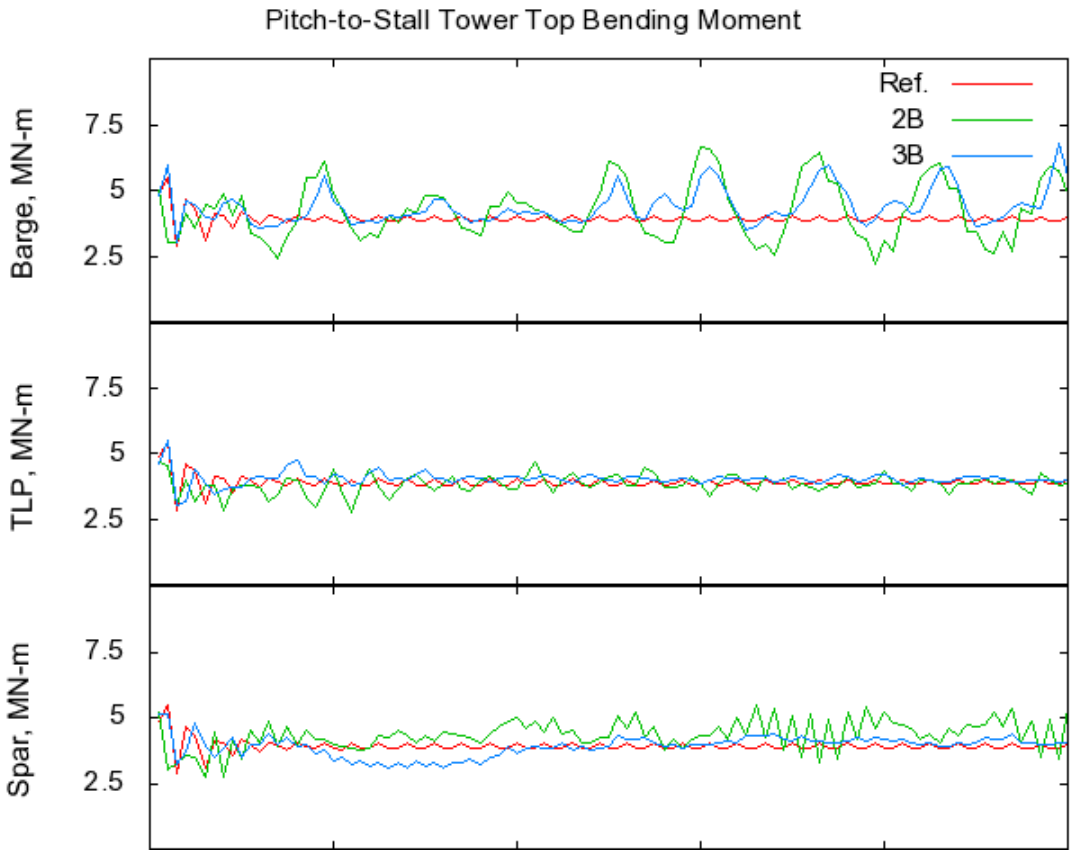

Figure A.18 - Tower-Top Bending Moment Pitch-to-Stall Time Series

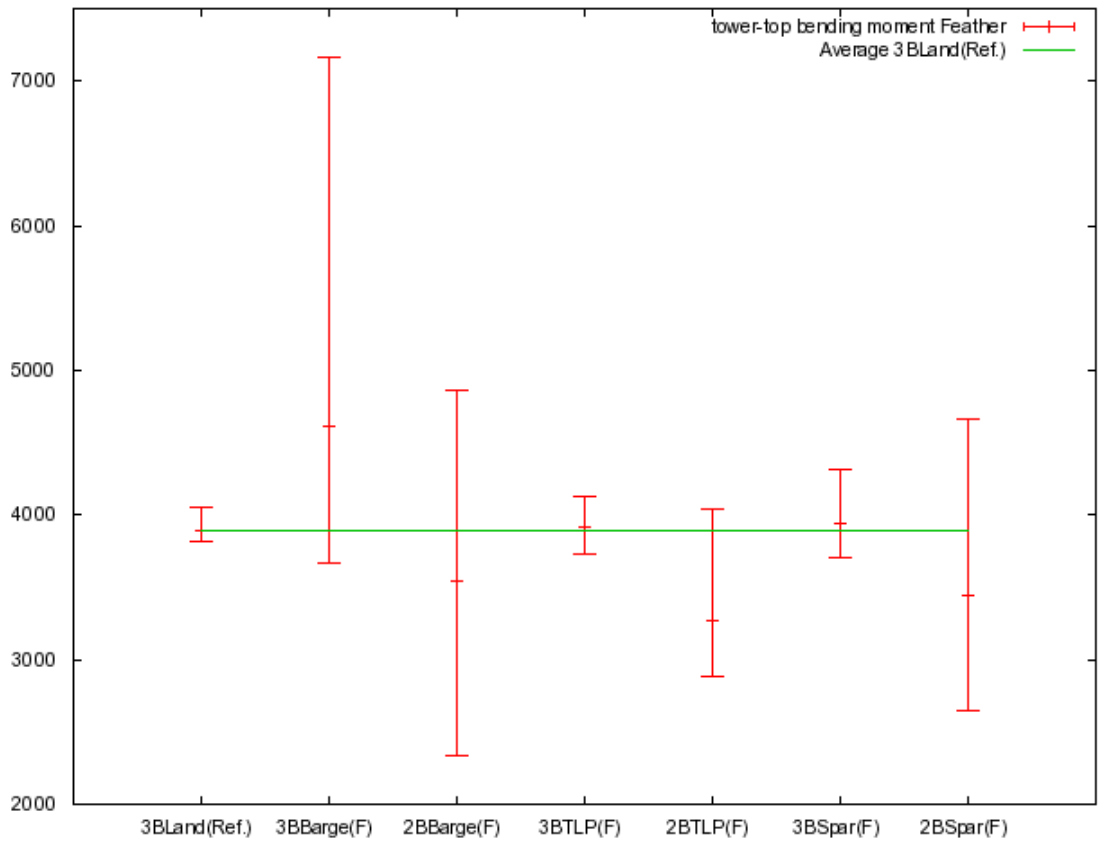

Figure A.19 - Tower-Top Bending Moment Pitch-to-Feather Maximum, Minimum, and Average

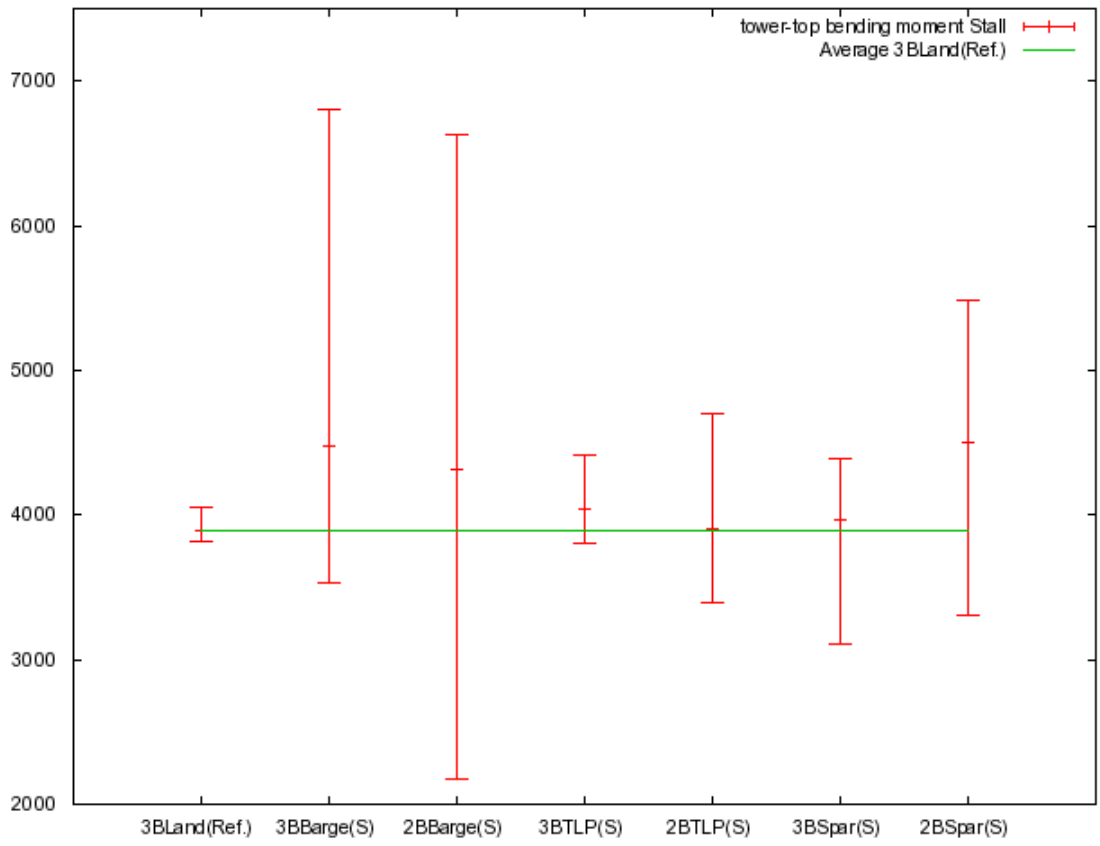

Figure A.20 - Tower-Top Bending Moment Pitch-to-Stall Maximum, Minimum, and Average

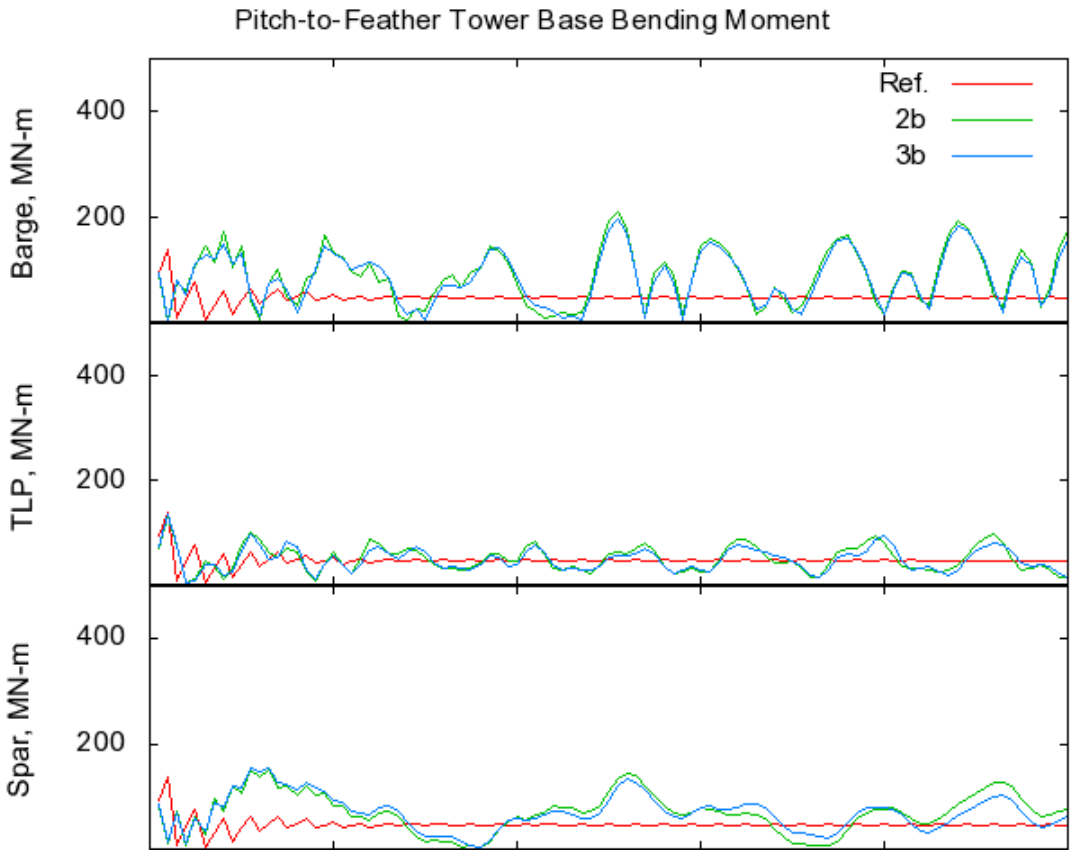

Figure A.21 - Tower-Base Bending Moment Pitch-to-Feather Time Series

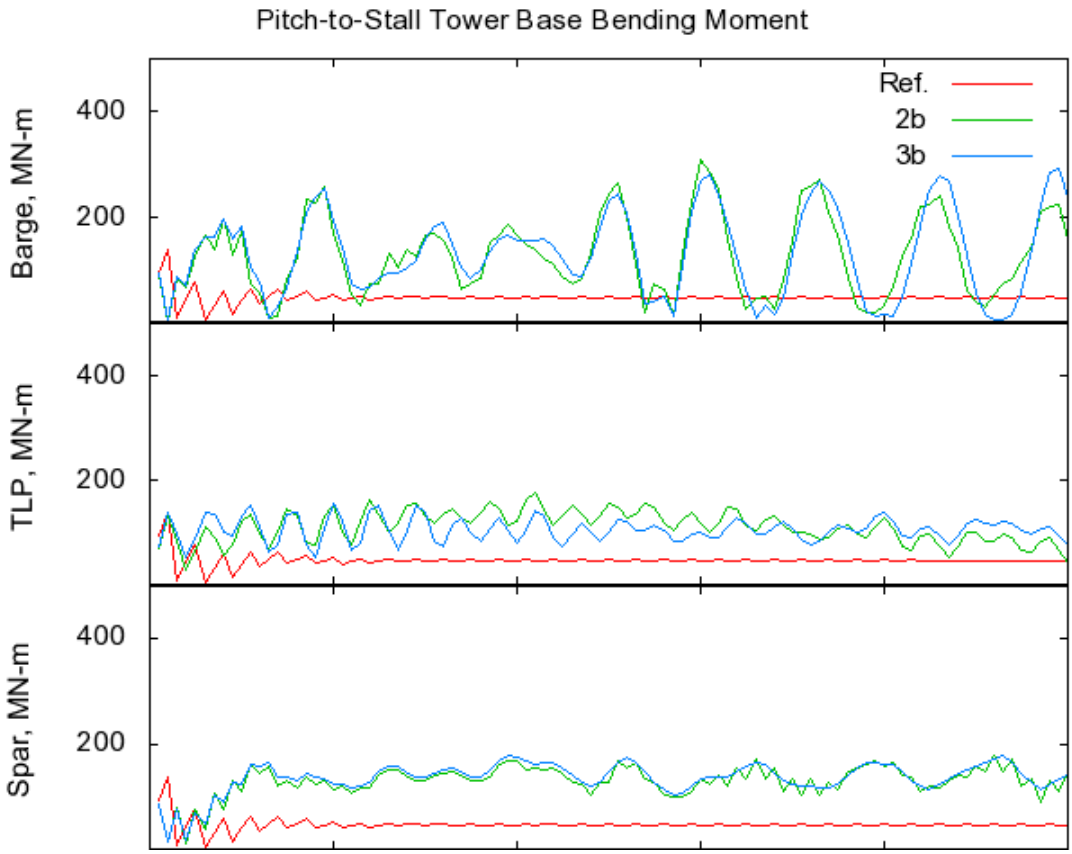

Figure A.22 - Tower-Base Bending Moment Pitch-to-Stall Time

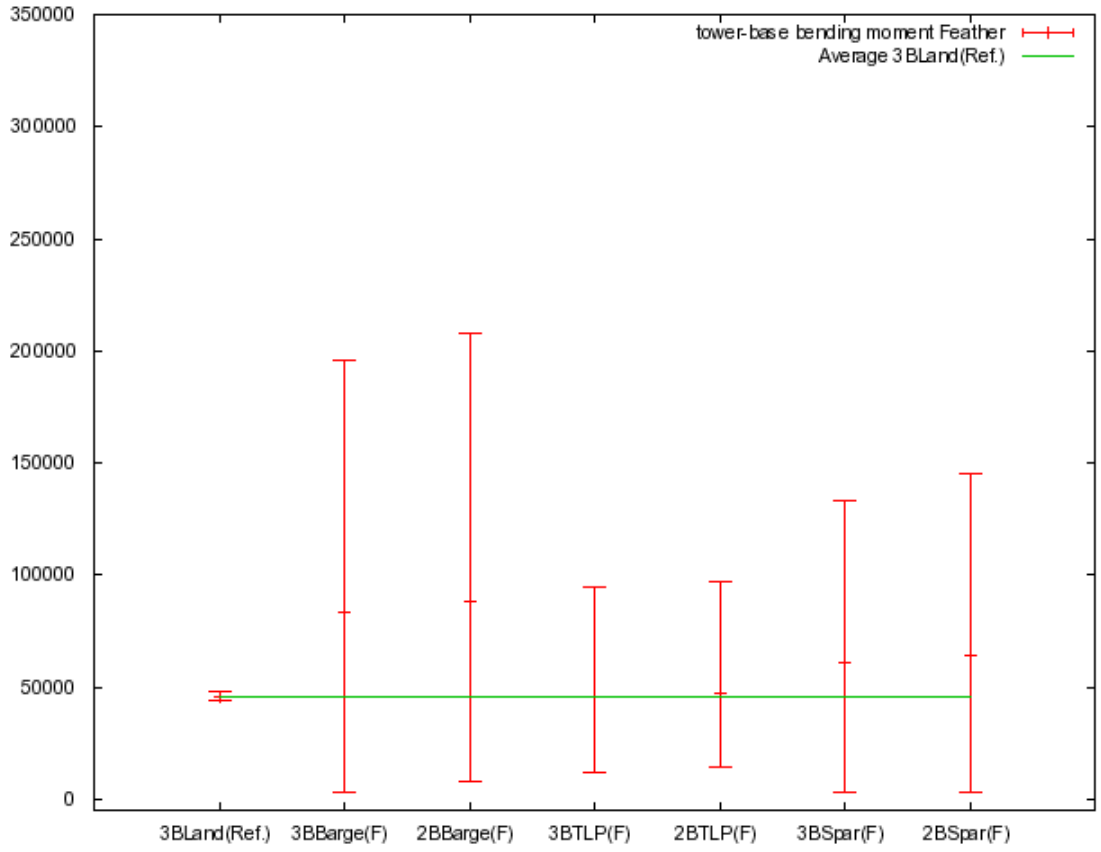

Figure A.23 - Tower-Base Bending Moment Pitch-to-Feather Maximum, Minimum, and Average

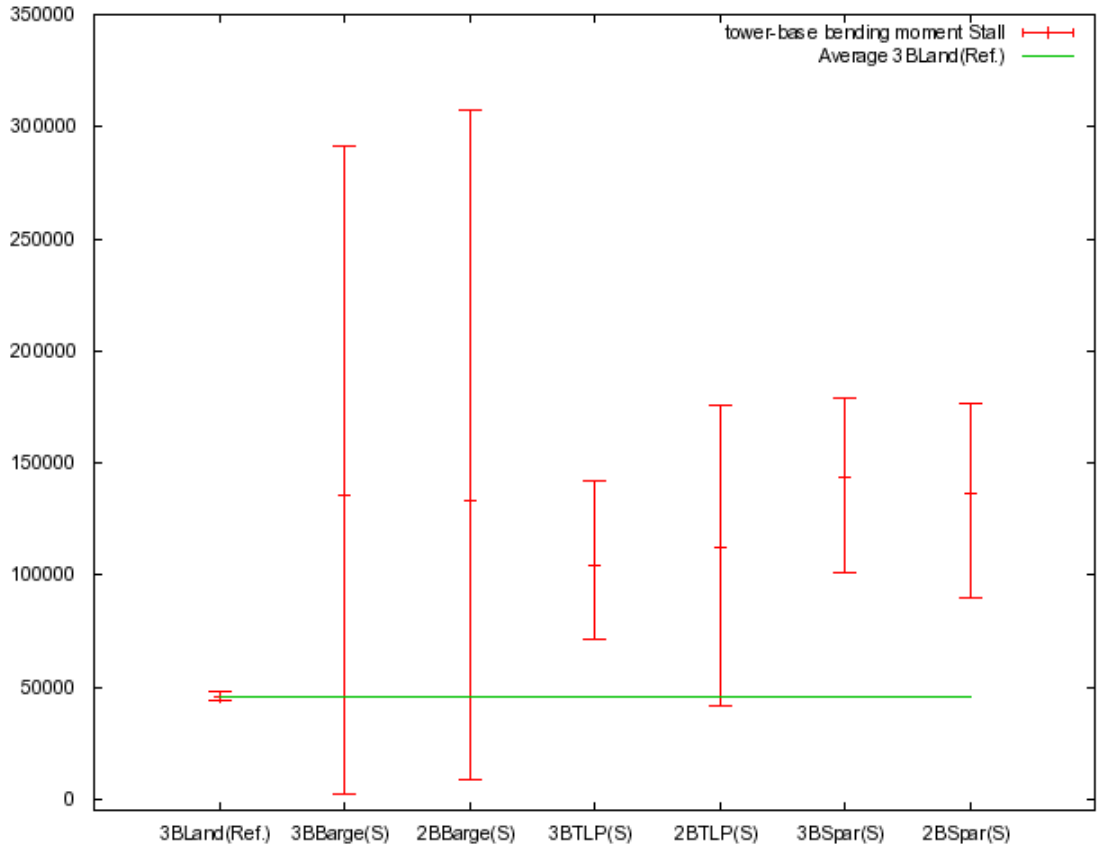

Figure A.24 - Tower-Base Bending Moment Pitch-to-Stall Maximum, Minimum, and Average

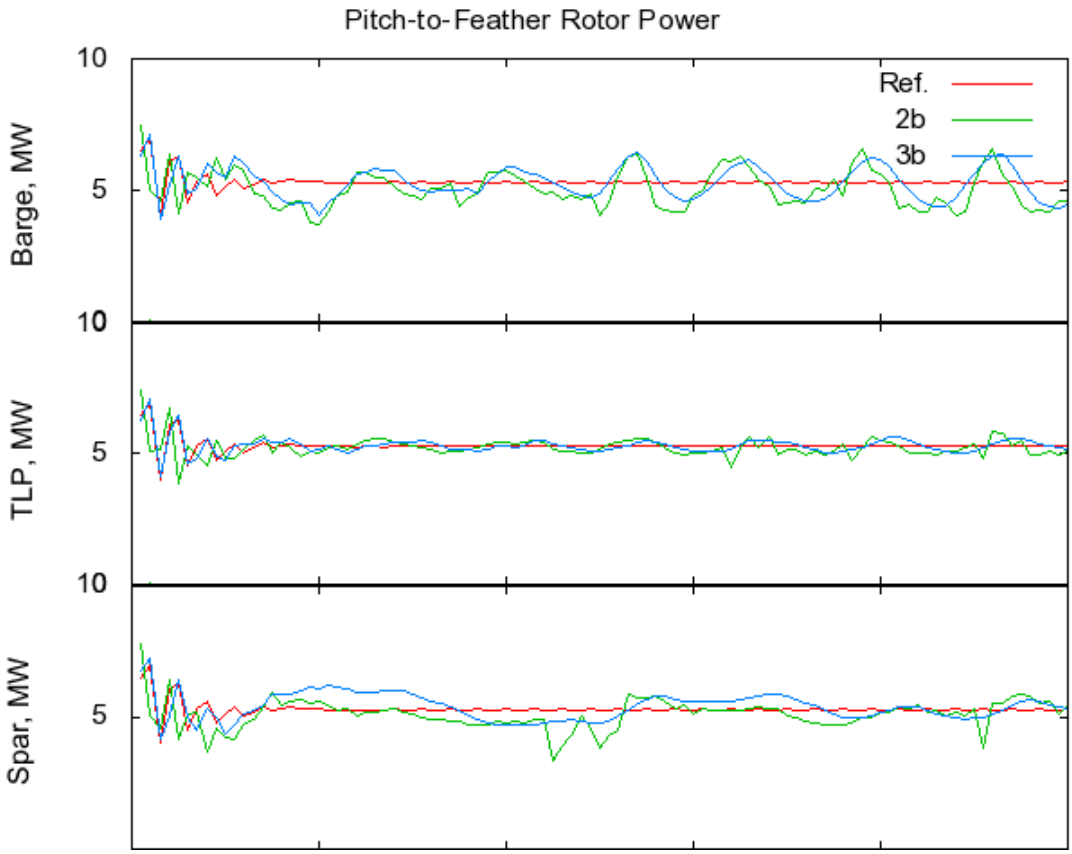

Figure A.25 - Rotor Power Pitch-to-Feather Time Series

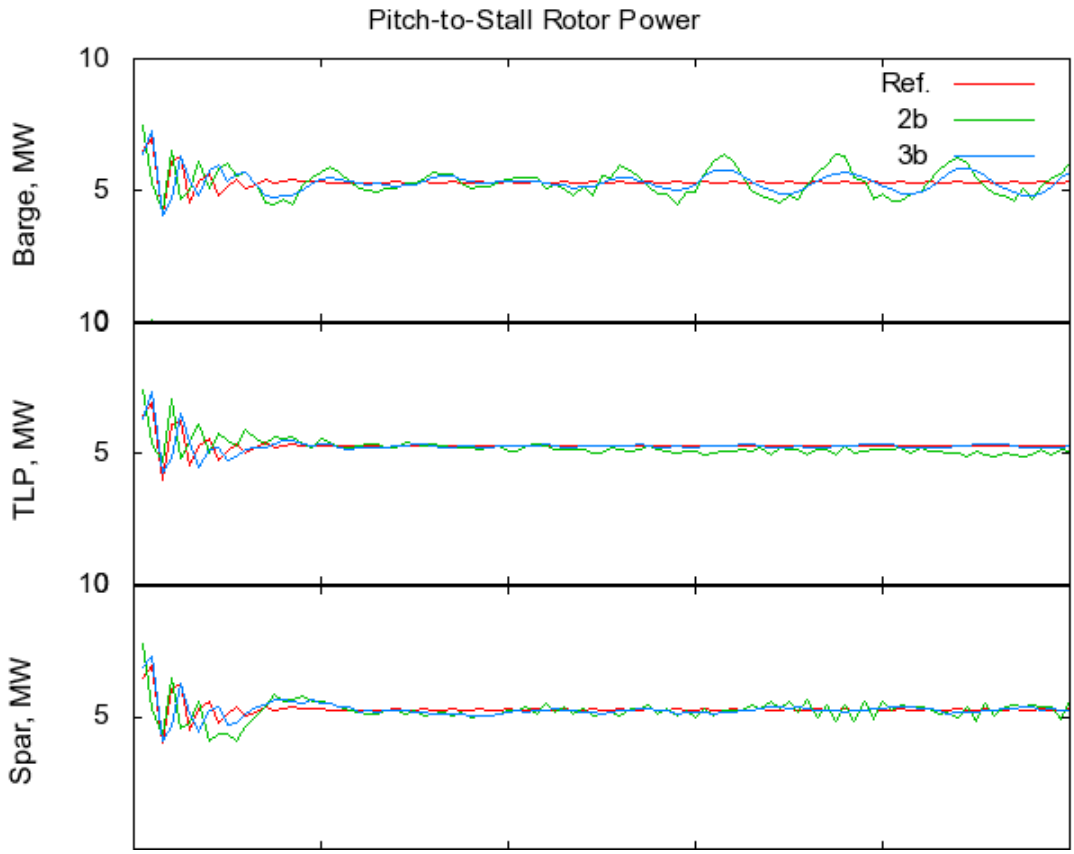

Figure A.26 - Rotor Power Pitch-to-Stall Time Series

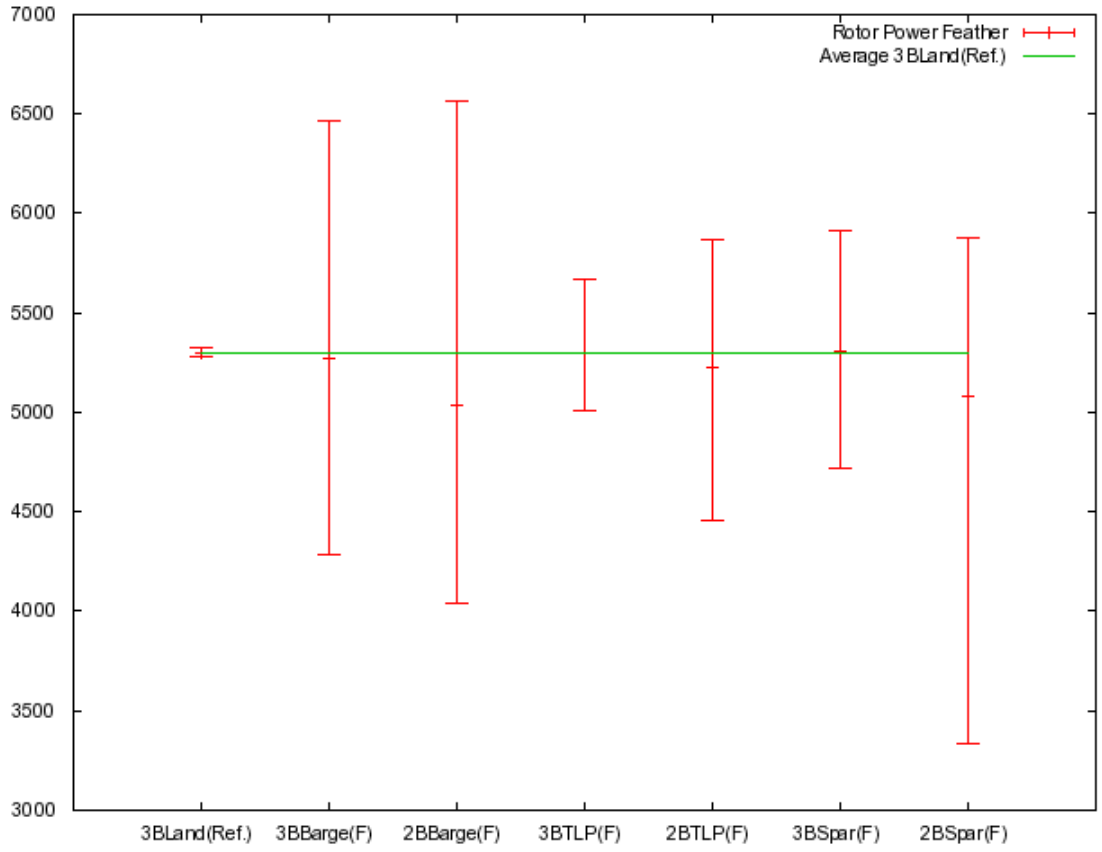

Figure A.27 - Rotor Power Pitch-to-Feather Maximum, Minimum, and Average

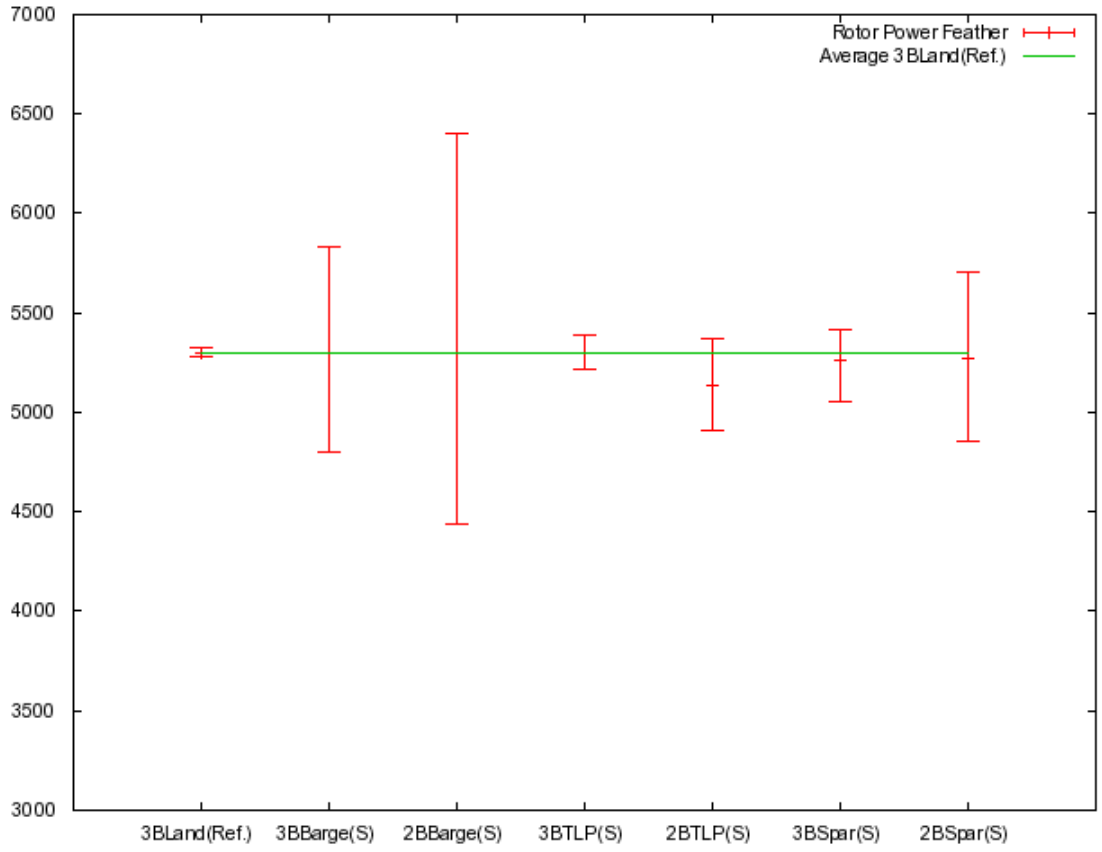

Figure A.28 - Rotor Power Pitch-to-Stall Maximum, Minimum, and Average